1997

Torque ripple minimization in vector controlled induction machines

Roberto Mario Barro
San Jose State University

INFORMATION TO USERS

This manuscript has been reproduced from the microfilm master. UMI films the text directly from the original or copy submitted. Thus, some thesis and dissertation copies are in typewriter face, while others may be from any type of computer printer.

The quality of this reproduction is dependent upon the quality of the copy submitted. Broken or indistinct print, colored or poor quality illustrations and photographs, print bleedthrough, substandard margins, and improper alignment can adversely affect reproduction.

In the unlikely event that the author did not send UMI a complete manuscript and there are missing pages, these will be noted. Also, if unauthorized copyright material had to be removed, a note will indicate the deletion.

Oversize materials (e.g., maps, drawings, charts) are reproduced by sectioning the original, beginning at the upper left-hand corner and continuing from left to right in equal sections with small overlaps. Each original is also photographed in one exposure and is included in reduced form at the back of the book.

Photographs included in the original manuscript have been reproduced xerographically in this copy. Higher quality 6" x 9" black and white photographic prints are available for any photographs or illustrations appearing in this copy for an additional charge. Contact UMI directly to order.

UMI

A Bell & Howell Information Company
300 North Zeeb Road, Ann Arbor MI 48106-1346 USA
313/761-4700 800/521-0600

TORQUE RIPPLE MINIMIZATION
IN
VECTOR CONTROLLED INDUCTION MACHINES

A Thesis

Presented to

The Faculty of the Department of Electrical Engineering

San Jose State University

In Partial Fulfillment

of the Requirements for the Degree

Master of Science

by

Roberto Mario Barro

August 1997

APPROVED FOR THE DEPARTMENT OF ELECTRICAL ENGINEERING

Dr. Ping Hsu

Dr. Peter Reischl

Dr. Addis Tesfaye

APPROVED FOR THE UNIVERSITY

M. Lou Lewandowski

ABSTRACT

TORQUE RIPPLE MINIMIZATION
IN VECTOR CONTROLLED INDUCTION MACHINES

by Roberto Barro

The dynamic response of an induction motor is immensely improved through the use of vector control. However, this controller can inherently and indirectly have an effect on the induction motor's tendency of producing torque ripple. This undesirable tendency can restrict the use of vector controlled induction machines from precision applications such as in robotics and machine tools. A detailed experimental based study on torque ripple production and reduction of induction machines under vector control is presented. A spectral torque ripple model is proposed based on the contribution of dc bias currents and torque harmonics of the actual field frequency. A parameter identification scheme is proposed. The scheme cross correlates digitally generated sine and cosine field functions with the torque ripple in order to determine the unknown parameters of the modeled torque ripple. Once the parameters are determined, the compensator generates a feedforward ripple cancellation term and performs bias current nullification.

DEDICATION

Life can be looked upon as a collage of pictures; Some pictures are black and white, others are in color, while others are still out of focus. My collage is full of pictures of people who have instilled in me strong personal characteristics. People who have selflessly dedicated their lives for the happiness of others, and have inspired me to achieve my goals. People who have shown me what hard work and ambition are truly about. I owe this respect to my parents Bruno and Antonietta. My mother is the "backbone" of our family, the source of my strength. She has demonstrated to me her fortitude in her day to day struggle to care for my brother Luciano who suffers from down syndrome. My father is the pillar of my pride. He has exemplified to me the true meaning of ambition and courage. He came to this country illiterate in English, with little education and little money, yet he achieved a very successful career as a mechanic. My parents have made endless sacrifices to enable the support of my education, and have unknowingly helped me to focus in upon the goals of my life.

At San Jose State University, Dr. Ping Hsu deserves a great deal of gratitude on my part and great deal of credit for the success of this project and the publications attained from it. His idea for torque ripple reduction is the basis of this project and my thesis. Ping, whom I sincerely consider as my mentor and respected advisor, has guided me throughout the course of my graduate education. His consistent willingness to help me or any other student and his patience in doing so are two of his many outstanding qualities as a professor and a person. I must also give credit to John Loud and Greg Mimmack, both who ambitiously took upon themselves the overwhelming project of implementing a real life vector controller at San Jose State University. I inherited their system.

Finally, I would like to say thank you to Lisa who ever so patiently has waited by my side, supported and cared for me throughout this long and arduous process.

TABLE OF CONTENTS

LIST OF TABLES

Table **Page**

LIST OF FIGURES

Figure **Page**

LIST OF VARIABLES

Variable		Units
B_{dc}	Three phase inverter dc Bus Voltage.	V
B_{sa}, B_{sb}, B_{sc}	Per phase magnetic flux density values generated in the stator by the reference stator currents.	T
B_s	Net magnetic flux density as generated in the stator windings.	T
C	Arbitrary constant used in "3 to 2" and "2 to 3" transformations.	
F_s	Controller sampling frequency.	Samp/ sec
ga_n, gb_n	Gain terms used in the proposed torque ripple compensator ($n = 1, 2, 3, 4, \cdots, \infty$).	N-m
i_{sa}, i_{sb}, i_{sc}	Three phase stator currents.	A
i_{ra}, i_{rb}, i_{rc}	Three phase rotor currents.	A
i_{saref}, i_{sbref}, i_{scref}	Instantaneous values of the per phase reference stator currents.	A
i_{sx}, i_{sy}	Two-axis direct and quadrature stator currents.	A
i_{sxref}, i_{syref}	Two-axis direct and quadrature reference stator currents.	A
I_{ox}, I_{oy}	Two-axis stator current bias offsets.	A
I_{oa}, I_{ob}, I_{oc}	Stator current bias offsets.	A
I_{sd}, I_{sq}	Two-axis direct and quadrature stator currents represented in the rotating (rotor-flux) frame.	A
I_{sdref}, I_{sqref}	Reference values of the two-axis direct and quadrature stator currents in the rotating (rotor-flux) frame.	A
I_{sdcont}	Flux controller reference value of the two-axis direct stator current.	A
k_{a1}, k_{b1}	Estimated bias current offsets.	A
k_{an}, k_{bn}	Estimated parameters used in modeling the harmonic torque ripple ($n = 2, 3, 4, \cdots, \infty$).	N-m
l_r	Rotor winding leakage inductance.	H
l_{ls}	Stator winding leakage inductance.	H

l_m	Three phase mutual inductance.	H
L_m	Two phase mutual inductance (equivalent to $1.5\, l_m$).	H
L_r	Rotor inductance defined as the mutual inductance summed with the rotor leakage inductance.	H
N_s	Number of per phase stator windings.	
p	Number of magnetic poles inside the induction motor.	
R_c	Resistance in an induction motor equivalent circuit modeling core losses.	Ω
R_r, R_s	Rotor and stator resistances respectively.	Ω
s	Rotor slip in respect to the electrical speed.	%
v_{sa}, v_{sb}, v_{sc}	Three phase stator voltages.	V
v_{ra}, v_{rb}, v_{src}	Three phase rotor voltages.	V
v_{sx}, v_{sy}	Two-axis direct and quadrature stator voltages.	V
v_{rx}, v_{ry}	Two-axis direct and quadrature rotor voltages.	V
E_{an}, E_{bn}	Parameter errors between the actual and estimated values.	A or N-m
α	Slip angle.	rad
$\dot{\alpha}$	Slip angular velocity or slip speed.	rad/s
θ, θ_e	Rotor electrical angular position in reference to the stator reference frame.	rad
θ_r	Rotor mechanical angular position in reference to a stationary reference frame.	rad
$\dot{\theta}_r$, ω_r	Rotor angular velocity.	rad/s
θ_{ref}	Desired or reference rotor position.	rad
ρ	Rotor flux vector angle in reference to the stator reference frame.	rad
τ_r	Rotor time constant.	s^{-1}

T_a	Augmented torque reference term generated by the summation of the reference torque parameter and the torque feedforward term.	N-m
T_e	Electromagnetic torque production in AC or DC machines.	N-m
T_f	Torque feedforward reference term generated by the ripple compensator.	N-m
T_m	Transient rich torque measured from the torque sensing transducer.	N-m
T_{mod}	Modeled harmonic torque ripple component.	N-m
T_{p-p}	Peak to peak torque ripple.	N-m
T_r	DC free time varying transient rich torque ripple.	N-m
T_{ref}	Reference torque used for general vector control.	N-m
Ψ_a	Actual Rotor flux linkage.	Wb
Ψ_c	Flux contribution due to dc bias current offsets.	Wb
Ψ_r	Rotor flux linkage.	Wb
Ψ_L	Leakage flux of the rotor windings.	Wb
Ψ_m	Mutual flux of the stator and rotor windings.	Wb
Ψ_{sa}, Ψ_{sb}, Ψ_{sc}	Three phase stator flux linkages.	Wb
Ψ_{ra}, Ψ_{rb}, Ψ_{rc}	Three phase rotor flux linkages.	Wb
Ψ_{rx}, Ψ_{ry}	Two-axis rotor flux linkages.	Wb
Ψ_{ref}	Reference flux used for general vector control.	Wb
ω_{ref}	Desired or reference rotor angular velocity.	rad/s
ω_{slip}	Slip speed defined as the difference of the rotor angular velocity and the stator electrical speed.	rad/s
ω_{sync}	Synchronous or electrical speed.	rad/s

Superscripts

s	Variable referenced to the stator frame.
r	Variable referenced to the rotor frame.
Ψ_r	Variable referenced to the rotor-flux frame.

Acronyms

AC	Alternating Current
ADC	Analog to Digital Converter
DC	Direct Current
DAC	Digital to Analog Converter
FOC	Field Oriented Control
KVL	Kirchoff's Voltage Law
PI	Proportional Integral Controller
PID	Proportional Integral Derivative Controller
PWM	Pulse Width Modulation
VC	Vector Control

CHAPTER 1

Introduction

The dynamic response of an induction motor is immensely improved through the use of vector control [31]. However, this controller can inherently and indirectly have an effect on the induction motor's tendency of producing torque ripple. This undesirable tendency can restrict the use of vector controlled induction machines from high precision applications such as in robotics and machine tools. It is the objective of this thesis to present a detailed experimental based study on torque ripple production and reduction of induction machines under vector control. This study is based on the formulation of a new engineering idea and the collection of empirical data. This study has led to publications in several conference proceedings relating industrial power electronics and motor control (v., [5], [6]). In order to clearly understand the problem chosen for study, Chapters 1, 2 and 3 are dedicated to establishing the background information and theory of controls systems engineering, induction machines and vector control. In Chapter 4, a spectral torque ripple model is proposed based on the contribution of dc bias currents and torque harmonics of the actual field frequency. In addition, a parameter identification scheme is also proposed. The scheme cross correlates digitally generated sine and cosine field functions with the torque ripple in order to determine the unknown parameters of the modeled torque ripple. Once the parameters are determined, the compensator generates a feedforward ripple cancellation term and performs bias current nullification. A series of experiments and conclusive observations are presented in Chapter 5 to show the effectiveness of the proposed scheme.

Control Systems Engineering

"Engineering is concerned with understanding and controlling the materials and forces of nature for the benefit of humankind" [10]. Historically, control system engineers have contributed immensely to the technological growth and sophistication of society

today. Fundamentally, the most important historical control example occurred in 1927, when Harold S. Black at Bell Laboratories invented the electronic feedback amplifier [11]. This important idea made it possible in the decades following World War I for communication over long distances. His simple solution is the basic root of automatic control. Of course, there were many other key contributors to the growing field of control theory (e.g., James Maxwell, E.J. Routh, A.M. Lyapunov, W.R. Evans, H. Nyquist and H.W. Bode). As a whole, this group of engineers (or theorists) laid down a solid theoretical foundation that control systems of the present are based on. This includes all the classical and modern analytical techniques utilizing frequency (i.e., Laplace Transform) and time based system analysis. On the other hand, the challenges faced by the control engineers of the past compared with those of the present does reflect the dynamic changing nature of our world. Our world today is a "digital" one and the challenge is more complicated than ever before. Today, control systems are utilized in all facets of life including computers, communications, entertainment, transportation, military and industrial processes using robotics, automation and motion control. The scope of control systems is broad, but in general these systems require optimal performance under stringent operating conditions and widely varying specifications.

The underlying principal of control system engineering is to coerce, if possible, the dynamic behavior of any given system to conform to a stable desired system response utilizing feedback. The classical general model of feedback control is shown in Figure 1.1.

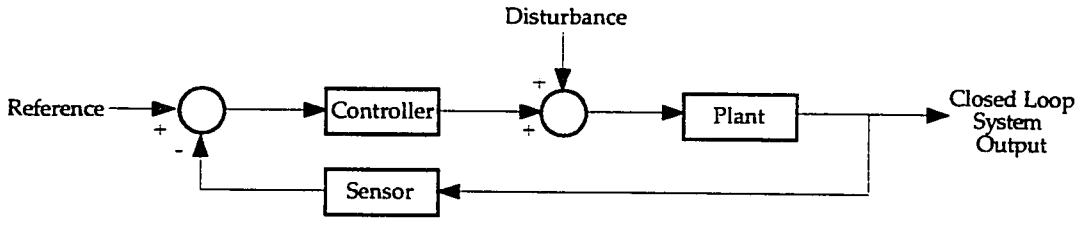

Figure 1.1. Classical Closed Loop Feedback Control System.

The system or process to be controlled is generally denoted as the "plant." By using some type of sensing device the closed loop system output is fedback, measured and set to track the reference input. In other words, plant control is performed by continually reducing the difference error e(t) between the reference input and system output [10].

Although such a system may seem trivial in nature to implement, in reality, there are multiple critical design issues a control engineer must investigate. First of all, the most important question that arises is the issue of plant modeling and if needed, linearization. A given control system will only be as good as the system model, and an inaccurate model will render the designed controller useless under actual implementation. A typical system model is a defining set of differential equations describing the process [11]. This process can be modeled (identified) using transient analysis, frequency response data, psuedorandom noise data, and/or the least squares method [11]. System identification through the aforementioned techniques in general can be a complex and an expensive goal to undertake, but it is imperative and critical for designing an accurate closed loop control system.

Once the plant model has been identified the engineer must investigate what type of canonical realization will suffice. In other words, will a classical feedback model (i.e., Laplace transform based) as in Figure 1.1 be acceptable or will it be necessary to use modern canonical forms based on state space (multivariable) feedback. Secondly, once the system is identified and a canonical form realized, upon the application of feedback will the system remain stable and if so, what are the stability margins of the system? Conversely, if the system becomes unstable, can the system under the correct control effort become stable? Third, how robust is the system? In other words, will the system conform to the desired reference trajectory under the presence of external disturbances or by changing plant dynamics (parameter sensitivity)? Finally, in terms of performing a transient analysis of the control system, issues pertaining to steady state error, damping, overshoot, rise

time, and settling time all need to be addressed for each selected control action [11]. Note that extensive techniques such as frequency response methods (Bode and Nyquist), pole placement using root locus design, and state space methods have been developed to answer these control questions.

Upon successful computer simulation, actual control system design and realization will of course vary from system to system. In the real life application the engineer is faced with two types of system realization: analog or digital. The analog control system consists of using a continuous time controller in conjunction with a continuous time plant as in Figure 1.1 as on page 2. On the other hand, a digital control system uses a discrete time counterpart controller in conjunction with a continuous time plant. A general diagram of a digital based control system is shown in Figure 1.2 below. The choice of which control system to use is dependent on the degree of difficulty in the realization (e.g., system order), precision, practicality, performance, cost, and safety. In some simple cases the use of either type of controller is feasible. For example, performing precise position control of a dc servo motor is plausible either through the use of a discrete or a continuous time controller [11]. In contrast, the motion control systems used in modern aviation (e.g., B-2 Stealth Bomber) and space exploration are very complicated and must use microprocessor based control systems [25]. In particular, a vector controlled ac machine is one other example on why digital control is essential. The requirements of a such a controller emphasize the need of using a flexible custom designed program. Furthermore, the complexity and costs of performing coordinate transformation, multiplication, and function

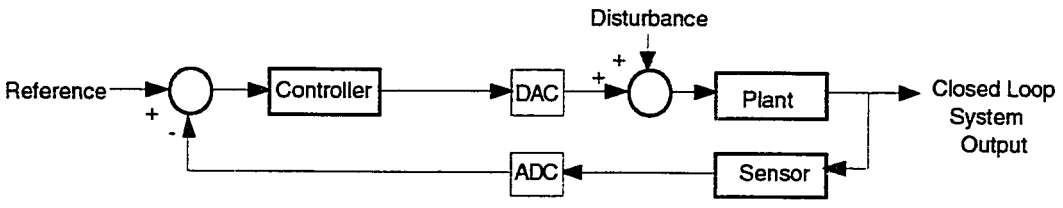

Figure 1.2. Digital Closed Loop Feedback Control System.

generation using analog components undermine the case of purely continuous time control [22]. The level of sophistication required by a vector controller is now practical, realizable and economical through use of on-line digital control.

Economics

Economically , the business of control systems is a multi-billion dollar industry. A good indicator into the marketing growth of control systems is the chart shown in Figure 1.3 on page 6. As determined by the U.S. Department of Commerce the chart represents the U.S. factory sales from 1985 to 1994 [33]. The reported factory sales clearly demonstrate the staggering continual annual growth in the controls business. Estimates for 1994 in the United States alone exceed fifteen billion per year! In fact, control systems and the required processing equipment account for 50.3% of business in the industrial electronics sector [33]. More specifically, the market for adjustable speed drives as shown in Figure 1.4 on page 6 is steadily increasing and as of 1994, sales surpassed three quarters of a billion dollars [33]. Finally, Figure 1.5 on page 6 as adapted from [3] shows that although the dc drive market is still in popular demand, the growth rate of the ac drive market is growing at five percent compounded annually in comparison to one percent growth rate of the dc market. Vector control has contributed a great deal to the steady growth of the ac market as will be discussed in this next section.

Background Vector Control

As a basis for precision motion control, dc motors and synchronous motors have typically been used in commercial, industrial, and military applications. In general, these applications require variable speed, four quadrant operation, and precision torque control at all speed. AC motors through the use of modern control algorithms are penetrating the dc motor marketplace. At the present time, the advancement of power semiconductor devices and the advent of digital signal processing have made it both possible and economical to

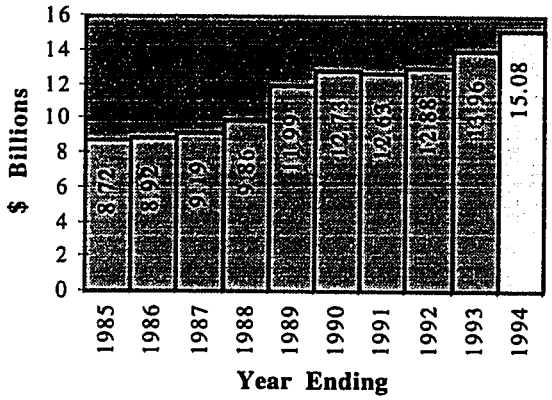

Figure 1.3. U.S. Factory Sales of Controls and Processing Equipment. (Source: 1996 Electronic Data Book.)

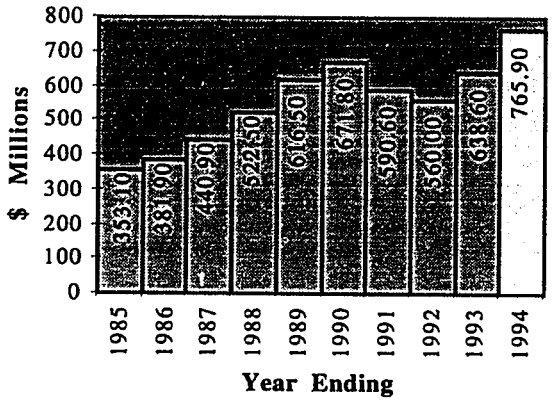

Figure 1.4. U.S. Factory Sales for Adjustable Speed Drives. (Source: 1996 Electronic Data Book.)

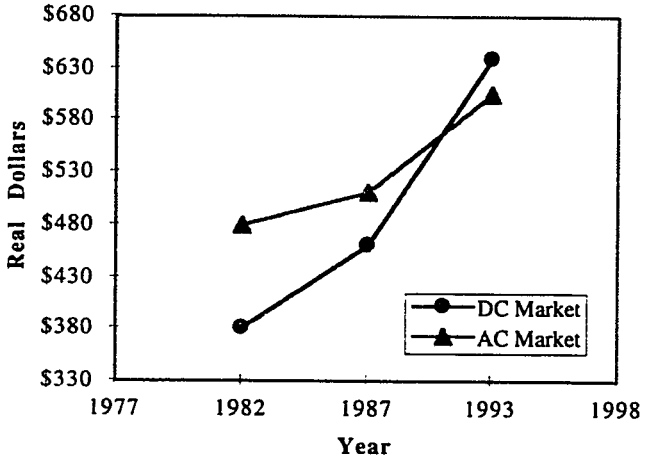

Figure 1.5. AC and DC Motor Market Growth Rates. (Source: D. Bak, "AC 'Drives' Ahead," *Engineering News*, pp. 23-24, May 6, 1996.)

use induction motors under vector control (abr., VC), alternatively named field oriented control (abr., FOC), for precision motion applications [31].

The induction machine has been around for over a century and it is considered to be the "workhorse of industrial processes throughout the world" [23]. The idea of polyphase alternating current and the design of induction machines is credited to Nikola Tesla for which he received a patent in 1888 [8]. The merits of an induction machine with a squirrel cage rotor running at fixed speed clearly defines why such a machine is a widely used industry workhorse. An induction motor is a structurally sound, simple, rugged, powerful, economical, extremely reliable, and low maintenance industrial commodity [18]. Moreover, since an induction motor is a brushless machine no sparks are generated and hence (as a low-cost alternative to the expensive dc brushless motor), the motor can be used in hazardous environments where explosive and flammable gases are present. For these reasons, an induction motor is clearly superior to a dc machine. On the other hand, the usefulness of such a machine is typically limited to only driving pumps, fans, and specialized equipment (e.g., drill press and milling machines). The reason is simply the fact that speed control of an induction motor is very difficult to achieve [18]. Typically, a mechanical reducing gearbox is used to perform speed adjustment. Modern techniques include using line frequency variation or the use of pulse width modulation (abr., PWM) [8]. The use of a variable frequency current source inverter (abr., CSI), a speed sensor, and a speed controller for example, is clearly not enough to warrant the use of induction motors for closed loop control of high performance systems. In this case, because the induction motor model used is based on steady state conditions, a poor transient response will result as well as inadequate low speed performance [8]. The induction machine is a "highly non-linear dynamic structure with strong dynamic interactions" and the dynamic model of such a machine is typically represented by a sixth order state space equation [31].

Therefore, a controller based on steady state characteristics is not enough for applications requiring fast stable dynamic performance at all speeds [22].

Vector control is a means for effectively "decoupling the complex multivariable control structure of the induction machine" [22]. Moreover, the most important merit of vector control is its ability to precisely and instantaneously control output torque over the rated speed, including stall conditions. Because of this property, a vector controlled induction motor can be used in conjunction with most feedback control schemes (e.g., PID or state feedback) to achieve a high level of performance. For example, the user now has the option to use an induction motor for variable speed operation or for running at a preferable fixed speed of choice (not as specified on the motor nameplate). The real advantage of vector control is the fact that all of the merits of induction motors like their low cost, ruggedness and reliability, can now be realized in demanding motor control applications.

The market demand for vector controlled adjustable speed drives has been steadily and increasingly growing, but the path from theory to the practical implementation of such a controller was complex. The slow market growth of vector drives can be attributed to a number of factors. Ten years ago the availability of computational power at a reasonable cost hindered the growth of vector drives [4]. Moreover, there were reliability issues pertaining to the control and power electronics under development [4]. Finally, the perception of complexity and reservations on devoting a rather expensive controller for a such a relatively inexpensive motor are other negative factors that hindered the development of vector drives [4]. Today vector controllers are declining in cost and are increasing in reliability [3]. They are penetrating the traditional areas of the market where dc motor control is prominent. Figure 1.6 on page 9 as adapted from [4] demonstrates where the U.S. market exists for vector controlled induction machines. The factory automation

segment of vector controllers is expected to grow at a compound annual growth rate of 12.5% [4].

Presently, induction motors are used in some of the most demanding motor control applications developed today. Some examples include using vector controlled induction machines for high speed elevators, cranes, winding equipment, machine spindle drives, steel casting lines, and plastic extruders [4]. Due to the fact that vector control allows precise instantaneous torque control, high torque when stalled, and regenerative abilities, a three-phase induction motor also can effectively be used in the propulsion of an electric vehicle (e.g., General Motor's EV1) [9], [28]. During regeneration, an induction machine is used as a generator and in the case of the EV1, this effect is used to brake the vehicle, recover, and channel some of the vehicle's kinetic energy back to the battery cells [28].

The future of vector control looks very strong and it appears that the evolution of this system is far from being completed. Although the topic of vector control is very

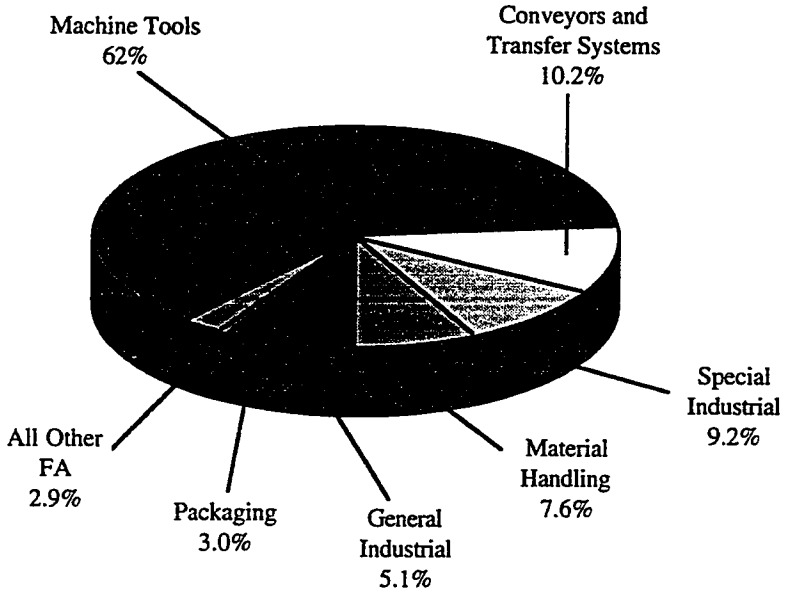

Figure 1.6. 1993 U.S. Market for AC Induction Vector Control Motors and Drives in Factory Automation Applications Totaling $80,700,000. (Source: F. J. Bartos, "Flux Vector AC Drives are Poised for Wider Growth," *Control Engineering*, pp. 75-81, Feb. 1995.)

dense, it is a well-researched area and a great deal of journal literature exists regarding the theory and new trends in this area. The background research conducted for this project confirms this fact. On the other hand, a thorough search through the technical literature will show that (ca., 1989 to 1996) little research has been performed in understanding the indirect link between vector control and the production of torque ripple. This problem will be introduced in the subsequent section.

Problem Description - Torque Ripple

In many industrial applications requiring precision motion control servo motors (e.g., dc motors) are used for impulsion. The general characteristics of these servo motor applications may include all or some of the following: (1) high torque capabilities, (2) fast response to acceleration/deceleration trajectories, (3) frequent start and stopping operations, (4) four quadrant operation, (5) field weakening capabilities, (6) zero speed torque production, (5) overloading capacity at all speeds, and (7) minimized or zero torque ripple [31]. In high precision control applications, the ability to produce perfectly steady torque at near zero or zero speed is very critical. For example, in robotic applications, a small amount of torque ripple at the base joint may result in high amplitude vibration at the end-effector. The presence of torque ripple "may excite resonances in the mechanical portion of the drive system, produce acoustic noise, and in machine tool applications, leave visible patterns in high-precision machined surfaces" [15]. In general, the consequence of torque ripple may deteriorate the precision performance of the drive, damage machine components, and shorten the life of the machine.

Despite the recent improvement on control performance due to the theory of vector control [4], the usage of induction motors in precision control applications has been very limited [5]. This is partially due to the fact that induction motors have a tendency of producing torque ripple even at zero speed. Figure 1.7 on page 11 shows a locked rotor torque measurement of an induction motor under an "untuned" vector controller. Figure

1.8 on page 12 is a FFT spectrum plot of the torque measurement in Figure 1.7. These figures clearly show the periodicity of the torque ripple. Specifically, the ripple energy is concentrated on the first (9.5 Hz), second, and sixth harmonics of the field frequency. Note, the term "torque ripple" used throughout this thesis defines the combined effects of the fundamental and harmonic (if present) torque ripple components.

Although torque ripple production by induction machines under general control is a well documented phenomena, very little research has been performed on torque ripple modeling or reduction for induction machines under vector control. As mentioned in the introduction of this chapter, it is the objective of this thesis to model the source of the torque ripple and propose a solution. In this thesis a torque ripple reduction scheme is proposed. This scheme utilizes the structure of vector control. The reduction of torque ripple is achieved via a feedforward ripple cancellation term and the use of bias current nullification terms. The key parameters of these cancellation terms are identified by an adaptive identification scheme. A detailed sequence of experiments have been performed to show the effectiveness of the proposed scheme. This scheme will give vector controlled induction machines a new higher level of performance, striving to reach the high standards set forth for servo motion control.

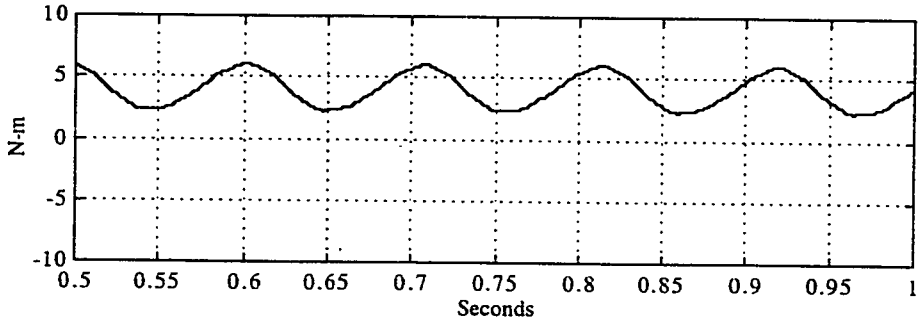

Figure 1.7. Torque Ripple Phenomena of a Vector Controlled Induction Machine[1].

[1] Experimental data of a 2 hp, 4 pole, 3 phase induction motor under static (locked rotor) conditions.

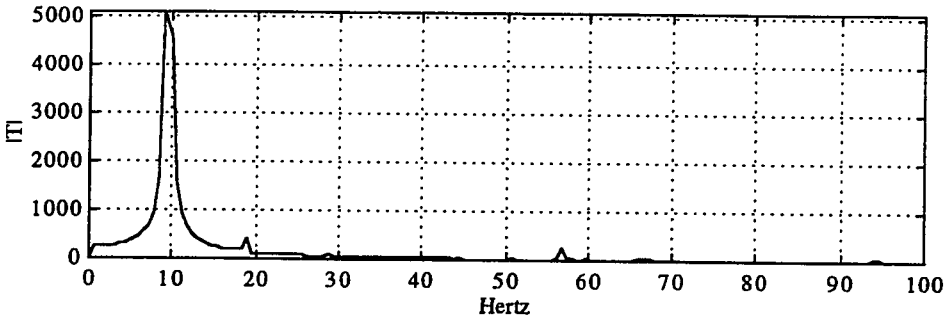

Figure 1.8. DFT Frequency Spectrum of the Torque Ripple as shown in Figure 1.7.

CHAPTER 2

Three-Phase Induction Machines

The objective of this chapter is to explain the inner workings and principle theory of induction machines. This chapter is not meant to regurgitate the theory as presented in many existing classical motor textbooks. On the other hand, the context of this material will be presented as a basis for understanding the theory of vector control as will be discussed in Chapter 3. In order to facilitate this goal, emphasis will be placed on (1) understanding the general design features of the induction machine, (2) setting forth how a rotating magnetic field is generated, (3) describing briefly the fundamental concepts of two-axis theory, (4) deriving the motor voltage and flux linkage expressions (5) understanding electromagnetic torque production and deriving the mathematical model of this effect, and (6) understanding the motor dynamics.

General Induction Machine Design Features

Induction machines fall under the general class of ac machines. In general, the induction machine can behave as a generator, where mechanical energy is converted to ac electrical energy, or it can behave as a motor where electrical energy is consumed to produce mechanical energy [8]. The principal of operation is based on magnetic induction as in a simple transformer. In a transformer, when a time varying voltage is applied to the primary windings, a magnetic flux is produced as given by Faraday's law. As the magnetic flux varies in the core of the transformer, the voltage in the secondary windings is induced by electromagnetic induction. In other words, in a transformer the primary and secondary windings are magnetically linked. In a similar fashion, the stator and rotor windings are magnetically linked, but contrary to the transformer, the rotor windings are free to rotate in reference to the stator. Note that these machines are called "induction machines" simply because the rotor voltage (which produces the rotor current and rotor magnetic field) is induced in the rotor windings by a rotating magnetic flux produced by the

stator windings. As a direct result of this "induction" an interaction exits between the rotating magnetic field set up by the stator currents and the magnetic field set up by the rotor currents thereby producing electromagnetic torque [23]. This electromagnetic torque will rotate the rotor in the direction of the rotating magnetic field.

The most common type of induction machine is the motor with a squirrel cage rotor as shown in Figure 2.1. This type of rotor uses either copper or aluminum for the rotor bars embedded in slots which terminate in short-circuiting end rings. Typically, these bars are skewed to reduce torque variations and to prevent the rotor and stator teeth from lining up opposite of each other and locking up [18]. The second type of rotor construction is the wound rotor type. In this construction the rotor consists of a three-phase set of windings "Y" connected and wound for the same number of poles as the stator windings. In addition, the rotor windings are brought out through slip rings where resistors can be externally added in series to vary rotor resistance [23]. In either case, the rotors bars or rotor windings are distributed in slots along the rotor structure. The rotor structure consists of a highly permeable steel alloy used to maximize magnetic flux density and minimize core losses. Similarly, the stator windings are place along the perimeter of the stator structure in slots as well. Again, highly permeable steel alloy is used to yield high magnetic flux

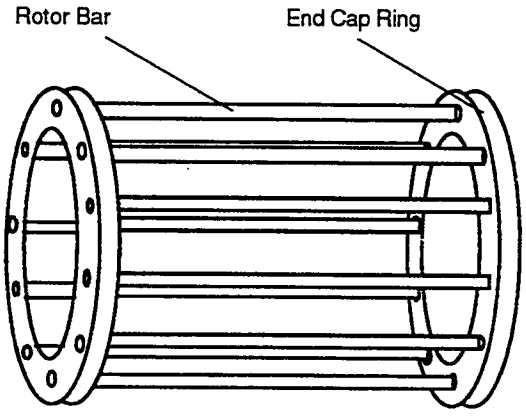

Figure 2.1. Squirrel Cage Rotor of an Induction Machine.

density and low core losses. Moreover, in order to induce a sinusoidal voltage in the rotor windings by a sinusoidal flux density vector, it is necessary to distribute the stator windings of each phase using

$$n_s = N_s \cos(\theta), \tag{2-1}$$

where N_s is the maximum number of conductors practicable in the machine to be designed. The stator windings are placed in slots in the stator and are done so to create magnetic poles around the perimeter of the stator [23]. However, in practice, it is not possible to accurately distribute windings in this fashion since there are a finite number of slots and an integral number of turns which can be allotted per slot [8].

The Rotating Magnetic Field Principle

One major principle in the operation of the induction machine is that of the rotating magnetic field principle. If three-phase power is impressed on the stator windings then a rotating magnetic field of constant magnitude is produced. For simplicity this concept can be best understood through the use of a generalized rotor-less motor. In addition, this induction motor will be further simplified by describing it with three single turn coils spaced 120° apart as shown in Figure 2.2 on page 17. Upon the application of three-phase sinusoidal voltage, current will flow through these stator windings and as a result, each phase will produce a magnetic flux density denoted separately as

$$B_{sa} = B_m \sin(\omega t), \tag{2-2}$$

$$B_{sb} = B_m \sin(\omega t - 120°), \tag{2-3}$$

$$B_{sc} = B_m \sin(\omega t - 240°), \tag{2-4}$$

where B_m is the maximum amplitude of flux density produced by each phase.

Note that in Figure 2.2 current flowing in the conductors (into the page) is denoted by a crosshair, and current flowing out of the page is denoted by a dot. The directions of the corresponding flux density vectors is given by using the classical right hand rule. A

mathematical proof of the rotating magnetic field concept using these flux density vectors is given by [8] and will be summarized here. The net magnetic flux density in the stator is given as

$$\vec{B}_s(t) = B_{sa}(t) + B_{sb}(t) + B_{sc}(t). \tag{2-5}$$

Note that once equations (2-2), (2-3), and (2-4) are substituted into (2-5), the components of each of the magnetic fields can be broken into x and y components, combined, and through the use of trigonometric identities, the final result in equation (2-6) is derived.

$$\vec{B}_s(t) = [1.5B_m \sin(\omega t)]\hat{x} - [1.5B_m \cos(\omega t)]\hat{y} \tag{2-6}$$

As the electrical angle (ωt) varies with respect to time, it is possible to show through the use of (2-6) that a constant field rotates. As shown in Figure 2.2, (ωt) is set to equal four intervals in time: 0°, 90°, 180°, and 270°. Clearly, as these values vary, the field or field poles will rotate in a counter-clockwise fashion. It will be later shown that the torque on the rotor will cause the rotor to accelerate and rotate in the same direction as the magnetic field. Moreover, if clockwise rotation is desired only two of the three connection leads supplying the motor with current need to be swapped [8].

Relating Mechanical and Electrical Speeds

Figure 2.2 also represents the rotating magnetic field as a field generated by a pair of imaginary rotating magnetic poles (north and south). This machine is described as a two-pole machine and for every electrical cycle these magnetic poles will rotate one complete mechanical revolution. In other words, since the rotor will follow this rotation, then for one complete electrical cycle the rotor will turn 360°. If the stator is wound for a higher number of poles then the rotor will spin at a lower speed. In general, if there are (p) magnetic poles on the induction motor stator, then there will be p/2 repetitions of the winding sequence a-c'-b-a'-c'-b [8]. Therefore, the electrical speed $d\theta_e/dt$ of the stator magnetic field is related to the mechanical speed $d\theta_r/dt$ of the rotor as

$$\frac{d\theta_e}{dt} = \frac{p}{2}\frac{d\theta_r}{dt}. \qquad (2\text{-}7)$$

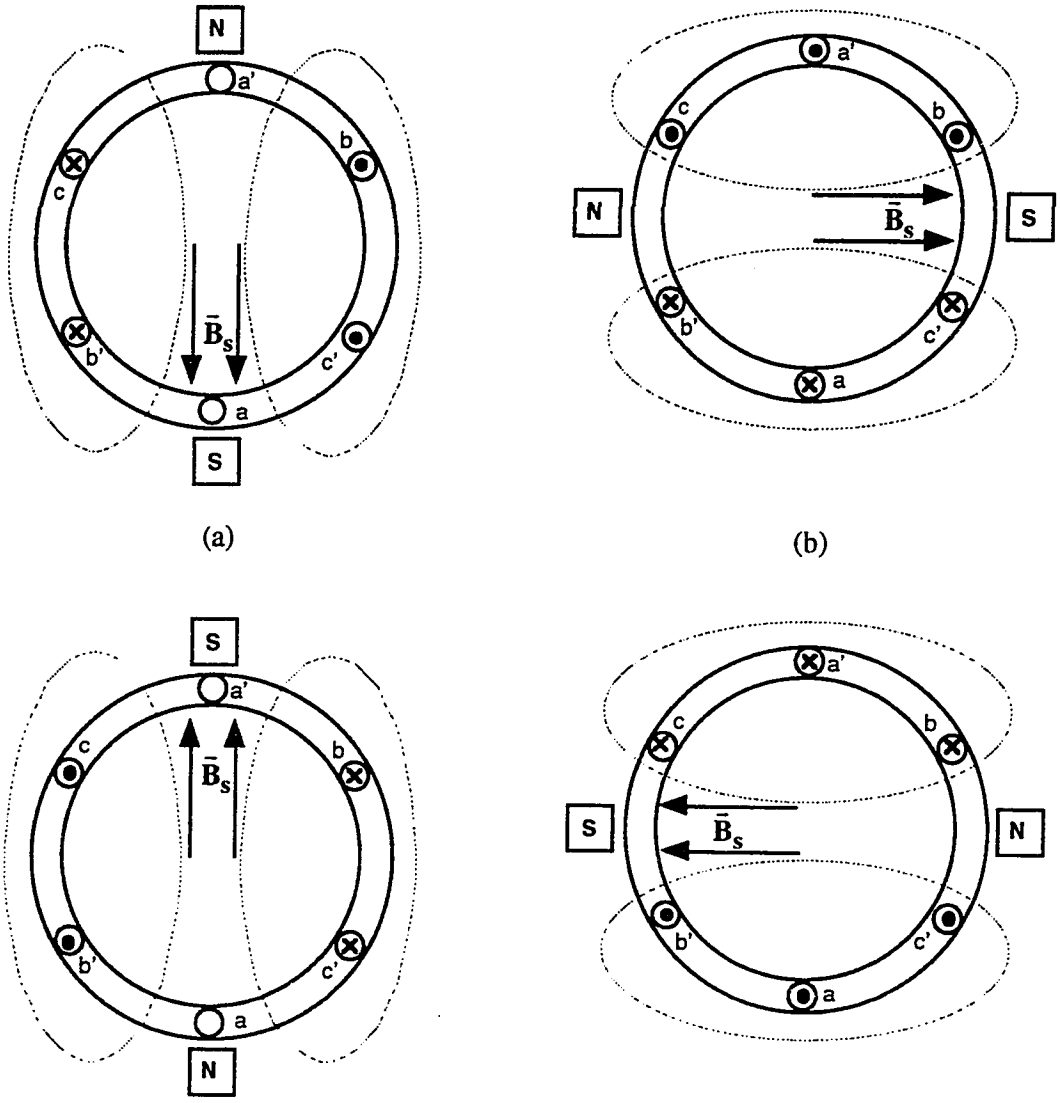

Figure 2.2. Rotating Stator Magnetic Field Upon the Application of Three-Phase Power at Various Instances of Time. (a) Net Stator Field at $\omega t = 0°$. (b) Net Stator Field at $\omega t = 90°$.(c) Net Stator field at $\omega t = 180°$. (d) Net Stator Field at $\omega t = 270°$. (Source: S. J. Chapman, *Electric Machinery Fundamentals*, 2nd ed. New York: McGraw Hill, 1991.)

Two-Axis Theory

The primary purpose of this section is to briefly introduce the notion of representing the three-phase variables of the induction machine in two-phase form. This transformation and its variations were derived and defined in detail by R.H. Park, H.C. Stanley, G. Kron, and D.S. Brereton et al. [20]. Although each interpretation was treated separately in the literature, it is generally understood that these two-axis transformations, so called a "change of variables" eliminate all time-varying inductances and greatly simplify mathematical derivations [20]. This is done by transforming the stator and rotor variables to a general frame of reference which may be either stationary or rotating with some angular velocity [20]. This transformation requires two steps. The first step, which is presented in this section, is to mathematically derive the two-phase variables from the set of three-phase variables or vice versa. The second step will be to introduce these variables in alternate frames of reference (rotated or stationary). This step will be described in detail in Chapter 3 where it is applied to vector control.

Three-Phase to Two-Phase Transformations

A classical coordinate transformation that is typically used is the three-phase to two-phase transformation. In the induction machine, three-phase variables defining voltage, current and flux can be transformed into equivalent two-phase variables. Using stator current as the basis of this derivation, the "3 to 2" transformation reduces the three-phase stator current vectors i_{sa}, i_{sb}, and i_{sc}, which are 120° apart, down to two vectors i_{sx} and i_{sy}, which are orthogonal in space. Figure 2.3 demonstrates both stator current vector realizations. Using vector algebra and trigonometry the equivalent two-phase orthogonal pair i_{sx} and i_{sy} can be derived in terms of the magnitudes of the three-phase set i_{sa}, i_{sb}, and i_{sc}. This pair is shown in equations (2-8) and (2-9).

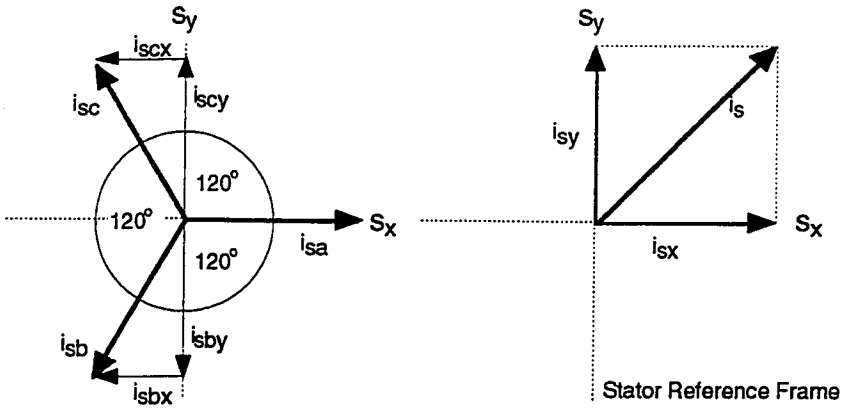

Figure 2.3. Vector Representation of the Three-Phase Stator Currents and the Equivalent Two-Phase Orthogonal Pair.

$$\begin{aligned} i_{sx} &= i_{sa} - i_{sb}\sin(30^\circ) - i_{sc}\sin(30^\circ) \\ &= i_{sa} - \frac{1}{2}i_{sb} - \frac{1}{2}i_{sc} \end{aligned} \tag{2-8}$$

$$\begin{aligned} i_{sy} &= i_{sc}\cos(30^\circ) - i_{sb}\cos(30^\circ) \\ &= i_{sc}\frac{\sqrt{3}}{2} - i_{sb}\frac{\sqrt{3}}{2} \end{aligned} \tag{2-9}$$

In matrix form, (2-8) and (2-9) can be written as

$$\begin{bmatrix} i_{sx} \\ i_{sy} \\ i_{s0} \end{bmatrix} = C \begin{bmatrix} 1 & -\frac{1}{2} & -\frac{1}{2} \\ 0 & -\frac{\sqrt{3}}{2} & \frac{\sqrt{3}}{2} \\ \frac{1}{2} & \frac{1}{2} & \frac{1}{2} \end{bmatrix} \begin{bmatrix} i_{sa} \\ i_{sb} \\ i_{sc} \end{bmatrix} \tag{2-10}$$

where i_{so} is usually referred to as a zero sequence current and C = 2/3 [7], [12], [31]. The zero sequence current exists provided that the balanced equation of (2-11) does not equal zero. In a "Y" connected induction machine the neutral is isolated and thus the zero sequence component is zero.

$$i_{sa} + i_{sb} + i_{sc} = 0 \tag{2-11}$$

The operator P as defined in equation (2-12) can be used in arbitrary "3-2" transformations of "Y" connected induction machines. Note that F is the variable of choice representing voltage, current, or flux and the subscript f is used denote a rotor or stator variable.

$$P \equiv \begin{bmatrix} F_{fx} \\ F_{fy} \end{bmatrix} = C \begin{bmatrix} 1 & -\frac{1}{2} & -\frac{1}{2} \\ 0 & -\frac{\sqrt{3}}{2} & \frac{\sqrt{3}}{2} \end{bmatrix} \begin{bmatrix} F_{fa} \\ F_{fb} \\ F_{fc} \end{bmatrix} \tag{2-12}$$

Two-Phase to Three-Phase Transformations

The inverse of the three-phase to two-phase transformation is the two-phase to three-phase transformation. It should be pointed out that in either the "3 to 2" or "2 to 3" transformation, the two-phase variables do not really exist, but are mathematical quantities used to simplify theory and derivations. This transformation is simply the mathematical matrix inversion of equation (2-10). The result of the matrix inversion is shown in (2-13).

$$\begin{bmatrix} i_{sa} \\ i_{sb} \\ i_{sc} \end{bmatrix} = \frac{1}{C} \begin{bmatrix} \frac{2}{3} & 0 & \frac{2}{3} \\ -\frac{1}{3} & -\frac{\sqrt{3}}{3} & \frac{2}{3} \\ -\frac{1}{3} & \frac{\sqrt{3}}{3} & \frac{2}{3} \end{bmatrix} \begin{bmatrix} i_{sx} \\ i_{sy} \\ i_{s0} \end{bmatrix} \tag{2-13}$$

Thus, the operator Q as defined in (2-14) is used in general "2-3" transformations of "Y" connected induction machines.

$$Q \equiv \begin{bmatrix} F_{fa} \\ F_{fb} \\ F_{fc} \end{bmatrix} = \frac{1}{C} \begin{bmatrix} \frac{2}{3} & 0 \\ -\frac{1}{3} & -\frac{\sqrt{3}}{3} \\ -\frac{1}{3} & \frac{\sqrt{3}}{3} \end{bmatrix} \begin{bmatrix} F_{fx} \\ F_{fy} \end{bmatrix} \tag{2-14}$$

Two to Three-Phase Power Constant

In the above analysis a constant factor C was used. Classically, C is set to equal to 2/3 for the unique transformations as found in [7], [20], [22], [31]. The choice of this constant is somewhat arbitrary and in some cases it can be set to one. On the other hand, in situations where the calculation of power is of great concern, this scale factor needs to be appropriately determined. This is to ensure that the transformation is power invariant [12], [31]. Using the circuits of Figure 2-4 to describe a "3 to 2" transformation, the total power of the three-phase circuit is equated with the total power of the two-phase equivalent circuit.

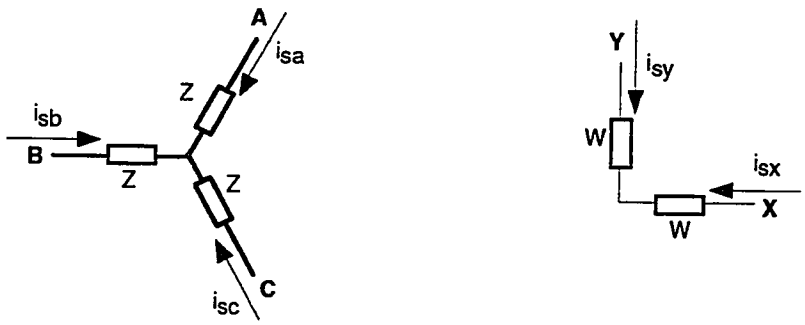

Figure 2.4. Three and Two-Phase Power Circuits.

In the three-phase equivalent circuit the total power is defined as in equation (2-15).

$$\begin{aligned} P_{total,3} &= P_a + P_b + P_c \\ &= i_a v_a + i_b v_b + i_c v_c \end{aligned} \tag{2-15}$$

In a similar fashion, by using the two-phase equivalent circuit the total power is defined as in (2-16).

$$\begin{aligned} P_{total,2} &= P_x + P_y \\ &= i_x v_x + i_y v_y \end{aligned} \tag{2-16}$$

Since the total two-phase power must be equal to the total three-phase power, equations (2-15) and (2-16) can be equated and (2-17) is found.

$$i_a v_a + i_b v_b + i_c v_c = i_x v_x + i_y v_y \tag{2-17}$$

Using (2-11) and the equations from the P operator, it can be shown that (2-17) reduces to

$$2i_b v_b + 2i_c v_c + i_b v_c + i_c v_b = C^2\left(3i_b v_b + 3i_c v_c + \frac{3}{2}i_b v_c + \frac{3}{2}i_c v_b\right). \tag{2-18}$$

As a result of equating the like terms of (2-18), the constant C is determined as

$$C = \sqrt{\frac{2}{3}}. \tag{2-19}$$

Therefore, since the currents i_{sx} and i_{sy} and the voltages v_{sx} and v_{sy} are conceptual quantities, and if these quantities are used to calculate the total average power, it is necessary to use the constant factor C of (2-19) to determine the correct power for a three-phase system using these two-phase variables. In other words, the average power calculated from the two-phase variables will not be equivalent to the power calculated from the three-phase variables without this constant.

Derivation of the Motor Voltage Equations

In order to become more familiar with the electrical dynamics of the three-phase induction machine, it is beneficial to understand the derivation of the motor voltage equations. These equations will first be derived in three-phase form and then converted into their equivalent two-phase forms. Moreover, these equations will be derived in a series of three events where (1) the inductance matrix is defined, (2) the rotor and stator flux linkages are defined, and (3) the rotor and stator voltage equations are derived.

The Inductance Matrix

In Figure 2.5 a simple induction machine is shown where the axis of the rotor windings is displaced by the angle θ_r. It is assumed that both the stator and rotor windings are sinusoidally distributed. Since the stator windings are displaced 120 degrees in space, a mutual coupling resulting in a mutual inductance between the stator windings exists. Similarly, there exists a mutual inductance between the rotor windings. Furthermore, since

the stator and rotor windings are displaced magnetically in space, a net coupling will also occur between the stator and rotor windings. This coupling will vary as the position of the rotor windings relative to the stator windings varies [21]. As a result, time varying sinusoidal functions of the stator to rotor mutual inductances arise. It will be shown in Chapter 3 that by using a rotational matrix a set of constant values may be used to define the stator and rotor mutual inductances. In summary a detailed expression governing all the aforementioned mutual inductances is shown in equation (2-20). This equation is defined as the inductance matrix of a three-phase induction machine. The details of this inductance matrix can be found in [20], [21], [22]. Note that l_m is defined as the peak mutual inductance, l_{ls} is defined as the stator leakage inductance, l_{lr} is defined as the rotor leakage inductance, $\theta_1 = \theta_r + 2\pi/3$ and $\theta_2 = \theta_r - 2\pi/3$.

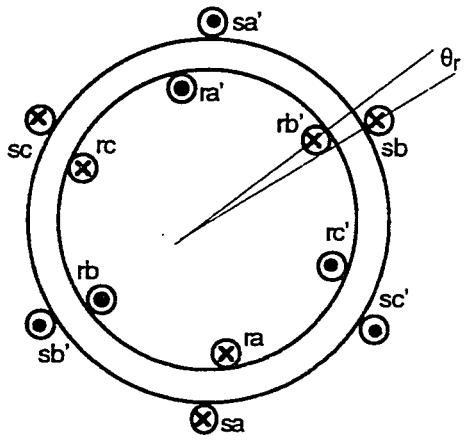

Figure 2.5. Cross-section of an Elementary Symmetrical Three-Phase Induction Machine. (Source: P. Vas, *Vector Control of AC Machines*. Oxford: Oxford University Press, 1990.)

$$L(\theta_r) \equiv \begin{bmatrix} l_m + l_{ls} & -\frac{l_m}{2} & -\frac{l_m}{2} & l_m\cos(\theta_r) & l_m\cos(\theta_1) & l_m\cos(\theta_2) \\ -\frac{l_m}{2} & l_m + l_{ls} & -\frac{l_m}{2} & l_m\cos(\theta_2) & l_m\cos(\theta_r) & l_m\cos(\theta_1) \\ -\frac{l_m}{2} & -\frac{l_m}{2} & l_m + l_{ls} & l_m\cos(\theta_1) & l_m\cos(\theta_2) & l_m\cos(\theta_r) \\ l_m\cos(\theta_r) & l_m\cos(\theta_2) & l_m\cos(\theta_1) & l_m + l_{lr} & -\frac{l_m}{2} & -\frac{l_m}{2} \\ l_m\cos(\theta_1) & l_m\cos(\theta_r) & l_m\cos(\theta_2) & -\frac{l_m}{2} & l_m + l_{lr} & -\frac{l_m}{2} \\ l_m\cos(\theta_2) & l_m\cos(\theta_1) & l_m\cos(\theta_r) & -\frac{l_m}{2} & -\frac{l_m}{2} & l_m + l_{lr} \end{bmatrix} \quad (2\text{-}20)$$

Stator and Rotor Flux Linkages

In order to calculate the stator and rotor voltages it necessary to define the stator flux and rotor flux linkage terms. Using the inductance matrix as defined above, the flux linkages are found using

$$\Psi = [L(\theta_r)][i] \quad (2\text{-}21)$$

where,

$$i \equiv [i_{sa}\ i_{sb}\ i_{sc}\ i_{ra}\ i_{rb}\ i_{rc}]^T, \quad (2\text{-}22)$$

and

$$\Psi \equiv [\Psi_{sa}\ \Psi_{sb}\ \Psi_{sc}\ \Psi_{ra}\ \Psi_{rb}\ \Psi_{rc}]^T. \quad (2\text{-}23)$$

Clearly, the flux of each phase has a total of six contributing terms. For example, Ψ_{sa} contains a self-flux linkage term produced by the stator current in the stator winding (a), two mutual flux linkage components due to the other two stator currents and three stator-rotor mutual flux linkage components.

Stator and Rotor Voltage Equations

In Figure 2.6 a "Y" connected induction machine is electrically connected as shown. The resistors R_s and R_r are the stator and rotor windings resistances respectively.

In order to determine the voltage of stator phase winding (a) a voltmeter would be attached between the neutral and the power lead of phase (a). Mathematically, this can be shown by using KVL to sum the voltages around each phase subcircuit in Figure 2.6.

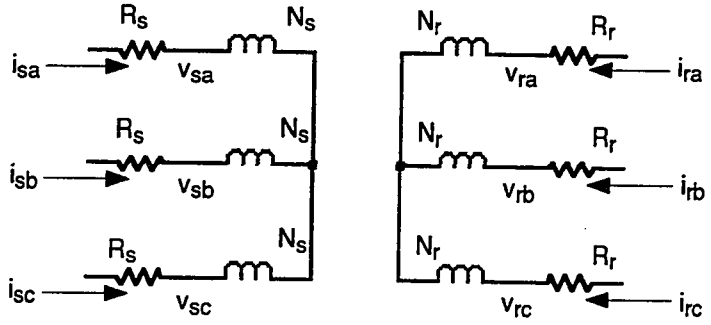

Figure 2.6. "Y" Connected Circuit of a Three-Phase Induction Machine.

Note that the voltage induced in each winding is given by Faraday's law which has been rewritten in terms of the linkage flux as

$$v = \frac{d\Psi}{dt}. \tag{2-24}$$

Therefore, the voltage v_{sa} across stator winding (a) exhibiting resistance R_s is written as

$$v_{sa} = R_s i_{sa} + \frac{d\Psi_{sa}}{dt}, \tag{2-25}$$

where i_{sa} is the current through stator winding (a), and Ψ_{sa} is the rotor flux linkage associated with this winding. The other voltage expressions of the stator and rotor windings are derived in a similar fashion. In matrix form the final expression relating all the voltage equations in terms of mutual inductances and winding resistances is given by

$$v = Ri + L(\theta_r)\frac{di}{dt} + \frac{dL(\theta_r)}{dt} i \tag{2-26}$$

where R is the resistance matrix given as

$$R=\begin{bmatrix} R_s & 0 & 0 & 0 & 0 & 0 \\ 0 & R_s & 0 & 0 & 0 & 0 \\ 0 & 0 & R_s & 0 & 0 & 0 \\ 0 & 0 & 0 & R_r & 0 & 0 \\ 0 & 0 & 0 & 0 & R_r & 0 \\ 0 & 0 & 0 & 0 & 0 & R_r \end{bmatrix}, \tag{2-27}$$

and

$$v \equiv \begin{bmatrix} v_{sa} & v_{sb} & v_{sc} & v_{ra} & v_{rb} & v_{rc} \end{bmatrix}^T. \tag{2-28}$$

Note that (2-26) can be transformed down to two-axis form. As a result of this transformation, it can be shown that a two-phase mutual inductance term L_m can be defined as

$$L_m \equiv \frac{3}{2} l_m. \tag{2-29}$$

Again the two-axis derivation of the motor voltage equations and existence of (2-29) is shown in detail in [21].

Electromechanical Energy Conversion

The second major principle in the operation of the induction machine is electromechanical energy conversion. In other words, electrical power is applied to the induction machine where it is converted to mechanical power. Assuming an ideal induction motor without power losses (i.e., 100% efficient), this relationship can be expressed as

$$P_m = P_e = \omega_r T_e. \tag{2-30}$$

Therefore, for electromagnetic energy conversion electromagnetic torque T_e must be produced at some rotor speed ω_r. This is best illustrated using the cross-sectional view of the simplified induction machine as shown in Figure 2.7.

In Figure 2.7 three-phase voltage has been applied to the stator windings of the two-pole induction machine. As a result, current flows and two magnetic poles develop incurring a stator flux Ψ_s between them. Assuming that the field is rotating clockwise, the

instantaneous flux direction and magnetic poles are as shown in Figure 2.7. As the flux sweeps through the rotor coil (denoted as a-a') a voltage V_{ind} is induced as given by Faraday's law

$$V_{ind} = -N\frac{d\Psi_s}{dt}. \tag{2-31}$$

Since the rotor coil is short circuited a current will flow in the direction shown, as determined by Lenz's law. This rotor current i_{ra} in turn will produce its own magnetic flux Ψ_r orthogonal to the flux as set up by the stator magnetic poles. The direction of the force on conductor (a) and (a') is given by the right hand rule and is defined as

$$F = i_{ra}(l \times \frac{\Psi_s}{A_c}), \tag{2-32}$$

where l is the length of the coil and A_c is the cross-sectional area between the two conductors (a) and (a') in the rotor. Clearly, the forces are a coupled pair separated by the diameter 2r of the rotor and, therefore, the torque on the rotor coil can be seen as

$$T_e = 2(r \times F), \tag{2-33}$$

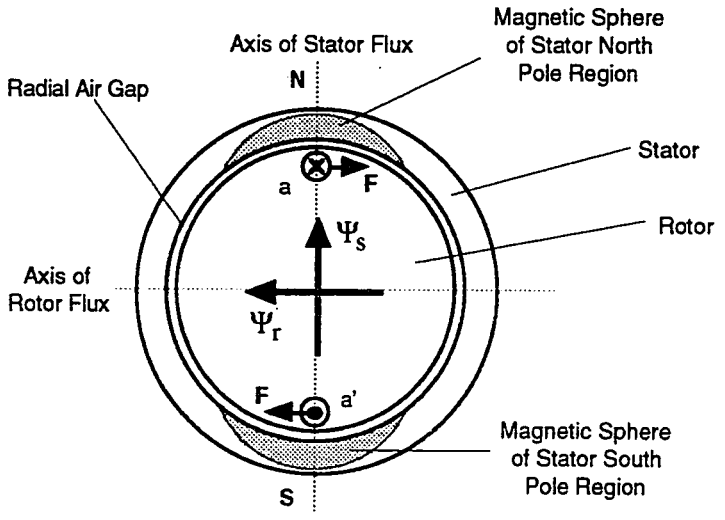

Figure 2.7. Torque Development in an Induction Motor. (Source: J. A. Karnas, D. Platnik, and P. F. Ryff, *Electric Machines and Transformers*. New Jersey: Prentice Hall, 1987.)

in the clockwise direction.

The torque equation is permutated in many alternate forms. In some textbooks such as in [8], [13], [18] the torque expression is derived in terms of the cross product of the rotor and stator magnetic flux densities (2-34). Alternate forms may be found in [22], [23], [30].

$$T_e = k(B_r \times B_s), \tag{2-34}$$

The following torque equation, which is derived through the principles of electromechanical energy conversion, will be very useful in discussion of vector control in Chapter 3 [20]. Equation (2-35) uses this fact where $L(\theta_r)$ is defined as the inductance matrix (2-20) and the current vector of (2-22) represents the three-phase stator and rotor currents. The derivation for (2-35) can be found in [20] and will not be repeated here.

$$Te = \frac{p}{2}[i]^T\left[\frac{\partial}{\partial\theta_r}L(\theta_r)\right][i] \tag{2-35}$$

Note that the (p/2) factor is included in (2-35) so as to correctly define the output torque T_e as a function of the number of electromagnetic poles. The expansion of (2-35) yields (2-36) and thus, (2-37).

$$Te = -\frac{l_m}{2}\frac{p}{2}\begin{bmatrix} i_{sa} \\ i_{sb} \\ i_{sc} \\ i_{ra} \\ i_{rb} \\ i_{rc} \end{bmatrix}^T \begin{bmatrix} 0 & 0 & 0 & \sin(\theta_r) & \sin(\theta_1) & \sin(\theta_2) \\ 0 & 0 & 0 & \sin(\theta_2) & \sin(\theta_r) & \sin(\theta_1) \\ 0 & 0 & 0 & \sin(\theta_1) & \sin(\theta_2) & \sin(\theta_r) \\ \sin(\theta_r) & \sin(\theta_2) & \sin(\theta_1) & 0 & 0 & 0 \\ \sin(\theta_1) & \sin(\theta_r) & \sin(\theta_2) & 0 & 0 & 0 \\ \sin(\theta_2) & \sin(\theta_1) & \sin(\theta_r) & 0 & 0 & 0 \end{bmatrix} \begin{bmatrix} i_{sa} \\ i_{sb} \\ i_{sc} \\ i_{ra} \\ i_{rb} \\ i_{rc} \end{bmatrix} \tag{2-36}$$

$$T_e = -l_m\frac{p}{2}\begin{bmatrix} i_{sa} & i_{sb} & i_{sc} \end{bmatrix}\begin{bmatrix} \sin(\theta_r) & \sin(\theta_1) & \sin(\theta_2) \\ \sin(\theta_2) & \sin(\theta_r) & \sin(\theta_1) \\ \sin(\theta_1) & \sin(\theta_2) & \sin(\theta_r) \end{bmatrix}\begin{bmatrix} i_{ra} \\ i_{rb} \\ i_{rc} \end{bmatrix} \tag{2-37}$$

Alternatively, equation (2-37) can be represented in two-axis form by using the P operator mentioned above (with C = 2/3). Equation (2-37) can be written as

$$T_e = -l_m \frac{p}{2}\left[\bar{i}_{sabc}\right]^T [S]\left[\bar{i}_{rabc}\right], \tag{2-38}$$

where

$$S \equiv \begin{bmatrix} \sin(\theta_r) & \sin(\theta_1) & \sin(\theta_2) \\ \sin(\theta_2) & \sin(\theta_r) & \sin(\theta_1) \\ \sin(\theta_1) & \sin(\theta_2) & \sin(\theta_r) \end{bmatrix}, \tag{2-39}$$

$$\bar{i}_{sabc} = \begin{bmatrix} i_{sa} & i_{sb} & i_{sc} \end{bmatrix}^T, \tag{2-40}$$

$$\bar{i}_{rabc} \equiv \begin{bmatrix} i_{ra} & i_{rb} & i_{rc} \end{bmatrix}^T. \tag{2-41}$$

The derivation begins by substituting the Q operator of (2-14) into (2-40) to determine an equivalent torque expression using two-phase currents. This transformation is shown in (2-42)

$$T_e = -l_m \frac{p}{2}\left[Q\bar{i}_{sxy}\right]^T [S]\left[Q\bar{i}_{rxy}\right], \tag{2-42}$$

where

$$\bar{i}_{sxy} \equiv \begin{bmatrix} i_{sx} & i_{sy} \end{bmatrix}^T, \tag{2-43}$$

$$\bar{i}_{rxy} \equiv \begin{bmatrix} i_{rx} & i_{ry} \end{bmatrix}^T. \tag{2-44}$$

Note that (2-42) can be written as

$$T_e = -l_m \frac{p}{2}\left[\bar{i}_{sxy}\right]^T \left[Q^T S Q\right]\left[\bar{i}_{rxy}\right] \tag{2-45}$$

where it can be proven that

$$Q^T S Q = \left(\frac{3}{2}\right)^2 \begin{bmatrix} \sin(\theta_r) & \cos(\theta_r) \\ -\cos(\theta_r) & \sin(\theta_r) \end{bmatrix}. \tag{2-46}$$

Furthermore, since the mutual inductance l_m is a three-phase variable, (2-29) can be used to transform it into a two-phase variable and thus, (2-45) can be written as

$$T_e = L_m \frac{P}{2}\frac{3}{2}\begin{bmatrix} i_{sx} & i_{sy} \end{bmatrix}\begin{bmatrix} -\sin(\theta_r) & -\cos(\theta_r) \\ \cos(\theta_r) & -\sin(\theta_r) \end{bmatrix}\begin{bmatrix} i_{rx} \\ i_{ry} \end{bmatrix}. \tag{2-47}$$

If the constant factor C is not used in the operator Q then

$$T_e = L_m \frac{P}{3}\begin{bmatrix} i_{sx} & i_{sy} \end{bmatrix}\begin{bmatrix} -\sin(\theta_r) & -\cos(\theta_r) \\ \cos(\theta_r) & -\sin(\theta_r) \end{bmatrix}\begin{bmatrix} i_{rx} \\ i_{ry} \end{bmatrix}. \tag{2-48}$$

Induction Motor Torque-Speed Characteristics

The rotor slip is defined in (2-49) where ω_{sync} is the synchronous speed (i.e., the electrical speed) and ω_r is the rotor speed. The slip speed is defined as in (2-50) where ω_{sync} is the difference of the synchronous speed and the actual rotor speed. Note that the relative motion of the rotor and magnetic fields (i.e., slip term) is the relative speed expressed on a percentage basis or on a unit basis [8]. At no load, the rotor spins at almost the same speed as the rotating stator magnetic field and thus, the rotor slip is very small.

$$s = \frac{\omega_{sync} - \omega_r}{\omega_{sync}} (\times 100\%) \tag{2-49}$$

$$\omega_{slip} = \omega_{sync} - \omega_r \tag{2-50}$$

Therefore, at no load the slip speed ω_{slip} is small, the induced voltage in the rotor bars is small, and the rotor currents are small. As more torque is demanded from the rotor, the speed of the rotor is lowered and, as more flux lines cut rotor bars, higher rotor current is induced. Higher rotor current results in higher produced torque. Note that an induction motor must have slip to develop torque as no flux lines would be cut by the rotor conductors if they were rotating at the synchronous speed [20]. In general, it is this speed differential or slip between the speed of rotation of the rotor and the speed of rotation of the stator magnetic field that determines motor torque. A typical torque-speed curve (computer simulated) of an induction motor is shown in Figure 2.8 where the horizontal axis is the

speed of the rotor and ω_{sync} = 1800 rpm. Note that the figure represents the case where the motor is started up with no external load torque applied to the shaft. Also note that the transient pulsation of the electromagnetic torque is a result of the transient offsets of the rotor and stator currents. In many cases, the inertia of the rotor and the load torque is generally large enough to smooth out this pulsating torque and thus, will cause insignificant variation in the rotor speed [21].

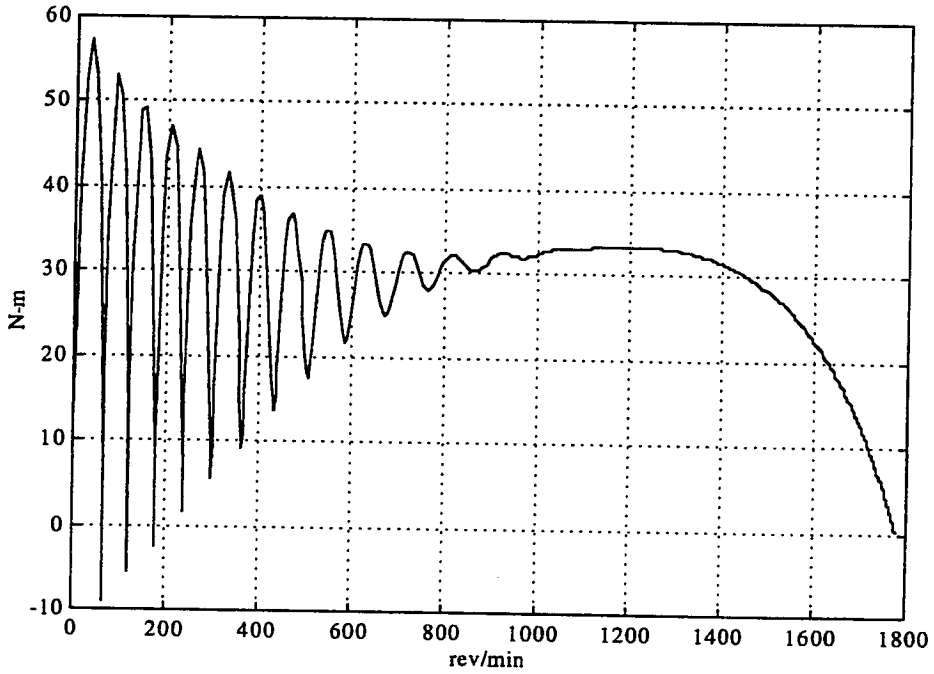

Figure 2.8 Typical Torque-Speed Curve of an Induction Motor under Free Acceleration During Startup.[1]

[1] Curve generated by simulation.

CHAPTER 3

Vector Control of Induction Machines

If an induction machine is to assume the role of a high performance servo drive, it is thus desired that the induction machine somehow inherit the dynamic characteristics of dc machines. Furthermore, it is also desired that the simple control techniques employed on these dc machines be applicable on ac machines such as the induction motor. The search to satisfy these two criterion has led to development of "vector controlled" techniques. The fundamental principal these vector control schemes are based on formulate an approach to obtain two independent orthogonal current components, one of which is torque producing and the other of which is flux producing [31]. The use of these two current components is applied for the direct instantaneous torque control of the induction machine. In other words, the motivation behind vector control is to enable the use of an induction machine to perform as if it were a separately excited dc machine [7]. Thus, through the use of vector control, the induction machine is capable of high dynamic performance.

This chapter will focus on developing a concise set of equations that enable the use of vector control in the practical setting. To achieve this goal, attention will be focused on (1) the analogy of the vector controlled induction machine as if it were a dc machine, (2) the methods of vector control, (3) developing the remaining set of equations not discussed in the two-axis theory of Chapter 2, (4) re-deriving expressions of the motor voltage equations and electromagnetic torque production in terms of vector control, (5) deriving a flux model and the implementation of a dynamic vector controller, (6) setting forth a routine to identify the motor parameters, and lastly, (7) describing some of the disadvantages of vector control.

The Separately Excited DC Motor Analogy

The principle of utilizing vector control for induction motor control can be well understood by comparing the electromagnetic torque production in both ac and dc type

motors. A separately excited dc motor is shown in Figure 3.1 where a separate voltage V_f is applied to excite a magnetic flux field Ψ_f and V_a is applied to incur a current flow i_a through the armature windings. The interaction of the excitation flux field with the armature current will result in forces acting on the armature conductors thereby producing electromagnetic torque. If, for example, the flux intensity were held constant, the electromagnetic torque of this dc motor could rapidly be regulated under the variation of impressed armature current. The expression governing this physical effect is the cross product of Ψ_f and i_a as in equation (3-1), where K is a constant and T_e is the electromagnetic torque [31]. Furthermore, because the flux and current vectors are always in space quadrature (i.e., 90 degrees apart) due to the commutation mechanism of the motor, it follows that (3-1) can be reduced to (3-2).

$$T_e = K\bar{\Psi}_f \times \bar{i}_a \tag{3-1}$$

$$T_e = K\Psi_f i_a \tag{3-2}$$

It was established in Chapter 2 that in an induction motor electromagnetic torque is

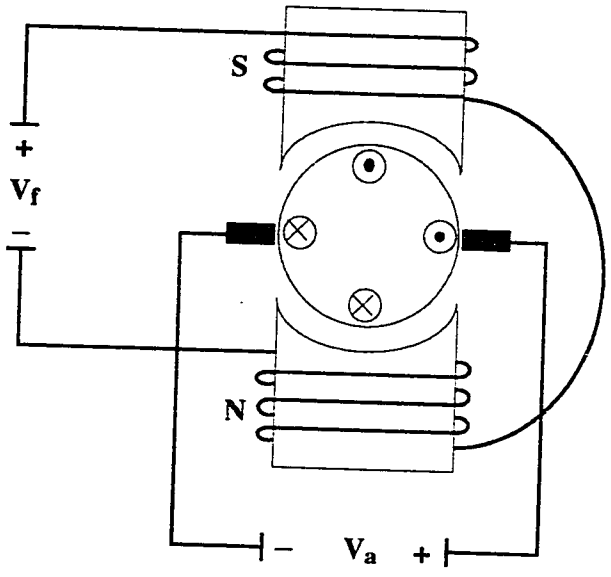

Figure 3.1. A Separately Excited Wound Field DC Motor.

generated through the interaction of a rotating magnetic field with the rotor magnetic field. It can also be shown that the general relation for torque production in an induction motor is described by equation (3.3) where Ψ_s and i_r are the magnitudes of the stator flux linkages and rotor currents respectively [31].

$$T_e = K\bar{\Psi}_s \times \bar{i}_r \tag{3-3}$$

To establish the similarity between the electromagnetic torque production of an ac machine with that of a dc machine it is necessary to redefine the cross product of (3-3) as in equation (3-4) [31].

$$T_e = K\left|\bar{\Psi}_s\right|\left|\bar{i}_r\right|\sin(\beta) \tag{3-4}$$

Note that when the torque angle β between stator flux vector and the rotor current vector is 90 degrees, maximum torque is established and thereby equation (3-5) is similar to equation (3-2) [31].

$$T_e = K\left|\bar{\Psi}_s\right|\left|\bar{i}_r\right| \tag{3-5}$$

It has been established that torque generation in an induction motor operates on the same basic principles of a dc motor. However, several complications arise in establishing an orthogonal relationship between the magnetic flux vector and stator current vector of an induction motor. First of all, for a dc motor the orthogonality of equation (3-1) will always be true due to motor design (i.e., pole placement and commutator usage). But with an induction machine, it is much more difficult to generate the proper interaction of the flux and current since the magnetic flux vector is constantly rotating. In contrast, the magnetic field set up in a dc motor is stationary. Secondly, it is not possible to monitor or measure the rotor currents. Again, this is a trivial matter in a separately excited dc machine since the armature current is delivered through the use of brushes. Third, it is given that for a separately excited dc motor the currents used to set up a magnetic flux and for torque generation (i.e., i_f and i_a) are decoupled or independent. In an induction motor, the stator

current supplies the rotor current through induction while also providing a means to generate a rotating magnetic flux. Finally, general torque control in either machine can be performed by varying the motor currents. However, for an induction machine both the magnitude and phase of the current vector must be controlled and synchronized with the flux vector to enable precise torque control. Clearly, the induction motor is much more difficult to control.

Methods of Vector Control

In order to perform precise torque control of an induction motor three control methods can be applied. These methods encapsulate using the application of a special reference frame such that the expression of electromagnetic torque derived is similar to that of a separately excited dc motor [31]. This reference frame can applied to and fixed to either the stator-flux frame, rotor-flux frame, or the magnetizing-flux frame. Moreover, these methods are called stator-flux oriented control, rotor-flux oriented control, and magnetizing-flux oriented control respectively [31].

In these control schemes the direct and quadrature stator currents are determined corresponding to the selected reference frame. Furthermore, in each of these control schemes, the special reference frame selected is synchronized with the flux vector such that direct current component is coaxial with the flux vector and the quadrature component is orthogonal. Due to this fact, in all three implementations information is required on the angle and magnitude of the flux vector specified (e.g., stator, rotor, or magnetizing) [31]. This information can be determined through the use of two specialized approaches.

These approaches are described as either being direct or indirect forms of vector control. For example, if direct rotor-flux oriented control is selected, information pertaining to the magnitude and position of the rotor-flux linkage will be determined through the use of Hall effect sensors placed in the motor. Alternatively, this information can be estimated through the use of a flux model [31]. On the other hand, if indirect rotor-

flux oriented control is selected the angle of the flux vector is estimated by integrating rotor speed in summation to the computed reference value of the slip angle [31].

Detailed Theory

The theory to be presented hereafter represents the case where direct vector control fixed to the rotor-flux frame is used. The induction motor is supplied by a current controlled PWM inverter. In addition, the induction motor under control is of the squirrel cage rotor type and a real time flux model is used to identify the flux vector. In order for this induction motor to function under conditions similar to the separately excited dc motor, key coordinate transformations coupled with an accurate flux model are needed. The schematic of this system is shown in Figure 3.7 on page 49. The theory and structure of the key elements of this system will be best understood in the following sections.

Rotated Frames of Reference

In Chapter 2, the two-axis theory of induction machines was introduced. That section described the "3 to 2" and "2 to 3" transformations in detail. This section introduces the variables of these transformations in rotated frames of references pertaining to vector control. The rotational transformation (also known as the commutator transformation) is a vital element used in implementing vector control [12]. There are two rotational transformations (or matrices) to discuss, one is the inverse of the other. The first is the rotational matrix as defined in equation (3-6) and the latter is rotational matrix of (3-7). Again, these transformations are mathematically derived using vector algebra and trigonometry and will not be discussed here.

$$R(\theta)=\begin{bmatrix}\cos(\theta) & -\sin(\theta)\\ \sin(\theta) & \cos(\theta)\end{bmatrix} \tag{3-6}$$

$$R(-\theta)=\begin{bmatrix}\cos(\theta) & \sin(\theta)\\ -\sin(\theta) & \cos(\theta)\end{bmatrix} \tag{3-7}$$

Equation (3-7) is seen to be the inverse of (3-6) where

$$R^{-1}(\theta)=R(-\theta). \tag{3-8}$$

One additional note that will be useful in the flux model derivation is the fact that, if the rotational matrix $R(\theta)$ is multiplied by its inverse $R(-\theta)$, the identity matrix results.

$$R(\theta)R(-\theta)=I \tag{3-9}$$

The role of the rotational matrix is to rotate the axes about the origin as shown in Figure 3.2 on page 38. If the axes are rotated through an angle θ, then every point of the plane has two representations: (x, y) in the original coordinate system and (x', y') in the new coordinate system. For example, if the pair of points x_1 and y_1 in Figure 3.2 are referenced to the (x, y) stationary frame, then these points are rotated to the (x', y') frame by using $R(-\theta)$ as follows

$$\begin{bmatrix}x_1'\\ y_1'\end{bmatrix}=\begin{bmatrix}\cos(\theta) & \sin(\theta)\\ -\sin(\theta) & \cos(\theta)\end{bmatrix}\begin{bmatrix}x_1\\ y_1\end{bmatrix}. \tag{3-10}$$

$R(-\theta)$ is used because the stationary frame (x, y) is seen as making a negative angle when referenced to the rotated (x', y') frame. Alternatively, the points x_1' and y_1' referenced to the rotated frame can be referenced back into the stationary frame by using $R(\theta)$ in this form

$$\begin{bmatrix}x\\ y\end{bmatrix}=\begin{bmatrix}\cos(\theta) & -\sin(\theta)\\ \sin(\theta) & \cos(\theta)\end{bmatrix}\begin{bmatrix}x'\\ y'\end{bmatrix}. \tag{3-11}$$

In short, it is possible to represent a point in space (e.g., voltage, current or flux) in alternate rotated frames of reference. In particular, the induction motor has multiple frames of reference. One frame of reference can be seen as if the observer was stationary in reference to the stator, and that the rotor is the rotating frame. Alternatively, it is possible to observe the rotor as the stationary frame of reference while the stator is the rotating frame of reference. Of course, in reality the stator is physically stationed and not rotating. As mentioned earlier three methods can be chosen to implement vector control. The basis of these methods is to a choose a special frame of reference such that the frame desired is synchronized with the specified flux vector. For example, if rotor-flux oriented control is desired, the special frame of reference is fixed to the rotor-flux frame. This frame of

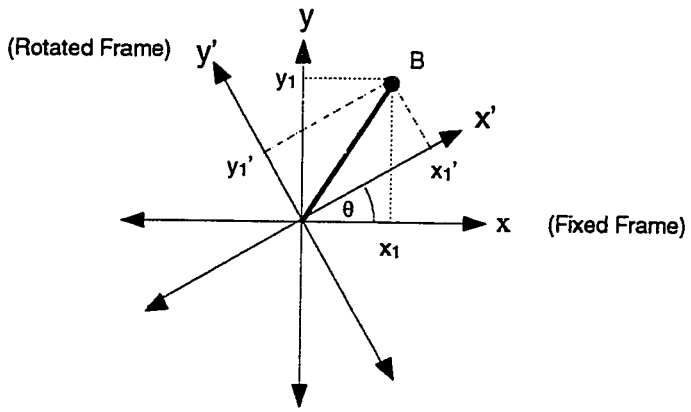

Figure 3.2. Axis Rotation About the Origin.

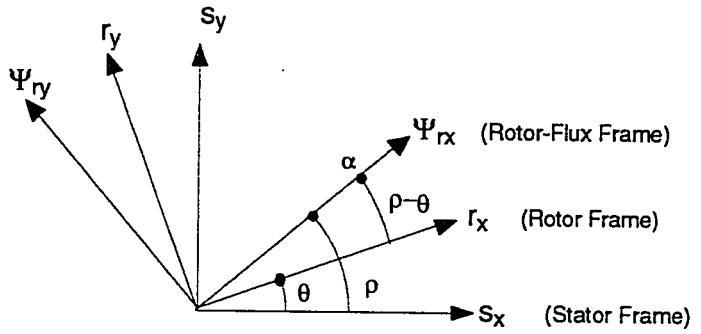

Figure 3.3. Induction Motor Frames of Reference.

reference is shown in Figure 3.3 on page 38 where the angle between the rotor and stator frame is the rotor angle θ_r, the angle between the rotor-flux frame and the stator frame is denoted as ρ, and the difference of these two angles is denoted as the slip angle α.

Time Derivative in the Rotating Frame

In the derivation of the flux model it is necessary to use the time derivative in the rotated frame. The purpose of this section is to demonstrate that the derivative of the rotational matrix is identical to the product of a skew symmetric matrix and the respected rotational matrix. The derivative of the rotational matrix is performed by simply taking the derivative of each element of the rotational matrix:

$$\frac{d}{dt}R(\theta)=\begin{bmatrix}-\dot{\theta}\sin(\theta) & -\dot{\theta}\cos(\theta)\\ \dot{\theta}\cos(\theta) & -\dot{\theta}\sin(\theta)\end{bmatrix}. \tag{3-12}$$

Alternatively, this derivative may also be found using the skew-symmetric matrix which is denoted as

$$S(\dot{\theta})=\begin{bmatrix}0 & -\dot{\theta}\\ \dot{\theta} & 0\end{bmatrix}. \tag{3-13}$$

By multiplying the skew matrix with the rotational matrix,

$$S(\dot{\theta})R(\theta)=\begin{bmatrix}0 & \dot{\theta}\\ \dot{\theta} & 0\end{bmatrix}\begin{bmatrix}\cos(\theta) & -\sin(\theta)\\ \sin(\theta) & \cos(\theta)\end{bmatrix} \tag{3-14}$$

equation (3-14) is determined and thus the matrices of (3-12) and (3-15) are identical.

$$S(\dot{\theta})R(\theta)=\begin{bmatrix}-\dot{\theta}\sin(\theta) & -\dot{\theta}\cos(\theta)\\ \dot{\theta}\cos(\theta) & -\dot{\theta}\sin(\theta)\end{bmatrix} \tag{3-15}$$

Moreover, using shorthand notation, the derivative of the rotational matrix can be written in the following form where

$$\frac{d}{dt}R(\theta)=S(\dot{\theta})R(\theta). \tag{3-16}$$

Motor Voltage Equations Revisited

In Chapter 2 an expression was derived that governed the stator and rotor voltages of the three-phase induction machine (i.e., equation 2-26 on page 25). If (2-26) is expanded out such that all six voltages of (2-28) are expressed, it will become apparent that there are inductances as functions of sine and cosine terms. Furthermore, the expressions of (2-26) will also contain current terms which are expressed in their own respected frames (i.e., rotor or stator frames). However, it was noted in Chapter 2 that a change of variables exists such that the time varying inductances of (2-26) become constant. This change of variables utilizes the "3 to 2" transformation in conjunction with the rotational matrices defined above. As a direct result of this transformation the derivation of vector control and the derivation of the flux model used in vector control are simplified. Moreover, this change of variables makes it possible to "treat the induction machine from the standpoint of an equivalent "T" circuit with constant inductances"[21]. The derivation of this model can be found in [21]. Note that this equivalent "T" circuit is analogous to a "T" circuit transformer model with the exception of the speed voltage terms $\omega_r\Psi_{rx}$ and $\omega_r\Psi_{ry}$. The equivalent "T" circuit(s) is shown in Figure 3.4 where the transformer analogy of this

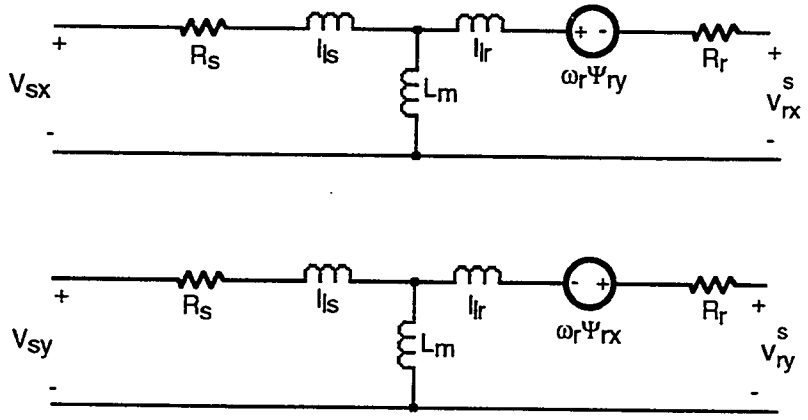

Figure 3.4. Transformed Two-Phase Induction Motor Circuit Denoted as an Equivalent "T" Circuit in the Stator Frame of Reference. (Source: P. C. Krause and O. Wasynczuk, *Electromechanical Motion Devices*. New York: McGraw Hill, 1989.)

model is shown in Figure 3.5.

In the derivation of the flux model several expressions are necessary from this transformer model. The first is a rotor voltage equation and the second is the rotor current expression. In the rotor reference frame the rotor voltage expression is defined as

$$\bar{v}_r^r = R_r \bar{i}_r^r + \frac{d}{dt}\bar{\Psi}_r^r, \tag{3-17}$$

where

$$\bar{v}_r \equiv \left[v_{rx} \;\; v_{ry}\right]^T, \tag{3-18}$$

$$\bar{i}_r \equiv \left[i_{rx} \;\; i_{ry}\right]^T. \tag{3-19}$$

$$\bar{\Psi}_r \equiv \left[\Psi_{rx} \;\; \Psi_{ry}\right]^T. \tag{3-20}$$

Note that the superscript "r" next to any variable such as voltage, current or flux denotes that the variable is referenced to the rotor frame. In order to find an expression for the rotor current, it is necessary to find a combined expression of the various flux linkage terms as shown in Figure 3.5. This combined flux linkage term is denoted as the rotor-flux linkage Ψ_r. The rotor-flux linkage is the summation of the mutual fluxes Ψ_m of the stator and rotor windings and the leakage flux Ψ_L leakage flux of the rotor windings (3-21).

$$\begin{aligned}\bar{\Psi}_r &= \bar{\Psi}_m + \bar{\Psi}_L \\ &= \bar{i}_r L_m + \bar{i}_r l_{lr} + \bar{i}_s L_m\end{aligned} \tag{3-21}$$

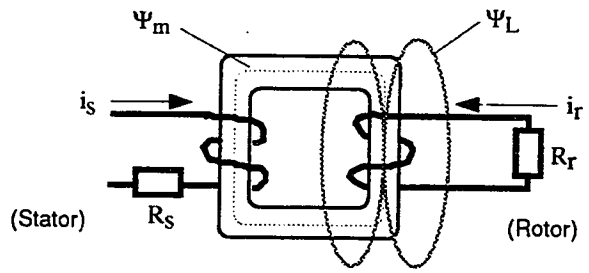

Figure 3.5. Transformer Analogy For Equivalent Two-Axis Induction Machines.

Alternatively, if the rotor mutual and leakage inductances are combined as in (3-22), then (3-21) can be written as (3-23).

$$L_r \equiv l_{lr} + L_m \tag{3-22}$$

$$\bar{\Psi}_r = \bar{i}_r L_r + \bar{i}_s L_m \tag{3-23}$$

Note that (3-23) can be rearranged to yield a rotor current expression which is useful in any frame of reference. Also note that L_r is defined as the rotor inductance.

Flux Model Derivation

The rotor voltage equations expressed in the rotor-flux oriented frame can be used to determine the magnitude and angle of the flux linkage vector in space [31]. The derivation of this flux model will be presented in this section. The derivation is much easier to implement using vector and matrix notations initially, and will be broken up into components as the derivation is completed. The derivation begins by using the first order differential equations of the two-axis rotor voltages of equation (3-17). Since all components of equation (3-17) are in the rotor frame, it is necessary to transform each component into the rotor-flux frame by using the rotational matrices.

In order to make use of equation (3-16) which expresses the time derivative in a rotated frame and in order for derivation simplification in the subsequent steps, it is important that equation (3-17) be rewritten as in equation (3-24) using (3-16).

$$\bar{v}_r^r = R_r \bar{i}_r^r + \frac{d}{dt}\left(R(\rho - \theta)\bar{\Psi}_r^{\Psi_r} \right) \tag{3-24}$$

Equation (3-24) is equivalent to equation (3-17) because the rotor magnetic flux linkage fixed to the rotor frame in space can also be seen as a if it the flux linkage was fixed to the rotor-flux frame and then rotated (by using equation (3-6)) into the rotor frame (see Figure 3.3). Note that the superscript, "Ψ_r" or "r" to the right of the vector bar denotes that the quantity under the bar is referenced to the rotor-flux frame or rotor frame respectively.

Using the chain rule of derivative formulas and using the formula for time derivatives in rotated frames, equation (3-24) can be written as

$$\bar{v}_r^r = R_r \bar{i}_r^r + S(\dot{\rho}-\dot{\theta})R(\rho-\theta)\bar{\Psi}_r^{\Psi r} + R(\rho-\theta)\dot{\bar{\Psi}}_r^{\Psi r}. \tag{3-25}$$

At this point it is possible to change the frame of reference for the remaining variables of equation (3-25) from the rotor frame to the rotor-flux frame. By multiplying each variable of equation (3-25) by the rotational matrix given in equation (3-7) a number of simplifications will result. The multiplication step is shown in equation (3-26).

$$\begin{aligned} R(\theta-\rho)\bar{v}_r^r &= R(\theta-\rho)R_r\bar{i}_r^r \\ &+R(\theta-\rho)\left[S(\dot{\rho}-\dot{\theta})R(\rho-\theta)\bar{\Psi}_r^{\Psi r} + R(\rho-\theta)\dot{\bar{\Psi}}_r^{\Psi r}\right] \end{aligned} \tag{3-26}$$

Note that when the rotational matrix in (3-26) is multiplied with inverse rotational matrix an identity matrix will result as in (3-9). The final rotor voltage expression as now observed in the rotor-flux frame is expressed as

$$\bar{v}_r^{\Psi r} = R_r \bar{i}_r^{\Psi r} + S(\dot{\rho}-\dot{\theta})\bar{\Psi}_r^{\Psi r} + \dot{\bar{\Psi}}_r^{\Psi r}. \tag{3-27}$$

The remaining steps presented hereafter are required for simplifying (3-27) down to a pair of expressions which can be used in real time by a computer to determine the magnitude and angle of the rotor-flux linkage vector. For this purpose information is required pertaining to the measurements of the stator currents. Therefore, by substituting the rotor current expression taken from equation (3-23) and defined in the rotor-flux frame,

$$\bar{i}_r^{\Psi r} = \frac{1}{L_r}\left(\bar{\Psi}_r^{\Psi r} - L_m \bar{i}_s^{\Psi r}\right), \tag{3-28}$$

into (3-27) and removing the reference frame notation for simplicity, equation (3-29) results:

$$\bar{v}_r = \frac{R_r}{L_r}\left(\bar{\Psi}_r - L_m \bar{i}_s\right) + S(\dot{\rho}-\dot{\theta})\bar{\Psi}_r + \dot{\bar{\Psi}}_r. \tag{3-29}$$

Furthermore, by expanding the vector and matrix quantities of (3-29), the rotor voltage equation will take on the following form where

$$\bar{v}_r = \frac{R_r}{L_r}\begin{bmatrix}|\Psi_r| \\ 0\end{bmatrix} - \frac{L_m R_r}{L_r}\begin{bmatrix}I_{sd} \\ I_{sq}\end{bmatrix} + \begin{bmatrix}0 & (\dot{\rho}-\dot{\theta}) \\ (\dot{\rho}-\dot{\theta}) & 0\end{bmatrix}\begin{bmatrix}|\Psi_r| \\ 0\end{bmatrix} + \begin{bmatrix}|\dot{\Psi}_r| \\ 0\end{bmatrix}. \tag{3-30}$$

Note that the two-phase stator current in the rotor-flux frame is defined as

$$\bar{i}_s^{\Psi r} = \begin{bmatrix}I_{sd} & I_{sq}\end{bmatrix}^T. \tag{3-31}$$

Since, the rotor bars in a squirrel cage induction motor are short circuiting connections and by using Kirchoffs Laws, the sum of the voltages in the rotor circuit model are equal to zero. Therefore, after expanding (3-30) and setting the rotor voltage vector to zero two equations result:

$$0 = |\Psi_r|\frac{R_r}{L_r} - I_{sd}\frac{L_m R_r}{L_r} + |\dot{\Psi}_r|, \tag{3-32}$$

$$0 = -I_{sq}\frac{L_m R_r}{L_r} + |\Psi_r|(\dot{\rho}-\dot{\theta}). \tag{3-33}$$

After rewriting (3-32) and (3-33) equations (3-34) and (3-35) are determined. Equation (3-34) will yield information pertaining to the magnitude of the rotor-flux linkage while equation (3-35) yields information pertaining to the rotor-flux linkage angle.

$$|\dot{\Psi}_r| = \frac{R_r}{L_r}(I_{sd}L_m - |\Psi_r|) \tag{3-34}$$

$$\dot{\rho} = \dot{\theta} + I_{sq}\left(\frac{L_m R_r}{L_r|\Psi_r|}\right) \tag{3-35}$$

Furthermore, equation (3-35) can also be seen in the form

$$\dot{\rho} = \dot{\theta} + \dot{\alpha} \tag{3-36}$$

where the derivative of the slip angle α (i.e., slip angular velocity or slip speed) is the quantity described as

$$\dot{\alpha} = I_{sq}\left(\frac{L_m R_r}{L_r|\Psi_r|}\right). \tag{3-37}$$

However, all these quantities require integration since the rotor-flux linkage magnitude and angle, and angular velocity are in derivative form. Through the use of a computer program and discrete integration using rectangular or trapezoidal methods, the rotor-flux linkage magnitude, angle, velocity can easily be resolved from their derivatives [27].

The resulting flux model for rotor-flux oriented vector control is shown in Figure 3.6. This figure is derived from equations (3-34) and (3-35). From equation (3-34) it is clear that the modeled rotor-flux linkage magnitude $|\Psi_r|$ can be determined if (1) the rotor resistance R_r is known, (2) the mutual inductance L_m is known, (3) the rotor inductance L_r is known, and (4) the direct axis stator current component I_{sd} is observed. The direct axis current component I_{sd} is observed by first measuring the stator currents, performing a "3 to 2" transformation, and then using the rotational matrix with a one sampled delayed version of the observed rotor-flux angle ρ [31]. Similarly, from equation (3-37) the modeled rotor-flux linkage angle can be determined if (1) R_r, L_r, L_m, I_{sq} and $|\Psi_r|$ are known, (2) the number of poles p in the induction motor are known, (3) and the rotor angular speed $\dot{\theta}_r$ is

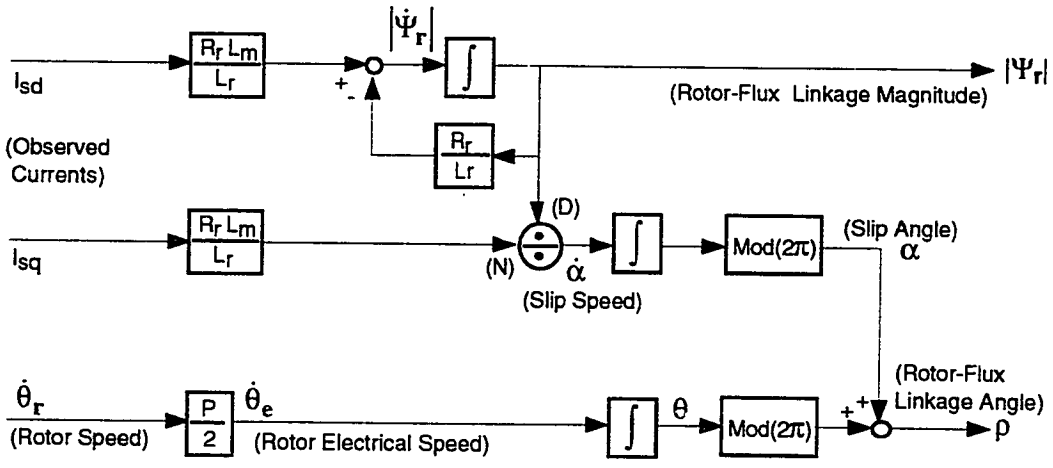

Figure 3.6. Flux Model in the Rotor-Flux Oriented Frame.

measured. Note that the rotor-flux linkage angle is the sum of the slip angle and the rotor electrical angle [31]. The rotor electrical angle is used since the number of poles present in the induction motor influence the rotor speed in relationship to the actual electrical frequency (2-7). Also note that the slip speed and the electrical speed quantities are integrated and passed through "Mod(2π)" limiting blocks prior to summation. These blocks limit the angle variables between 0 and 2π radians.

Electromagnetic Torque Production Revisited

In order for the vector control algorithm to determine the proper magnitude of the stator current for a given torque reference, a simple torque expression is derived from equation (2-47). This expression uses known variables to define the electromagnetic torque of the induction machine. Equation (2-47) can be restated using the skew symmetric matrix as

$$T_e = L_m \frac{P}{2}\frac{3}{2}\begin{bmatrix} i_{sx} & i_{sy} \end{bmatrix}\begin{bmatrix} 0 & -1 \\ 1 & 0 \end{bmatrix}\begin{bmatrix} \cos(\theta_r) & -\sin(\theta_r) \\ \sin(\theta_r) & \cos(\theta_r) \end{bmatrix}\begin{bmatrix} i^r_{rx} \\ i^r_{ry} \end{bmatrix}. \tag{3-38}$$

Note that in (3-38) the rotor current variables are defined in the rotor frame and need to be rotated to the stator frame using (3-7). Also note that the matrix term of (3-38) is identical to the rotational matrix of (3-6).

$$T_e = L_m \frac{P}{2}\frac{3}{2}\begin{bmatrix} i_{sx} & i_{sy} \end{bmatrix}\begin{bmatrix} 0 & -1 \\ 1 & 0 \end{bmatrix}R(\theta)R(-\theta)\begin{bmatrix} i^s_{rx} \\ i^s_{ry} \end{bmatrix}. \tag{3-39}$$

Equation (3-39) can be rewritten using the cross product operator as

$$T_e = L_m \frac{P}{2}\frac{3}{2}\bar{i}^s_s \times \bar{i}^s_r. \tag{3-40}$$

Again, using the rotor current equation of (3-28) but expressed in the stator frame (3-40) is rewritten as

$$T_e = \frac{P}{2}\frac{3}{2}\frac{L_m}{L_r}\bar{i}_s^s \times \left(L_r \bar{i}_r^s + L_m \bar{i}_s^s\right). \tag{3-41}$$

where

$$\bar{i}_s^s \times L_m \bar{i}_s^s = 0. \tag{3-42}$$

The torque expression in the stator frame becomes

$$T_e = \frac{P}{2}\frac{3}{2}\frac{L_m}{L_r}\bar{i}_s^s \times \bar{\Psi}_r^s. \tag{3-43}$$

In rotor-flux oriented control the rotational matrix is applied to (3-43) and the electromagnetic torque is

$$T_e = \frac{P}{2}\frac{3}{2}\frac{L_m}{L_r}\begin{bmatrix} I_{sd} \\ I_{sq} \end{bmatrix} \times \begin{bmatrix} |\Psi_r| \\ 0 \end{bmatrix} \tag{3-44}$$

hence,

$$T_e = \frac{P}{2}\frac{3}{2}\frac{L_m}{L_r} I_{sq} |\Psi_r|. \tag{3-45}$$

Recall that if the constant C is not used in the "3 to 2" transformation, the torque expression of (3-45) is multiplied by 2/3, resulting in

$$T_e = \frac{P}{3}\frac{L_m}{L_r} I_{sq} |\Psi_r|. \tag{3-46}$$

The various forms of the aforementioned torque expressions can be found in [7], [21], [22], [31].

Rotor-Flux Oriented Vector Control System

A rotor-flux oriented vector control system utilizes all the aforementioned transformations, models and equations accordingly as shown in Figure 3.7 on page 49. This figure is a schematic of a vector controlled induction machine using a position control loop and an embedded speed control loop. A simplified model of a vector controlled

induction machine is shown in Figure 3.9 on page 52. Assuming that the rotor time constant (3-47)

$$\tau_r = \frac{L_r}{R_r} \tag{3-47}$$

has been correctly identified for true flux modeling, two variables are required to enable vector control. The first is the flux reference Ψ_{ref} and the latter is the torque reference T_{ref}. In the ideal situation, any flux reference or torque reference may be utilized, but in reality, these variables are constrained by magnetic saturation, maximum amplifier current generating capabilities, and the hard constraint on how much torque a given induction motor can physically, realistically and reliably produce [31]. Both these parameters can be user specified or can be generated through control loops for a high level of performance. The torque reference in Figure 3.7 is generated through the use of a position and speed control loop. This position control system will be described in detail to (1) describe how vector control theory is practically implemented and (2) indicate how to use vector control for closed loop induction motor control.

The cascaded control structure as shown in Figure 3.7 uses the integrated value of the measured rotor speed to give the actual value of the rotor angle θ_r. This value is compared with the desired reference angle θ_{ref} and the resulting error in radians is passed through a position controller G_p (i.e., PI controller). The output of the position controller is the desired rotor speed ω_{ref}. The desired rotor speed is then compared to the actual rotor speed and the error serves as the input to the speed controller, where the constant of proportionally used in the controller G_s (i.e., PI controller) relates speed in rad/s to torque in Newton-meters (N-m). The output of this speed control block is thus the torque reference. Equation (3-46) is used to determine the desired quadrature reference stator

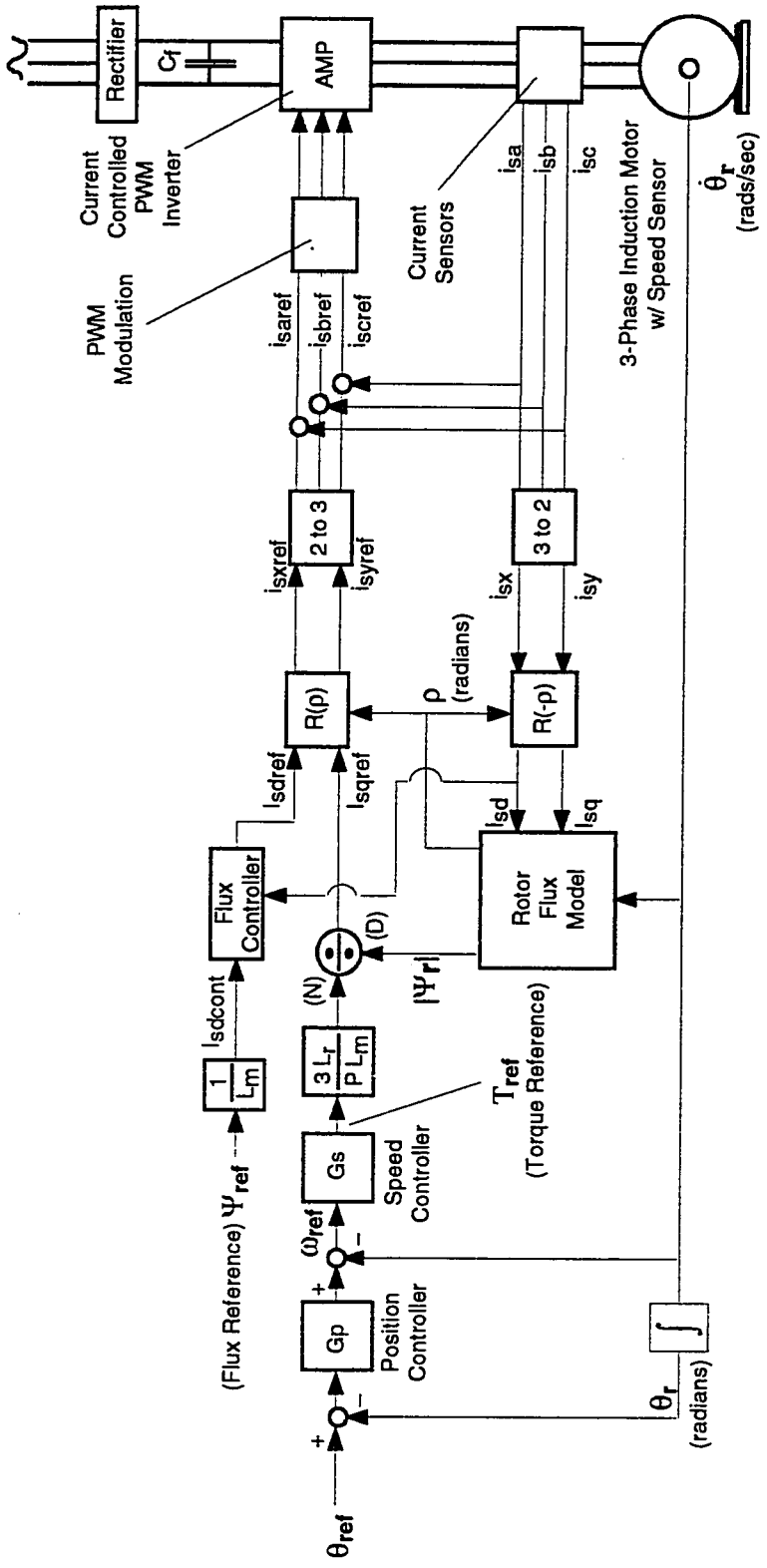

Figure 3.7. Schematic of a Rotor-Flux Oriented Vector Controlled Induction Motor Utilizing a Current Controlled PWM Inverter Amplifier.

current i_{sqref} for a given desired Torque T_{ref}. Note that to determine i_{sqref} information regarding the estimated flux magnitude $|\Psi_r|$ as determined from the flux model is required.

$$i_{sqref} = \frac{3}{P}\frac{L_r}{L_m}\frac{T_{ref}}{|\Psi_r|} \tag{3-48}$$

Similarly, the desired direct reference stator current i_{sdref} is set up by first generating a controlled current input i_{sdcont} to the flux controller (3-49). Note that the flux controller merely uses PI feedback control coupled with the estimated direct reference current i_{sd} to generate and maintain the proper reference stator current i_{sdref} for a desired flux magnitude Ψ_{ref}.

$$i_{sdcont} = \frac{|\Psi_{ref}|}{L_m} \tag{3-49}$$

In rotor-flux oriented vector control for a constant torque and constant flux reference, the reference stator currents i_{sqref} and i_{sdref} are dc quantities and are viewed as pair of orthogonal vectors fixed and synchronized to a rotating rotor-flux frame. The stator current i_{sdref} is coaxial with the flux vector and i_{sqref} is orthogonal in reference to the flux vector. The stator current vector i_{sdref} contributes to the production of the magnetic flux linkage while i_{sqref} contributes to the production of electromagnetic torque. As mentioned before, maximum torque is obtained when the flux vector and quadrature current

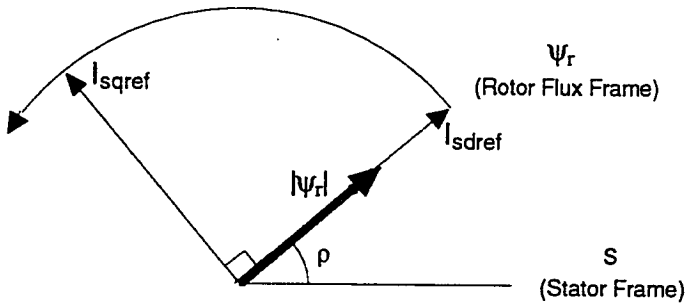

Figure 3.8. Current and Flux Vectors in Reference to the Rotor-Flux Frame.

component are orthogonal. These vectors are shown in Figure 3.8. Because the vectors are rotating at an angular velocity (dρ/dt), it is necessary to transform these quantities into the two-axis stator current references i_{sxref} and i_{syref} using the rotational matrix of equation (3-6). As a direct result of this field rotation dc stator current quantities in the rotor-flux frame are modulated into two time varying (ac) current quantities. Note that angle used in the rotational matrix is the rotor-flux angle as estimated by the flux model. These two current (i.e., i_{sxref}, i_{syref}) references are then transformed into their three-phase values (i.e., i_{saref}, i_{sbref}, and i_{scref}) by applying the "2 to 3" transformation (i.e., the Q operator with C = 1). Once transformed, the three-phase stator current references values are sent to the current controlled PWM inverter (power amplifier) which drives the induction machine. Finally, in order for the flux model to estimate the rotor-flux angle and magnitude, i_{sa}, i_{sb}, and i_{sc} are transformed back into two-axis form using the "3 to 2" transformation (i.e., the P operator with C = 1), and then synchronized to the rotor-flux frame using equation (3-7). Note that, in a "Y" connected induction machine, there is an absence of zero-sequence currents (i.e., $i_{so} = 0$) and thus, it is sufficient to only monitor two of the three impressed stator currents [31]. In other words, the condition for balanced three-phase currents as denoted in equation (2-11) may be substituted into equations (2-8) and (2-9) for the simultaneous derivation of i_{sx}, i_{sy} as in equations (3-50) and (3-51).

$$i_{sx} = 1.5 i_{sa} \tag{3-50}$$

$$i_{sy} = \left(-\sqrt{3}/2\right)\left(i_{sa} + 2 i_{sb}\right) \tag{3-51}$$

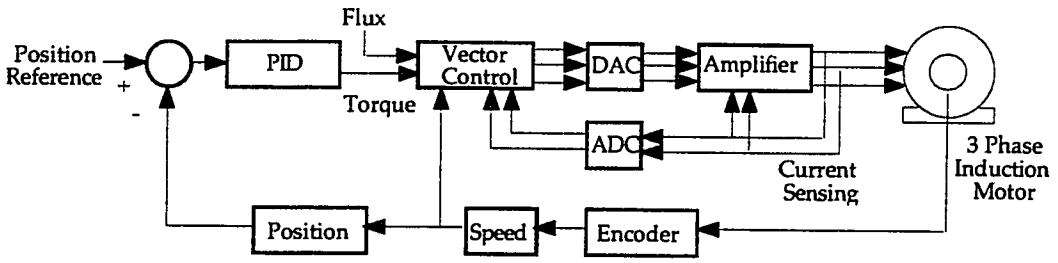

Figure 3.9. Simplified Block Diagram of a Vector Controlled Induction Machine.

Flux Model Parameter Determination

The discussion up to this point has assumed that the machine parameters such as rotor resistance R_r or mutual inductance $L_m = 1.5l_m$ were known. This section develops two simple tests which can be used in determining the machine parameters. This material has been adapted from [13] and is a widely used technique which can be found in many other motor textbooks as in [18], [21], [23], [30], [31], et al. The equivalent circuit of the induction machine has the basic topology of that of a modeled transformer. Therefore, "understanding the principles that govern the open circuit and short circuit test of the transformer leads to the understanding of the principles that govern the equivalent test applied to the induction device." [23]. These tests typically used are the "no load" and "locked rotor tests." The equivalent circuit of Figure 3.10 is used as a basis in determining the machine parameters.

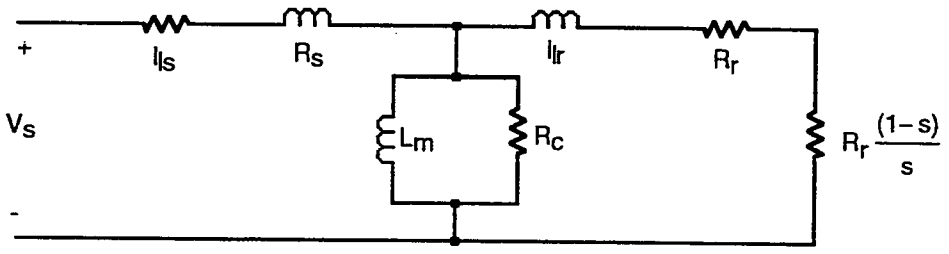

Figure 3.10. Per Phase Equivalent Circuit of an Induction Machine.

No Load Test

The no load test is comparable to the open circuit test of a regular transformer. At no load the circuit of Figure 3.10 reduces down to the circuit of Figure 3.11. This is due to the fact that at no load little rotor current flows in the rotor, and thus the resistance in the rotor circuit is effectively a high impedance path. As a result of this high impedance, the rotor circuit can be considered as an open circuit. Therefore, by taking test data of the voltage, current and frequency, and by measuring the stator resistance R_s using an ohmmeter, it is quite simple to identify the mutual inductance L_m using classical circuit theory. Note that the leakage inductance is taken to be about 5% of L_m and can be ignored initially [16]. Also, note that R_c models the cores losses and can be included in the analysis but, for simplicity, it can be ignored. A detailed description of the no load test can be found in [13].

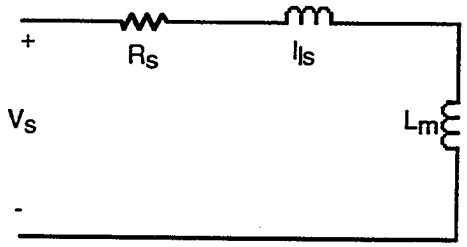

Figure 3.11. The Equivalent Circuit of an Induction Machine under No-Load Test Conditions of Operation on a Per-Phase Basis.

Locked Rotor Test

This test is very similar to the short circuit test of a transformer. In this case an external torque is applied to lock the rotor stationary in place. The voltage impressed on the stator windings is ramped up slowly as data is accumulated. As shown in Figure 3.12 the leakage and mutual inductances are ignored. At standstill the rotor circuit is at a lower

impedance compared to the impedance of the mutual inductance L_m. Therefore, little current flows in the branched circuit in comparison to the rotor circuit and thus the branched circuit can be ignored. Again, if data is taken pertaining to voltage, current and frequency, using classical phasor analysis from circuit theory, it is possible to identify the rotor resistance. A detailed description of the locked rotor test can be found in [13].

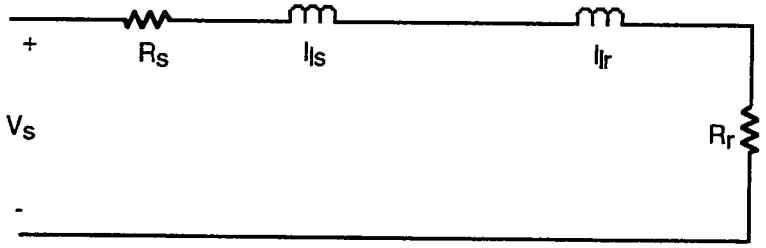

Figure 3.12. The Equivalent Circuit of an Induction Machine for the Locked Rotor Test Operation on a Per-Phase Basis.

Vector Control Limitations

As in any system, performance degradation of vector controlled induction machines can be attributed to parameter sensitivity. The most important feature of the flux model equations (3-34) and (3-35) is the strong dependency on the rotor time constant. If inaccurate values of the rotor resistance R_r and rotor self-inductance L_r are used in the flux model, it could lead to coupling between the direct and quadrature axis, incorrect field orientation and in effect, a deteriorated dynamic (possibly unstable) performance of the drive [31]. The rotor time constant can change due to a number of factors such as temperature, magnetic saturation, and the effects of current displacement [31]. The most difficult factor to control is temperature dependency. The typical induction motor is designed to run in high speed applications, where the rotor utilizes a built in air propelling action and the stator frame has cooling heat sinks, both of which aid in maintaining temperature stability. However, if such a machine is used for a high torque low speed

application, the designed cooling mechanisms cannot effectively and rapidly cool the motor down. It may be necessary to provide a new means to dissipate the heat. In terms of dynamic performance (of the direct vector controller), torque control precision is strongly dependent on the rotor time constant (3-47) [2], [7]. Figure 3.13 demonstrates the case where under locked rotor conditions the torque output of the induction machine varies with temperature. These results were experimentally determined and the temperature was measured using a thermocouple placed on the stator windings inside the motor. Note that on-line adaptive controllers have been proposed to adjust the rotor time constant for proper torque control [2]. Finally, in Chapter 4 we shall see the pronounced torque ripple effect of vector controlled machines.

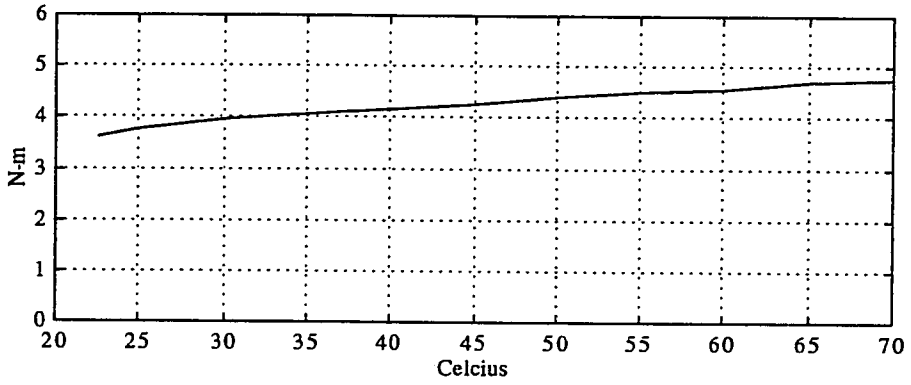

Figure 3.13. Experimental Torque Output as a Function of Temperature[1].

[1] Thermocouple inserted inside motor and placed on stator windings.

CHAPTER 4

Torque Ripple Modeling and Minimizing Theory

A study on torque ripple production and reduction of induction machines under vector control is presented in this chapter. Clearly, as discussed in Chapter 1, torque ripple can have detrimental effects on the precision performance of a controlled system. Among the many aftereffects, torque ripple will stress and fatigue the machine components and will most certainly effect or damage the finished product (e.g., machined surface). Therefore, in order for a vector controlled induction machine to behave as precise as a typical servo motor, it is necessary to understand and to diminish the source of the torque ripple. The goal of this chapter is to (1) describe researched details of torque ripple production, (2) propose a fundamental and harmonic torque ripple model, (3) propose a torque ripple compensation model, (4) describe a parameter identification scheme and prove parameter convergence, and (5) propose alternative methods of torque ripple compensation.

Researched Details of Torque Ripple Production

Torque ripple is a well studied phenomena in many types of motors, both ac and dc. The culmination of the observed literature suggests that torque ripple can be described as being either cogging or pulsating (ripple-like). In the general sense, these specific distinctions are both time varying torque fluctuations. Specifically, cogging torque is used to define the effects of slot harmonics in induction and synchronous machines [31]. The presence of uniform slots around the inside of the stator is the source of regular variations of flux and reluctance along the stator's surface. Due to these variations, harmonic components of the voltage are produced. Through the interaction of the stator and rotor slot harmonics, severe parasitic torques are produced, thereby introducing noise and vibration into the machine [8]. Similarly, torque pulsation or torque ripple in an induction motor is also a well documented phenomena. The causes of torque ripple can be attributed to the unevenness of air gap and finite number of stator slots and rotor bars [8], [19],

imbalance of the three-phase power source [5], [6] and, in the case of an inverter-fed motor, non-sinusoidal PWM waveform [7], [14], [17], [31]. These factors can cause various torque ripple harmonics of the fundamental stator current frequency (i.e., the field frequency).

An inverter-fed motor, due to the symmetric nature of the PWM waveform, contains mostly odd harmonics of the field frequency. The third harmonics are cophasal and therefore do not produce significant torque ripple. The interaction between the fundamental flux and the 5th and the 7th harmonic currents causes a torque ripple component that is six times the field frequency [7]. This ripple component can be reduced by modifying the PWM modulation scheme to compensate for the effect of deadtime and current loop delay as proposed in [17] and [19]. The effect of three-phase power source imbalance in an inverter-fed machine is mainly caused by circuit offset. In a vector controller, this effect is particularly prominent due to the algorithm's high sensitivity to the three-phase stator current measurements [5], [6], [19]. Since all circuit signals are referenced to the stator frame, offset in these signals is equivalent to a periodic signal injected into the system in the field reference frame (i.e., the d-q frame). Consequently, a fundamental torque ripple component at the field frequency is produced.

Proposed Solution

Clearly, the magnitude and presence of the fundamental torque ripple and/or harmonic torque ripple components will vary from system to system. The torque ripple reduction scheme proposed here utilizes the structure of vector control. Assuming the presence of both components, the problem of torque ripple minimization in an induction motor under vector control can be subdivided into two specific problems [5], [6]. The first problem is to neutralize the fundamental torque ripple component. The second is to reduce any significant harmonic torque ripple components. However, in either case, the general functionality of the torque ripple compensator is the same.

The general functionality of the ripple compensator is based upon a parameter identification scheme. In other words, a parameterized spectral torque ripple model is proposed based on the contribution of dc bias currents and torque harmonics of the actual field frequency. The unknown parameters of this modeled torque ripple are determined by cross correlating digitally generated sine and cosine field functions with the measured torque ripple. Once the parameters are determined, the compensator generates a feedforward ripple cancellation term and performs bias current nullification.

It is important to note that it is possible to minimize the fundamental torque ripple component by manually tuning or removing any bias current generating offsets in the controller hardware. In addition, this effect can be further reduced under careful design of the motor, the current measuring circuit and transducers, and the controller and sampling hardware. It is also possible, in theory at least, to reject the torque ripple by closing the torque feedback loop via a proportional controller. This approach will result in a high gain loop which in turn may result in instability. The proposed scheme is able to automatically nullify the bias current generating circuit offsets (thereby reducing the fundamental torque ripple component) and to reduce the higher torque ripple harmonics via feedforward cancellation [5], [6]. Since the ripple reduction is achieved asymptotically, the stability of the system is preserved.

System Structure

Figure 4.1 on the next page shows the structure of a vector controller with the proposed torque ripple compensator. This system is very similar to Figure 3.7 of Chapter 3. The major hardware components of this system includes an induction motor, a PWM power amplifier, a digital computer, and a torque sensor. As indicated in the figure, the control software is mainly based on the standard VC algorithm. As discussed in Chapter 3,

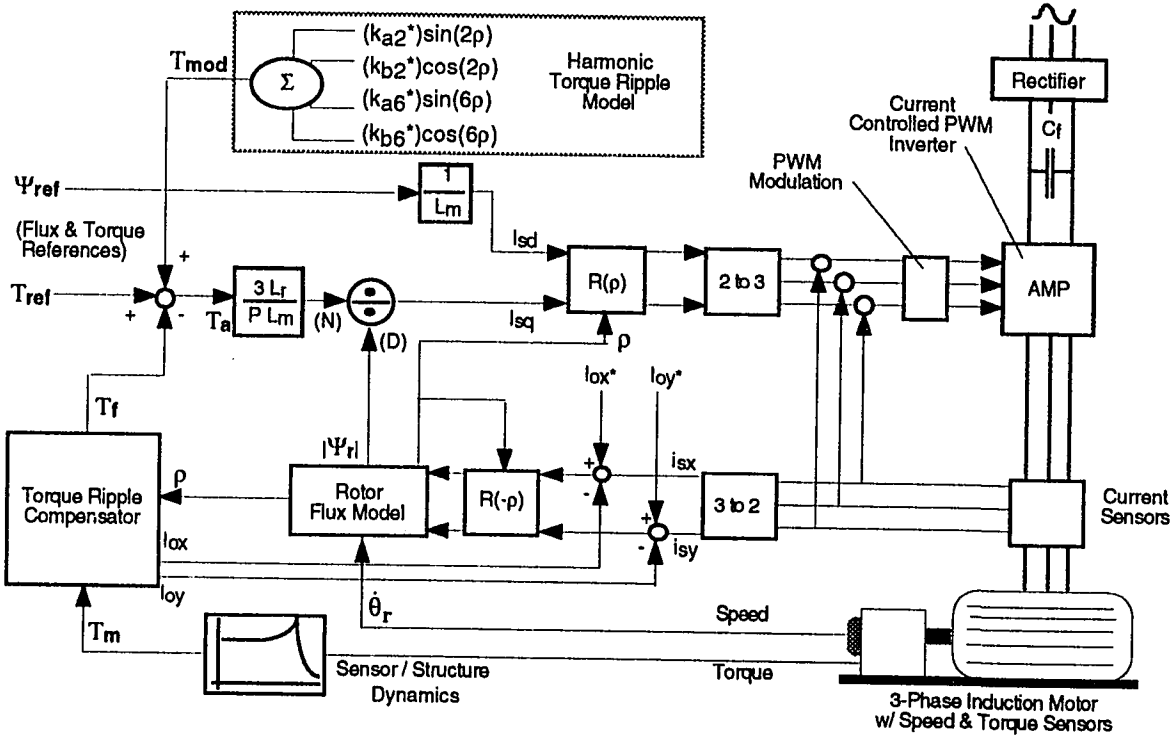

Figure 4.1. General System Structure using a Rotor-Flux Vector Controller in Conjunction with the Torque Ripple Compensator. (Source: R. Barro, P. Hsu, "Torque ripple compensation of vector controlled induction machines," in *IEEE Proc. Power Elect. Specialist Conf.*, 1997, pp. 1281-1287.)

this control system is configured to accept a torque reference input T_{ref} from an outer loop controller (e.g., speed, position using a PID controller) and generates the appropriate phase currents for the induction motor. As discussed in Chapter 3, vector control also allows the control of the flux level for field weakening operations. This control input, however, is not used in the proposed scheme.

Under the ideal situation, the VC algorithm guarantees that the actual torque produced by the induction motor tracks the reference torque exactly. In reality, due to the bandwidth of the power amplifier and model mismatch, the transfer function between the torque reference input to the actual motor torque T_m is better modeled by a lowpass filter. In the proposed scheme, motor torque is measured and fedback to the compensator. The transfer function of this feedback loop consists of the dynamics of the VC algorithm, PWM current loop, structure dynamics, and the torque transducer dynamics. It is important that the bandwidth of this transfer function be above the highest frequency torque ripple component to be reduced. Moreover, the phase shift for frequencies less than this bandwidth must be strictly less than 90 degrees. These properties are essential for the parameter identification scheme [1], [5].

Model of Fundamental Torque Ripple

As mentioned earlier, the fundamental torque ripple component in a vector controller is mainly due to the bias current as a result of circuit offset in the acquisition of the stator current. As shown in Figure 4.1 these offset terms are modeled in two-axis form by a pair of unknown constants (i.e., I_{ox} and I_{oy}) injected into the stator current data acquisition path. The effect of these offsets on the actual torque will be derived in the following paragraphs. The derivation is based on the rotor-flux oriented vector control model referenced to the stator frame of Figure 4.2. The mathematical workload is reduced and simplified by choosing this model. Note, however, that the effect of the offsets on the torque output of the induction machine is independent of the frame of reference used. The

rotor-flux model in the stator frame is adapted from [16] and can be found in [31].

The derivation begins by using the transformation matrix R(ρ) of (4-1) (restatement of equation (3-6)) and defining the reference stator currents in an alternate fashion. In other words, the reference stator currents can be written using the flux and torque references in conjunction with the rotor-flux model components Ψ_{rx} and Ψ_{ry}. Using (4-2) and (4-3), which define the orthogonal quadrature and direct stator currents accordingly, the reference stator currents can be written as in equation (4-4).

$$R(\rho)=\begin{bmatrix}\cos(\rho) & -\sin(\rho)\\ \sin(\rho) & \cos(\rho)\end{bmatrix} \tag{4-1}$$

$$I_{sd}=\frac{\Psi_{ref}}{L_m} \tag{4-2}$$

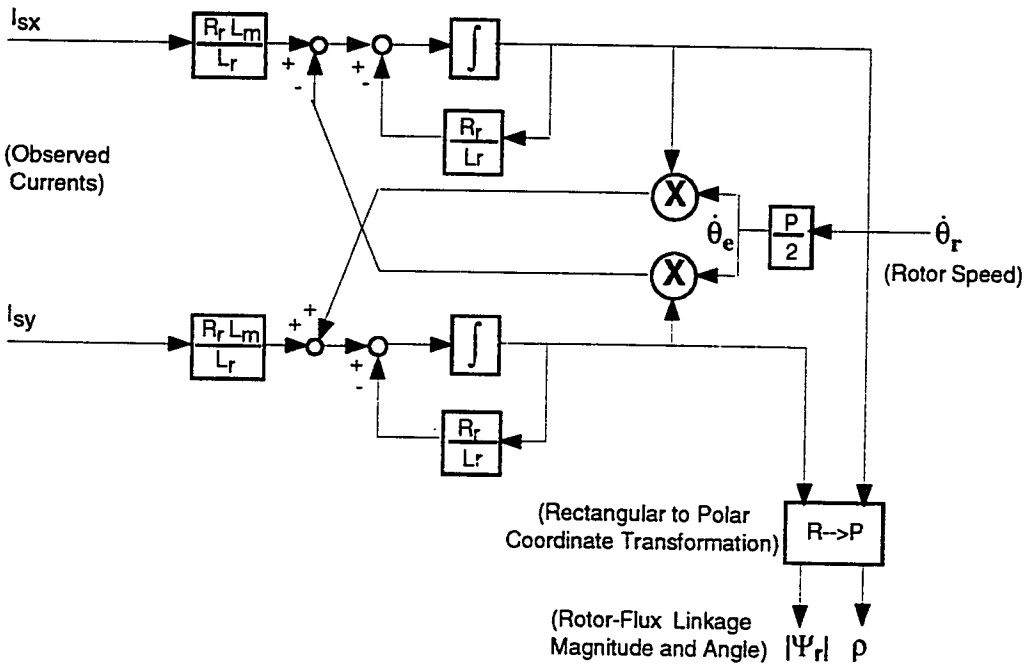

Figure 4.2. Rotor-Flux Model Referenced to the Stator Frame.

$$I_{sq} = \frac{3}{p}\frac{L_r}{L_m}\frac{1}{|\Psi_r|}T_{ref} \tag{4-3}$$

$$\bar{i}_s^s = \begin{bmatrix} i_{sx}^s \\ i_{sy}^s \end{bmatrix} = \begin{bmatrix} \cos(\rho) & -\sin(\rho) \\ \sin(\rho) & \cos(\rho) \end{bmatrix}\begin{bmatrix} I_{sd} \\ I_{sq} \end{bmatrix} \tag{4-4}$$

Since $\Psi_{rx} = |\Psi_r|\cos(\rho)$ and $\Psi_{ry} = |\Psi_r|\sin(\rho)$, then (4-4) can be re-written as in (4-5) and (4-6), where the term C_1 is defined as in (4-7). Note that all variables designated with the superscript 's' are referenced to the stator frame.

$$\bar{i}_s = \frac{1}{|\Psi_r|}\begin{bmatrix} \Psi_{rx}^s & -\Psi_{ry}^s \\ \Psi_{ry}^s & \Psi_{rx}^s \end{bmatrix}\begin{bmatrix} I_{sd} \\ I_{sq} \end{bmatrix} \tag{4-5}$$

$$\bar{i}_s = \frac{1}{|\Psi_r|L_m}\begin{bmatrix} \Psi_{ref} & -C_1 \\ C_1 & \Psi_{ref} \end{bmatrix}\begin{bmatrix} \Psi_{rx}^s \\ \Psi_{ry}^s \end{bmatrix} \tag{4-6}$$

$$C_1 \equiv \frac{3}{p}\frac{L_r}{|\Psi_r|}T_{ref} \tag{4-7}$$

Equation (4-6) is true provided that I_{ox} and I_{oy} are zero and in this case, the observed rotor flux Ψ_r determined by the flux model is identical to the actual motor rotor flux Ψ_a. It is also assumed that the reference and the actual stator currents are identical and that the power amplifier is ideal. Figure 4.3 on the next page describes these aforementioned statements using transfer function blocks of the vector controller. Clearly, if I_{ox} and I_{oy} are not zero than the inputs to the motor and the flux model are different. As a direct result, the actual flux production in the motor will differ from the flux model by a constant factor Ψ_c (4-8).

$$\bar{\Psi}_a^s = \bar{\Psi}_r^s - \bar{\Psi}_c^s \tag{4-8}$$

Alternatively, equation (4-8) can be rewritten as in (4-9) where $H_1(s)$ is the transfer function relating the stator current and rotor flux described as the motor and flux models respectively.

$$\bar{\Psi}_r(s) = H_1(s)\bar{i}_s(s) + H_1(s)\bar{I}_o(s) \tag{4-9}$$

Since the offset vector $I_o(s)$ is a constant, from (4-9) it is clear that $H_1(s)I_o(s)$ is the DC steady state output due to $I_o(s)$. Using the rotor-flux model referenced in the stator frame and including the offsetting bias terms, the derivative of the rotor flux can be written as in (4-10).

$$\begin{bmatrix} \dot{\Psi}_{rx}^s \\ \dot{\Psi}_{ry}^s \end{bmatrix} = \begin{bmatrix} -\frac{R_r}{L_r} & -\dot{\theta}_r \frac{p}{2} \\ \dot{\theta}_r \frac{p}{2} & -\frac{R_r}{L_r} \end{bmatrix} \begin{bmatrix} \Psi_{rx}^s \\ \Psi_{ry}^s \end{bmatrix} + \frac{L_m R_r}{L_r} \left(\begin{bmatrix} i_{rx}^s \\ i_{ry}^s \end{bmatrix} + \begin{bmatrix} I_{ox}^s \\ I_{oy}^s \end{bmatrix} \right) \tag{4-10}$$

Note that the DC output due to I_o is the solution of (4-11).

$$\begin{bmatrix} 0 \\ 0 \end{bmatrix} = \begin{bmatrix} -\frac{R_r}{L_r} & -\dot{\theta}_r \frac{p}{2} \\ \dot{\theta}_r \frac{p}{2} & -\frac{R_r}{L_r} \end{bmatrix} \begin{bmatrix} \Psi_{rx}^s \\ \Psi_{ry}^s \end{bmatrix} + L_m \frac{R_r}{L_r} \begin{bmatrix} I_{ox}^s \\ I_{oy}^s \end{bmatrix} \tag{4-11}$$

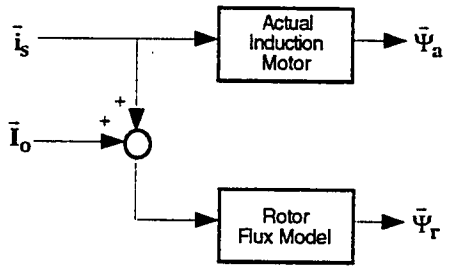

Figure 4.3. Model of an Induction Motor Running in Conjunction with a Rotor-Flux Model Subjected to Stator DC Bias Currents.

If the rotor is locked than $d\theta_r/dt$ is zero and thus, the flux contribution of I_o is

$$\bar{\Psi}_c^s = L_m \bar{I}_o \tag{4-12}$$

The electromagnetic torque production in an induction machine is shown in (4-13).

$$T_e = \frac{p}{3}\frac{L_m}{L_r}\bar{\Psi}_a^s \times \bar{i}_s^s \tag{4-13}$$

If (4-8) is substituted into (4-13), equation (4-14) is determined. Equation (4-14) consists of two terms as described by (4-15). The first term is a classical relation describing the constant electromagnetic torque production of an induction motor (see Chapter 3). The second term can be expanded upon the substitution of equation (4-6) and (4-12). As a result of these substitutions, a general relation describing the magnitude and phase of the torque ripple as a function of the circuit offsets, flux and torque references, and the components of the magnitude of the rotor flux is found in (4-16). Note that C_2 is defined as in equation (4-17).

$$T_e = \frac{p}{3}\frac{L_m}{L_r}\bar{\Psi}_r^s \times \bar{i}_s^s - \frac{p}{3}\frac{L_m}{L_r}\bar{\Psi}_c^s \times \bar{i}_s^s \tag{4-14}$$

$$= T_{consant} - T_{ripple} \tag{4-15}$$

$$T_{ripple} = C_2\begin{bmatrix} I_{ox} & I_{oy} \end{bmatrix}\begin{bmatrix} C_1\Psi_{sx}^s + \Psi_{sy}^s\Psi_{ref} \\ -\Psi_{sx}^s\Psi_{ref} + C_1\Psi_{sy}^s \end{bmatrix} \tag{4-16}$$

$$C_2 \equiv \frac{p}{3}\frac{L_m}{Lr}\frac{1}{|\Psi_r|} \tag{4-17}$$

Alternatively, (4-16) can be written in terms of the rotor-flux angle ρ and the field phase (i.e., $\cos(\rho)$ and $\sin(\rho)$) as in (4-18).

$$T_{ripple} = C_2 |\Psi_r| \begin{bmatrix} I_{ox} & I_{oy} \end{bmatrix} \begin{bmatrix} C_1 \cos(\rho) + \Psi_{ref} \sin(\rho) \\ -\Psi_{ref} \cos(\rho) + C_1 \sin(\rho) \end{bmatrix} \quad (4\text{-}18)$$

Also note that in a typical operation C_1 is much greater than Ψ_{ref} (i.e., $C_1 >> \Psi_{ref}$). This means that in the typical operation the contribution of I_{ox} to the torque ripple is mostly in phase with $\cos(\rho)$ and that of I_{oy} is to mostly in phase with $\sin(\rho)$.

Harmonic Torque Ripple Model

A discussion was presented on the causes of torque ripple. Clearly, an exact mathematical expression of all the aforementioned causes (excluding circuit offset) is complex and difficult to obtain. In this case, the causes of the harmonic torque ripple components are combined and modeled as a fictitious torque command input to the vector controller. This fictitious torque term T_{mod} consists of a linear combination of sinusoid functions whose frequencies are multiples of the field frequency. The structure of this disturbance term is shown in Figure 4.1 on page 59 and is defined in (4-19).

$$T_{mod}(\rho) = \sum_{n=2,6} \left(\tilde{k}_{an} \cos(n\rho) + \tilde{k}_{bn} \sin(n\rho) \right) \quad (4\text{-}19)$$

Parameters k_{an}^* and k_{bn}^* (i.e., where n = 1, 2 and 6) are defined as the unknown parameters which determine the magnitude and phase of the torque ripple components. Note that the parameters k_{a1}^* and k_{b1}^* are really the unknown bias current terms where $k_{a1}^* = I_{ox}^*$ and $k_{b1}^* = I_{oy}^*$ and are not grouped in the model for T_{mod}. In the experimental setup, the energy of the torque ripple concentrated in the first, second, and sixth harmonics and therefore, only these three ripple components are considered in the following discussion. The proposed approach, however, can be extended to the case where more spectral lines exist.

Ripple Compensation Model

Figure 4.4 shows the structure of the ripple compensator. The compensator generates two types of correction terms: (1) bias current nullification terms, (2) and the ripple feedforward cancellation term T_f. Note that the composition of T_f is very similar to that of T_{mod}. In fact, if the parameters of T_f (i.e., parameter estimates k_{an} and k_{bn}) match those in T_{mod}, the effect of T_{mod} is completely canceled by T_f. The bias current nullification terms operate in a similar fashion. In the actual implementation, in order to utilize the full resolution of the ADC, the torque ripple T_r is extracted from the torque measurement T_m by passing it through a analog highpass filter. In the experimental setup an application specific

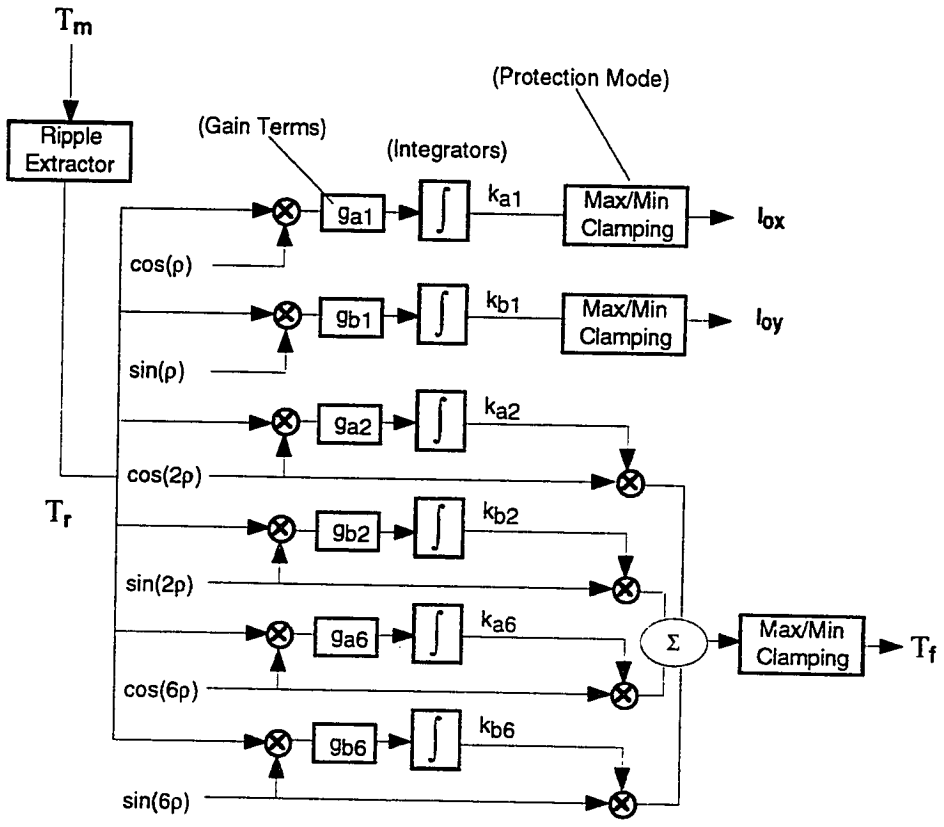

Figure 4.4. Proposed and Experimentally Implemented Torque Ripple Compensator. (Source: R. Barro, P. Hsu, "Torque ripple compensation of vector controlled induction machines," in *IEEE Proc. Power Elect. Specialist Conf.*, 1997, pp. 1281-1287.)

circuit was constructed for this task. A discussion on this circuit can be found in Appendix B.

Parameter Identification

In the parameter tuning process, the desired torque is set to a constant value T_{ref}, and the parameter estimates are updated according to update laws (4-20) and (4-21). The values for ga_n and gb_n in these equations are parameter update gains and are to be adjusted experimentally to achieve a reasonable convergence rate and to avoid undesirable transient behavior.

$$k_{an} = \int ga_n \cos(n\rho) T_r dt \tag{4-20}$$

$$k_{bn} = \int gb_n \sin(n\rho) T_r dt \tag{4-21}$$

These update laws cross correlate the measured torque ripple and the basis functions that the parameters are associated with. In other words, the bias current nullification terms k_{a1} and k_{b1} (i.e., I_{ox} and I_{oy}) are generated from the cross correlation of, respectively, cos(ρ) and sin(ρ) with the torque ripple. This is because, as explained earlier, the contribution of I_{ox} to the torque ripple is mostly in phase with cos(ρ) and that of I_{oy} is mostly in phase with sin(ρ).

In order to guarantee that the parameter estimates converge to their true values, it is imperative that the phase shift of the torque feedback loop be less than 90°. In other words, the actual torque measurement from torque feedback loop can be represented by (4-22), where T_r is the extracted torque ripple and T_a is the augmented torque given by (4-23). $H_2(s)$ represents the transfer function of the torque feedback loop. Therefore, for the frequencies of interest (e.g., 1st, 2nd, and 6th harmonics), $H_2(s)$ must not provide more than 90° phase shift. Note that the phase shift requirement was experimentally verified and discussed in [5]. Although (4-23) is defined for the 2nd and 6th harmonics, as mentioned

earlier, it can be extended to include more spectral lines. The parameter errors between the actual and estimated values are defined in (4-24) and (4-25).

$$T_r(s) = H_2(s)T_a(s) \tag{4-22}$$

$$T_a(\rho) = T_{ref}(\rho) + \sum_{n=2,6}\left(\tilde{k}_{an}\sin(n\rho) + \tilde{k}_{bn}\cos(n\rho)\right) \tag{4-23}$$

$$\tilde{k}_{an} \equiv k^*_{an} - k_{an} \tag{4-24}$$

$$\tilde{k}_{bn} \equiv k^*_{bn} - k_{bn} \tag{4-25}$$

The following analysis will show that the magnitudes of the parameter errors converge to zero thereby proving parameter convergence. In this analysis one term of one harmonic (i.e., 2nd harmonic) is considered. In equation (4-26) the magnitude of the parameter error associated with the "a2" term is defined as E_{a2}.

$$E_{a2} = \frac{1}{2}\left|\tilde{k}_{a2}\right|^2 \tag{4-26}$$

Using update law (4-19) it is possible to show that E_{a2} converges to zero. To prove the convergence of the parameter k_{a2}, we consider the magnitude of the parameter error E_{a2} as defined in (4-26). Note that the derivative of the actual parameter k_{a2}* is zero since it is assumed to be constant. In addition, the derivative of the parameter estimate k_{a2} (4-27) is found using the derivative of (4-19) where the gain term ga_2 has been set to one. The derivative of E_{a2} is defined in (4-28).

$$\dot{k}_{a2} = T_r\cos(2\rho) \tag{4-27}$$

$$\begin{aligned}\dot{E}_{a2} &= \left(\tilde{k}_{a2}\right)\left(\dot{\tilde{k}}_{a2}\right) \\ &= \left(\tilde{k}_{a2}\right)\left(\dot{k}^{*}_{a2} - \dot{k}_{a2}\right) \\ &= -\left(\tilde{k}_{a2}\right)\left(\dot{k}_{a2}\right) \\ &= -\left(\tilde{k}_{a2}\right)\left(T_r \cos(2\rho)\right)\end{aligned} \tag{4-28}$$

Also note that as a direct result of integrating both sides of (4-28), equation (4-29) is determined.

$$\begin{aligned}E_{a2}(t) &= E_{a2}(0) + \int_0^t -\tilde{k}_{a2}\left(T_m \cos(2\rho)\right)dt \\ &= E_{a2}(0) - G_2 \int_0^t \tilde{k}^2_{a2}\left(\cos(2\rho)\right)\left(\cos(2\rho + \phi_2)\right)dt\end{aligned} \tag{4-29}$$

The variable G_2 and ϕ_2 in (4-29) is the magnitude and phase response of $H_2(s)$ at the 2nd harmonic frequency. Equation (4-29) is based on the orthogonality between sinusoidal functions of different frequencies and the assumption that the parameter k_{a2} adapts slowly. Note that as mentioned earlier, the transfer function $H_2(s)$ is assumed to have a phase shift less than 90 degrees at the frequency of interest. This assumption implies that the integral term in (4-29) is positive for a sufficiently long integration period. Since $E_{a2}(t)$ is bounded below by zero, the integral term in (4-29) must be bounded above by $E_{a2}(0)$. Furthermore, since the product of the cosine term in the integral term has a constant peak magnitude and since the integral term is bounded even for an arbitrarily long integration period, the parameter estimate error must converge to zero.

In summary, the above analysis shows that, if parameter estimates k_{an} and k_{bn} are updated according to equations (4-19) and (4-20), they will eventually converge to the true unknown parameters k_{an}* and k_{bn}*. This analysis is based on two assumptions. First of all, the phase shift due to the transfer function $H_2(s)$ at the frequencies of interest is less then 90 degrees and secondly, the process undergoes slow adaptation. In a more rigorous

analysis and with additional filtering of the measured signals, both of these assumptions can be relaxed [1].

Ripple Compensator Permutations

There are several important issues which need to be resolved in the use of this compensator. The first issue is the fact that the implementation of this ripple minimization algorithm requires the use of a torque sensor. Fine quality torque sensors with reliable strain gauges and low hysteresis are quite expensive. A 1000 lb-in high quality sensor may cost upwards around $4000.00. In low cost applications this may or may not be tolerable. Furthermore, many existing control systems are not designed for using a torque sensor as a means for closed loop feedback [16]. With this point made, the second major issue is the implementation of this algorithm without using a torque sensor in the compensator. In other words, can other signals be used in place of the torque signal? The answer is yes. It is possible to use the position ripple from a closed loop position controller in place of the measured torque ripple from the torque sensor. Critically, though, the position ripple must adhere to the rules governing the 90 degree correlation interval and (if using a shaft encoder) be highpass filtered in software. Finally, the last issue pertains to other ripple compensator permutations. In other words, in some systems using a torque sensor and locking the rotor may not be feasible. In this case, it clearly would be useful if this compensator can work under a speed control loop or open loop vector control scheme where a low steady state speed is achieved and torque is fedback. Again, it is possible to perform such a compensation scheme provided that the rules of the compensation algorithm are adhered to. In Chapter 5, several experiments are listed which provide proof of success of these permutated compensation algorithms.

Software Algorithm

The implementation of the torque ripple compensator is performed through the use of a C function call in the main loop of the VC algorithm. In its simplest form an example

of this function is shown in Figure 4.6. Note, the function is programmed to be initiated upon the setting of flags by the user from a host computer. All variables not defined inside the function are global. In addition, one feature not discussed in the previous sections is a protection mode. In the program saturation blocks should be placed at the outputs of the integrators of the fundamental ripple compensator. A protection block should also be placed at the feedforward torque input of the vector controller (i.e., T_f). This protection block will clip off the high amplitude feedforward torque peaks. These protection modes are a must since they protect the vector controller in the event of parameter divergence. A more complicated version would implement an auto shutoff mode upon complete parameter identification or shutoff if the vector controller becomes unstable. In addition, a more complete compensator will perform the highpass filtering of the torque measurement, identify any offsets at the output of the vector controller, and entail the use of an outer loop speed and/or position controller for parameter identification.

In Chapter 5 experiments such as the aforementioned, and system/model identification/verification are presented in detail.

```
Ripple_Minimize()
{
    float Scale, max_offset_x, max_offset_y;
    Scale = 100;
    max_offset_x = 2.00;
    max_offset_y = 2.00
    min_offset_x = -2.00;
    min_offset_y = -2.00
    if (goffset_added_flag == 0)
    {
        goffset_x_added_in = 0.0;
        goffset_y_added_in = 0.0;
        lox = 0.0;
        loy = 0.0;
    }
    if (offset_added_flag == 1 )
    {
        a1= cos(rho);
        b1 = sin(rho);
        a2= cos(2*rho);
        b2 = sin(2*rho);
        a6= cos(6*rho);
        b6 = sin(6*rho);
        offset_x_added_in = offset_x_added_in + deltat * ga1 * (a1 * Actual_Torque_in_AC);
        lox = offset_x_added_in;
        if (goffset_x_added_in > max_offset_x) glox = max_offset_x;
        if (goffset_x_added_in < min_offset_x) glox = min_offset_x;
        offset_x_added_in = offset_x_added_in + deltat * gb1 * (b1 * Actual_Torque_in_AC);
        loy = offset_y_added_in;
        if (goffset_y_added_in > max_offset_y) gloy = max_offset_y;
        if (goffset_y_added_in < min_offset_y) gloy = min_offset_y;
        ka2 = ka2 + deltat * ga2 * (a2 * Actual_Torque_in_AC);
        kb2 = kb2 + deltat * gb2 * (b2 * Actual_Torque_in_AC);
        ka6 = ka6 + deltat * ga6 * (a6 * Actual_Torque_in_AC);
        kb6 = kb6 + deltat * gb6 * (b6 * Actual_Torque_in_AC);
        T_feed = ka2*a2 + kb2*b2 +ka6*a6 + kb6*b6)/Scale;
    }
}
```

Figure 4.5. Sample C Program Function Implementation of the Torque Ripple Compensator.

CHAPTER 5

Conclusive Experimental Results

The mathematical investigation of torque ripple production in vector controlled induction machines is clearly complex as discussed in Chapter 4. On the other hand, experimentally this complex problem may be broken down into a series of tests which can yield insight into the core of the problem. The purpose of this chapter is to present empirical data which characterizes the torque ripple model and reduction scheme as presented in Chapter 4. The heart of this chapter is the evaluative analysis of this empirical data. Most of the data discussed and presented in this chapter is located at the end of the chapter (beginning on page 91). Moreover, unless otherwise noted, most of the results presented in this chapter are based on the zero speed condition and were generated using a rotor-flux oriented direct vector controller.

Experimental Setup

In order to investigate the torque ripple source and the reduction scheme (and the scheme permutations) proposed in Chapter 4, a specialized test-bed was constructed. A diagram of this test-bed is shown in Figure 5.1 and a photograph is shown in Figure 5.2 on page 75. As shown, the test-bed includes an industrial off-shelf squirrel cage induction motor, a torque sensing transducer, a speed reducing gearbox, and a loading dc motor. A zero backlash flexible disc coupling was used to create a rigid union between the right side of the torque sensor and the motor shaft. On the left side of the torque sensor a pulley is mounted on the shaft and a locking pin may be inserted on this side for locked rotor testing. Furthermore, this pulley can also be used for weight lifting and suspension through a cable pulley mechanism. A speed reducing gearbox and a dc motor are also integrated (via shaft coupling) into the machine for heavy torque loading on the induction motor. The dc motor is configured to behave as a generator so to provide torque loading [8]. A number of configurations are possible in this versatile test bed (e.g., high torque and low or zero

speed or low torque and high speed applications). The specifications of the motor, torque sensor, and the flexible disc coupling are described respectively by Tables B.1, B.2, and B.3 in Appendix B.

In addition to the aforementioned testing machine, the experimental setup contains other key elements for the impulsion of the induction motor. First of all, the induction motor under test is driven by a PWM voltage source inverter (power amplifier). The power source of this inverter is an adjustable dc bus (0-390 Volts). The power amplifier permits the adjustment of the current magnitude and frequency (via nonsinusoidal PWM voltage) through the use of current feedback (i.e., comparison of actual and reference currents) for accurate current regulation [24]. The reference currents required for current regulation are generated by the vector controller. The vector controller used is direct and is rotor-flux oriented referenced to the rotor-flux frame (as discussed in Chapter 3). The VC algorithm (programmed in C) is enabled through the use of a TMS320C30 DSP controller. The rotor-flux model implemented uses current sensing from two of the three phase currents

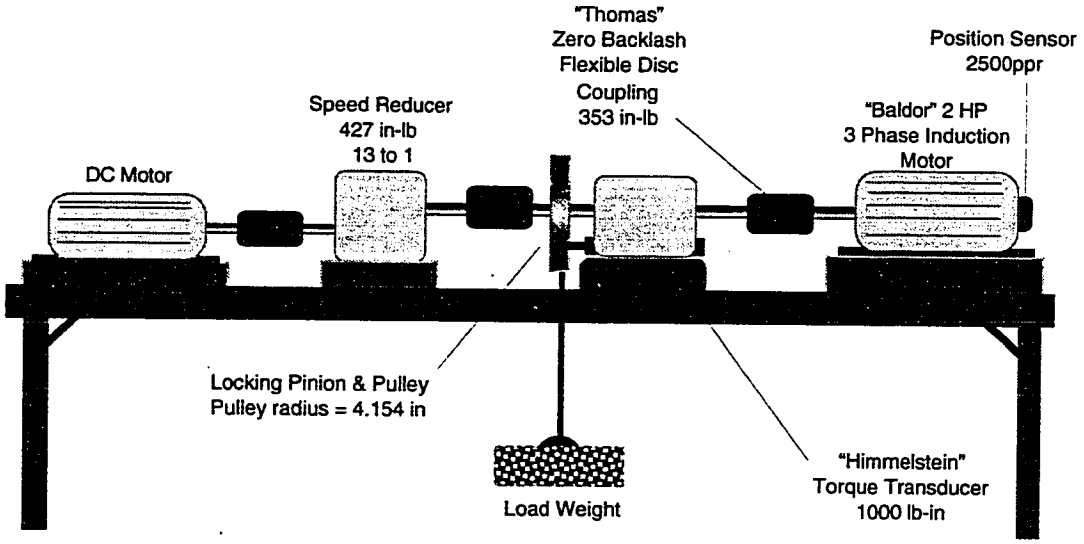

Figure 5.1. Diagram of the Experimental Testing Machine.

and velocity feedback through a digital encoder. Finally, to ensure the operating temperature was at a stable value, cooling fans were placed around the motor. The temperature of the motor was monitored using a thermocouple and the operating temperature of motor was usually kept between 27° C and 50° C. The key torque ripple minimization experiments performed are presented in the following sections.

Experimental Set No. 1 - System Identification

In Chapter 4 a discussion was presented in reference to the dynamics of the torque feedback loop. The purpose of this experiment was to identify the transfer function of this torque feedback loop. A model of this loop is shown in Figure 5.3 (next page) where $H_2(s)$ is defined as the transfer function defining the PWM current loop, vector controller, motor, torque sensor and structure dynamics under locked conditions. Ideally, the measured torque of this loop is identical to the reference torque and thus $H_2(s)$ is equal to one. In reality, $H_2(s)$ as in equation (5-1) is modeled in this system as a second order lowpass filter exhibiting a resonant mode.

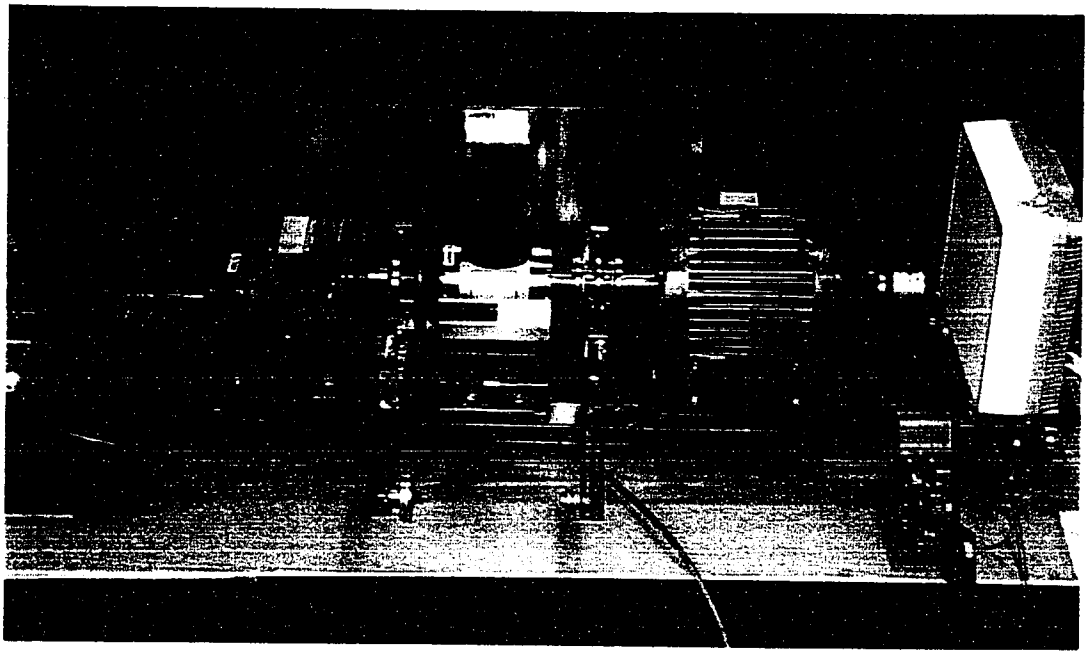

Figure 5.2. Actual Experimental Induction Motor Torque Loading and Sensing Machine.

$$H_2(s) = \frac{35,6292.92}{s^2 + 59.69s + 35,6292.92} \qquad (5\text{-}1)$$

This is based on the experimental data as shown in Figures 5.6, 5.7, and 5.8. Figures 5.6 and 5.7 were generated by injecting a range of equal magnitude torque sinusoids at increasing frequencies into the vector controller. The output torque magnitude and phase values (frequency response) were recorded at each of those frequencies. Clearly, the frequency response data demonstrates a resonant mode between 95-100 Hz and 90° phase shift in this region. In addition, to confirm this resonant mode, step response data was taken as well. The step response data of Figure 5.8 demonstrates that this model is underdamped, overshoots the desired torque and exhibits a resonant mode between 95-100 Hz. The bandwidth of this system is found to be approximately 100 Hz and the data presented hereafter has been low pass filtered in MATLAB at this frequency to remove any extraneous noise components. The reason for low-pass filtering the data at this frequency is presented next.

Experimental Set No. 2 - Noise Analysis

The torque sensor used in this project exhibits a high level of sensitivity to electrical noise in the experimental setup. The reason for this could be attributed to noise generation by the power amplifier and the autotransformer used in controlling the dc bus voltage. Figure 5.9 demonstrates the noise present on the torque signal with the vector controller enabled and the torque sensor uncoupled from the motor. Figure 5.10 demonstrates the wide range of frequencies which are present on the signal. Note that the spike at 9.5 Hz is the field frequency of the motor during the experiment. If the system is assumed to have a

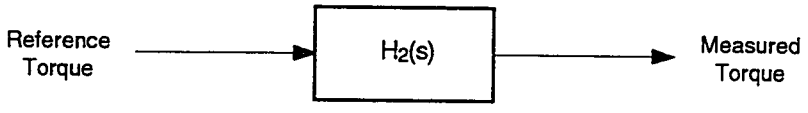

Figure 5.3. Torque Feedback Loop Transfer Function.

bandwidth of at least 100 Hz from the above analysis, then the torque signal can be filtered at this frequency for signal clarity. An 8th-order Butterworth lowpass digital filter in MATLAB was used for the torque signal shown in Figure 5.11. Clearly, the clarity of the signal and the bandwidth of this system warrants the use of this filter for the presentation of the torque data.

Experimental Set No. 3 -Untuned Vector Control

In order to clearly exhibit the undesirable effects bias current offsets have on vector control, a gamut of data from separate experiments was collected (i.e., Figures 5.12 through 5.22). The operating conditions for this set of data are as follows: T_{ref} = 4 N-m, Ψ_{ref} = 0.2 Wb, B_{dc} = 250 V, ω_r = 0 r/min, Temp. = 27° - 40° C, F_s = 5000 Hz, R_r = 0.82 Ω, L_r = 0.11079 H, and L_m = 0.1080 H. This collection of data is based on the locked rotor condition. Figure 5.12 demonstrates that the measured stator currents i_{sx} and i_{sy} are not centered around zero due to bias current offsets. This figure also demonstrates the nonsinusoidal nature of the signals. Figures 5.13 and 5.14 show that the direct and quadrature currents I_{sd} and I_{sq} respectively, are not constant in the rotor-flux frame. As a result of the bias current offsets, I_{sd} and I_{sq} are time-varying. Similarly, the observed rotor flux magnitude $|\Psi_r|$ (shown in Figure 5.15) is also time-varying and not constant. Although it is very subtle, Figures 5.16 and 5.17 respectively show that the slip angle α and rotor flux angle ρ are nonlinear. As a result of the nonlinear rotor-flux angle, the field functions cos(ρ) and sin(ρ) are shown to be nonsinusoidal in Figures 5.18 and 5.19. Figure 5.20 is the end product of bias current offsets. The torque measurement demonstrates the vile magnitude of torque ripple. Figure 5.21 is an FFT spectrum plot of the locked rotor torque measurement of Figure 5.20. Figures 5.20 and 5.21 clearly demonstrate the periodicity of the torque ripple and that higher order harmonics of the fundamental component are present. Specifically, the ripple energy is concentrated on the first (9.5 Hz), second, and sixth harmonics of the field frequency. This observation and

the above analysis clearly supports that the source of the ripple can be modeled by a linear combination of a set of sinusoid functions whose frequencies are multiples of the fundamental field frequency. Finally, Figure 5.22 demonstrates the phase relation of some of the aforementioned control parameters with respect to one another.

Experimental Set No. 4 -Torque Ripple Characterization and Model Validation

In order to characterize the influence of torque and flux on the fundamental torque ripple a sequence of tests were carried out. Table 5.2 on page 115 contains data where the motor is locked and torque is applied in the clockwise direction. Table 5.3 contains data where the motor is locked and torque is applied in the counterclockwise direction. These tables demonstrate that at low flux levels the torque ripple magnitude is much larger than at higher flux levels (i.e., C_1 in equation (4-18) is larger and dominates). Moreover, the phase shift of the torque ripple in relation to cos(ρ) is much more significant at lower flux levels.

Prior to the derivation of equation (4-18), it was experimentally verified that the magnitude and phase of the torque ripple are functions of the magnitude of the bias current offsets. This is shown in Figures 5.23 and 5.24. In Figure 5.23, the experimental data was generated with one of the bias terms (i.e., I_{oy}) eliminated. Note that peak to peak torque $T_{p\text{-}p}$ is much smaller in comparison to $T_{p\text{-}p}$ of Figure 5.22. Also note that the torque ripple is nearly in phase with cos(ρ). In Figure 5.24, the experimental data was generated with I_{ox} eliminated. In this case $T_{p\text{-}p}$ has changed again and the torque ripple is about 90° out of phase with cos(ρ).

In order to verify that the torque ripple model of equation (4-18) is valid, the sampled data of ρ from Figure 5.22 was used. The conditions used in (4-18) from the experiment of Figure 5.22 are as follows: P = 4, Ψ_{ref} = 0.2 Wb, T_{ref} = 4 N-m, L_r = 0.11079, L_m = 0.1080, I_{ox} = 0.422 A and I_{ox} = -0.646 A. In Figure 5.25 the measured torque ripple of Figure 5.22 is shown without the steady state torque. The modeled curve

of Figure 5.26 shows clearly how close the magnitude and phase of the model match the actual torque ripple of Figure 5.25. A table of values (i.e., Table 5.4) was computed using (4-18) as well. The modeled data of Table 5.4 closely corresponds to the actual measured data of Table 5.2.

Experimental Set No. 5 -Fundamental Torque Ripple Reduction

In this set of experiments, only the fundamental torque ripple component is compensated. The operating conditions for this set of data are as follows: $T_{ref} = 4$ N-m, $\Psi_{ref} = 0.2$ Wb, $B_{dc} = 250$ V, $\omega_r = 0$ r/min, Temp. = 27° - 40° C, $F_s = 5000$ Hz, $R_r = 0.82\ \Omega$, $L_r = 0.11079$ H, and $L_m = 0.1080$ H. Again, this collection of data is based on the locked rotor condition. Upon parameter convergence and the nullification of the stator bias currents, various signals of the vector controller have clearly been affected. First of all, Figure 5.27 shows noticeably that the bias currents offsets have been nullified and that i_{sx} and i_{sy} are centered about zero. Figure 5.28 shows that the observed rotor-flux magnitude is constant. More importantly, Figure 5.29 shows the resulting torque measurement and Figure 5.30 shows the corresponding spectrum. As shown, the fundamental component was effectively compensated by the adding the corresponding offset terms of $I_{ox} = -0.422$ A and $I_{ox} = 0.646$ A to the two-axis (x, y) current sensing inputs. These two-axis current offsets correspond to offsets at the real current sensing inputs (e.g., phase A, B, and C) of $I_{oa} = -0.281$ A and $I_{ob} = -0.232$ A. The stator current at this torque level is approximately 10.2 Amps (peak). The amount of added offset is only 2.8% and 2.2% of the peak current while the peak torque ripple is about 33% of the nominal value. Clearly, the controller exhibits high sensitivity to the current measurement offset.

Figure 5.31 demonstrates collectively some of the main signals of the tuned vector controller. In particular, the figure demonstrates that I_{sd} and I_{sq} are constant as desired, the rotor flux angle is linear, and cos(ρ) is sinusoidal. Figure 5.32 shows the real time torque ripple reduction and the convergence of the parameter I_{ox} in approximately two seconds.

Figure 5.33 demonstrates the Lissajous patterns generated from i_{sx} and i_{sy} before and after fundamental ripple reduction. Note that the rate of parameter convergence was quite consistent during the generation of Figures 5.26 through 5.32. The rate of convergence will vary upon the field frequency and the choice of the gains in the update laws. The rate of convergence will also vary upon the proper selection of the field functions. Although Figures 5.23 and 5.24 were used in the characterization of the torque ripple, they also serve in demonstrating equation (4-18) is correctly defined. In other words, for rapid parameter convergence of I_{ox} and I_{oy}, cos(ρ) and sin(ρ) are used respectively in (4-20) and (4-21) since the contribution of I_{ox} to the torque ripple is mostly in phase with cos(ρ) and that of I_{oy} is mostly in phase with sin(ρ). This can be verified under close analysis of the torque ripple and field functions in Figures 5.23 and 5.24.

Experimental Set No. 6 -Harmonic Torque Ripple Reduction

In this set of experiments all three ripple components (fundamental, 2nd, and 6th) are compensated. The locked rotor operating conditions for this set of data are as follows: T_{ref} = 4 N-m, Ψ_{ref} = 0.2 Wb, B_{dc} = 250 V, ω_r = 0 r/min, Temp. = 27° - 40° C, F_s = 5000 Hz, R_r = 0.82 Ω, L_r = 0.11079 H, and L_m = 0.1080 H. Figure 5.34 shows the final torque measurement upon complete parameter adaptation and the respected spectrum is shown in Figure 5.35. Figure 5.36 shows a typical feedforward cancellation term used to reduce the harmonic torque ripple. The identified parameters of this feedforward cancellation term are: k_{a2} = -0.0088 N-m, k_{b2} = -0.0122 N-m, k_{a6} = 0.0028 N-m and k_{b6} = 0.0301 N-m. Figure 5.37 is the frequency spectrum of the feedforward cancellation term. Clearly, the 2nd and 6th harmonics have been identified and the resulting spectrum of Figure 5.35 is free of harmonics.

Experimental Set No. 7 -Torque Ripple Reduction using Other Control Configurations

This set of data confirms the possibility of using the proposed compensator in conjunction with other control configurations. In particular, an investigation into using the

compensator under open loop and closed loop speed control was performed. Note, however, due to the difficulty in resolving the harmonic torque ripple in these control configurations, only the fundamental torque ripple term was reduced. The three configurations are as follows:

1. Torque ripple reduction using a torque sensor and open loop speed control.
2. Torque ripple reduction using a torque sensor and closing the speed control loop around the vector controller.
3. Torque ripple reduction using a position sensor at zero speed and closing the position control loop around the vector controller.

Open Loop Vector Control

In this configuration, a low torque reference was given to the vector controller and the speed reducer was used to load the motor. The motor was allowed to reach a steady state speed prior to the use of the compensator. The operating conditions for this set of data are as follows: T_{ref} = 2.5 N-m, Ψ_{ref} = 0.2 Wb, B_{dc} = 250 V, ω_r = 49 r/min, Temp. = 27° - 40° C, F_s = 5000 Hz, R_r = 0.82 Ω, L_r = 0.11079 H, and L_m = 0.1080 H. Figure 5.38 demonstrates the torque ripple under these conditions and Figure 5.39 is the resulting frequency spectrum. Figure 5.39 notes the difficulty in resolving any harmonic torque ripple. The speed reducer used is a geared assembly and it introduces a high level of mechanical noise into the torque signal. After fundamental torque ripple reduction, the compensator determined that I_{ox} = -0.422 A and I_{oy} = 0.646 A. The torque measurement after compensation is shown in Figure 5.40 and the resulting spectrum is shown in Figure 5.41.

Speed Control Loop

It is possible to dynamically tune the offsets I_{ox} and I_{oy} using a closed speed control loop around the VC algorithm. Note in this configuration a load is attached to the rotor and the motor is set to run at a moderately low speed (e.g., 50 r/min). This experiment is very

similar to the open loop control case presented above. The operating conditions for this set of data are as follows: $\Psi_{ref} = 0.2$ Wb, $B_{dc} = 250$ V, $\omega_r = 50$ r/min, $\omega_{ref} = 50$ r/min, Temp. = 27° - 40° C, $F_s = 5000$ Hz, $R_r = 0.82\ \Omega$, $L_r = 0.11079$ H, and $L_m = 0.1080$ H. Figures 5.42 and 5.43 demonstrate the torque ripple and the spectrum prior to compensation. Figures 5.44 and 5.45 demonstrate the torque ripple and the spectrum after torque ripple reduction. After rapid fundamental torque ripple reduction, the compensator determined that $I_{ox} = -0.422$ A and $I_{oy} = 0.646$ A.

Position Control Loop

It is also possible determine I_{ox} and I_{oy} utilizing a position sensor and closing the position control loop around the VC algorithm. A weight is lifted and suspended via a cable pulley mechanism. In this setup, the load to the motor is constant and hence the rotor position should not vibrate (even though a slight position error may exist). Since the mechanical damping is low, any amount of torque ripple results in an oscillation of the suspended weight. The idea in this series of tests is to determine whether or not the identification of the torque ripple model parameters can be done by using the measured position ripple (i.e., position ripple which is highpass filtered) instead of the measured torque ripple. The critical issue here is the effective closed loop bandwidth of the position controller. If the bandwidth of the position control loop is much higher than the field frequency, the torque ripple component is nearly in-phase with the position ripple. In effect, the compensator can use the position ripple in the compensator of Chapter 4 in place of the torque ripple.

The following data presented has been determined by cross-correlating the position ripple with the stator currents (i.e., phase A, B). This is due to the fact that the primary conception of the torque ripple compensator used the stator currents for the parameter update laws. The data and observations collected, however, can be applied to the case in

which the update laws use the field functions instead. Since, the position control experiment is rather detailed, the data presented is broken up into sections for clarity.

Understanding the Position Control Loop. The purpose of this experiment was to observe various signals of the vector controller under position control. In this experiment the flux command was held constant (i.e., 0.4 Wb) and a weight suspended. As the weight was increased it was observed that (1) the magnitude of the stator current increased, (2) the magnitude of the torque commanded (i.e., reference) from the position controller increased, and (3) the magnetic field frequency increased. The effect of $H_3(s)$ (see Figure 5.4) in the position feedback loop was also observed in this experiment. The plant $H_3(s)$ models the vector controller from position control input to motor output. An accurate model was not obtained since the plant in reality changes with each new weight suspended. However, the critical point of observation in the experiment was the phase shift of the position ripple with respect to the stator current. It was documented that the phase relation of these two signals increased as (e.g., 0° to greater than 90°) as more weight was suspended.

Weight Selection in Relation to Torque Ripple Compensation. Clearly, the selection of the weight for suspension is an important criterion in order for this technique to work. The approach presented here was tested over a gamut of flux references. The idea was to choose a weight that would excite a sustained oscillatory mode, but not to choose a weight that would push the phase relation between the position ripple and the reference current waveforms passed 90 degrees. As discussed in Chapter 4, the phase relation must be less than 90 degrees for successful cross correlation in the determination of the required

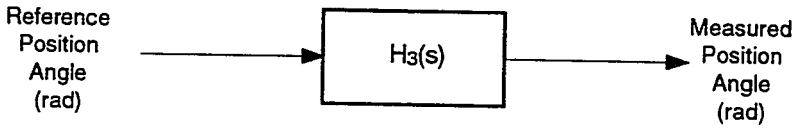

Figure 5.4. Position Feedback Loop Transfer Function.

parameters. The testing of this ripple compensator proceeded by using a high flux command of 0.40 webers and weights of 10, 15, 20, 22.5, and 25 lbs. It was observed that by using the lower weights, a high convergence rate could be established, but as the weight level was increased the rate of convergence was much slower up to the point where it diverged. Clearly, as more weight was added the position ripple and current became more and more out phase and thus, the 90° correlation interval was ultimately violated. Note, this compensator was also tested using lower flux references and various weights. In each case the results were essentially the same. In other words, each case demonstrated that for a given flux command there is a range of acceptable loading the can be used. In general, this means if the weights chosen are too high the amplifier may saturate and/or the phase difference between the current and position ripple has exceeded the 90 degree limit. On the other hand, if the weights chosen are too low the compensator will converge very slowly or it simply may not have the necessary excitation (i.e., current is too low or the ripple magnitude is too low coupled with the fact that the field frequency is very low) to perform correctly, quickly, and reliably. Note that the estimated bias current nullification terms were relatively the same in all test cases. Furthermore, the estimated bias current nullification terms were consistent with the estimated terms determined by the locked rotor torque ripple compensator.

Observed Data. Before and after "snapshots" of the position and torque waveforms indicate that there is a position resolution inaccuracy of the shaft encoder or there is some type mechanical friction interacting with the measurement. Figure 5.46 demonstrates the measured torque of the loaded induction motor under untuned vector control. Figure 5.48 demonstrates the measured position ripple. Figures 5.47 and 5.49 are the respected frequency spectrums of Figures 5.46 and 5.48. Figures 5.50 through 5.53 demonstrate the measured torque and position measurements with their respected frequency spectrums after tuning. The plots clearly show that there is still a small amount of harmonic ripple

content left as registered by the torque sensor and not the position sensor. In other words, although the position ripple has gone to zero the actual torque ripple (harmonics) has not. The spectrum of the position ripple (i.e., Figure 5.53) clearly demonstrates that their are no harmonics resolved by using the position sensor. As a result of this observation no testing was performed to reduce the harmonic torque ripple components.

Lastly, one final experiment was performed to verify parameter convergence using the field functions. This is shown by a pair of figures. Figure 5.54 demonstrated the measured position and torque ripple signals prior to compensation. Figure 5.55 demonstrates the same signals after compensation. The identified bias current nullification terms were determined as I_{ox} = -0.404 A and I_{oy} = 0.678 A. The weight used measured approximately 14.1 lbs.

Experimental Set No. 8 -Signal and Parameter Sensitivity to Operating Conditions

The purpose of this section is three-fold. First of all, the results of a series of random experiments demonstrating the controller's torque ripple from alternate perspectives is presented. Secondly, this section seeks to enforce the reliability of the compensator by presenting a series of tests which verify the consistency and the robust quality of the parameters identified. Third, one test is documented to show the effect of using the improper field functions in equations (4-20) and (4-21). First of all, in line with the first goal, some analysis was performed on the source of the harmonic torque ripple components. The operating conditions for this set of data are as follows: Ψ_{ref} = 0.2 Wb, ω_r = 0 r/min, Temp. = 27° - 40° C, F_s = 5250 Hz, R_r = 0.82 Ω, L_r = 0.11079 H, and L_m = 0.1080 H. In Figure 5.56 a three dimensional spectrum plot is shown as a function of the measured dc bus voltage. In other words, the locked rotor torque ripple spectrum was collected at increasing bus voltages. Note the increasing number of harmonics as the bus voltage is increased. A similar analysis using the above stated conditions was performed under six locked rotor positions at 60° intervals. This three dimensional spectrum plot is

shown in Figure 5.57. The plot shows the harmonic torque ripple components are slightly dependent on the rotor angular position. In Figure 5.58 and 5.59 the effect of the peaking transfer function model of the torque feedback loop is pronounced. In Figure 5.59 the 6th harmonic is seen to be amplified at or near the resonant frequency. This point is also confirmed from the data of Table 5.1 on page 114.

In order to characterize the effect of torque and flux on the fundamental torque ripple a sequence of tests were carried out. Tables 5.2 and 5.3 both demonstrate that at low flux levels the torque ripple magnitude is much larger than at higher flux levels. Moreover, the phase shift of the torque ripple in relation cos(ρ) is much more significant at lower flux levels. One other test was performed to observe the phase relation of the torque ripple with cos(ρ). In this test, two of three wires of the feeding power to the induction motor were swapped. As discussed in Chapter 2 the effect is the reverse rotation of the motor. Figure 5.60 shows how the phase relation of the locked rotor torque ripple and cos(ρ) is lagging when compared with the leading torque ripple and cos(ρ) of Figure 5.61.

In line with the second goal of this section, to verify the consistency of the estimated parameters found using this proposed scheme, tests were performed under various combinations of flux and torque references. The results of these tests are shown in Tables 5.5 and 5.6. Using the information from these tables Figures 5.62 and 5.63 were generated. Figure 5.62 is a scatter plot of the estimated parameters I_{ox} and I_{oy}. Figure 5.63 is a scatter plot of the 2nd and 6th parameter estimates. As indicated by Figures 5.62 and 5.63 the parameters estimated have preferred regions in the parameter space. Note that the fundamental torque ripple is much more sensitive to parameter variation than the cases dealing with harmonic torque ripples [5].

Finally, Figure 5.64 demonstrates that the convergence of parameters I_{oy} using the improper field functions (not as defined in (4-20) and (4-21). Note how the parameter estimate I_{oy} overshoots and has an increased length of time in convergence.

Discussion and Summary of Experimental Results

At the onset of this project experiments were conducted to investigate the manual identification of the parameters causing the fundamental torque ripple. Initially, there was suspicion that the torque ripple was caused due to offset present in the stator current signal paths. It was believed that this was a result of dc bias current offsets present at the output (reference) stator currents. After manual tuning it was possible to reduce the torque ripple significantly but at a cost of highly nonsinusoidal current waveforms. This was clearly unacceptable, even though it was possible to manually reduce the fundamental torque ripple. As a result of this observation, the approach was switched to manually tuning at the input (measured) stator currents. Again, manual tuning by trial and error was slowly possible, but this time, the stator currents were sinusoidal and the torque ripple was reduced to near zero. Note that in this case no offset tuning was required at the VC output. Thus, it is also important to note that torque ripple production is highly sensitive to dc bias currents at the stator current inputs to the vector controller (i.e., more so than at the reference stator currents). DC bias currents at the input (i.e., measured current) or DAC output (i.e., reference current) of the vector controller will induce torque ripple. Moreover, dc bias currents at the VC input will translate into offsets at the VC reference output, but it is unclear (due to the design of the hardware) how bias current offsets at the reference translate into offsets at the VC measuring input. What is clear from these experiments is that offset present at either the input or output of the vector controller should be nullified at those points and not in an opposing fashion. This is the fundamental premise of torque ripple reduction.

As a result of this observation, the compensator was implemented primarily at the input of the vector controller. It is critically important to mention that the compensation techniques of Chapter 4 (i.e., using sine and cosine) evolved from the experiments of using the stator currents in the parameter update laws. This point was previously mentioned in

the discussion of the position control experiment using the torque ripple compensator. A great deal of experiments were initially performed under this criterion. The notion at first made sense since the controller implemented in the laboratory only used two current measuring transducers. Any dc offset on these signal paths resulted in torque ripple. Therefore, the idea was to identify these terms using the torque ripple and stator currents associated with each signal path. The technique worked but parameter convergence was not always guaranteed and in most cases, the compensator exhibited very slow parameter convergence. The idea of using the field functions sin(ρ) and cos(ρ) came about after observing how well the parameter identification scheme worked in the reduction of the harmonic torque ripple components. The goal was to search for a more unified structure of identifying all the torque ripple model components. The path to this goal was nontrivial and painstakingly long, but in short, the evolution of using the field functions in place of the stator currents i_{sa} and i_{sb} was successful. The key experiments performed in the satisfaction of this goal have been presented.

Clearly, a detailed analysis has been performed on the subject of torque ripple and vector control. In summary the main experimental observations and conclusions from experimental sets No. 1 through No. 8 can be listed as follows:

1. The fundamental torque ripple component exhibited by a vector controller is linked to bias current offsets in the stator current sensing and feedback paths.

2. The torque ripple magnitude and phase is dependent on the magnitudes of the bias current offsets I_{ox} and I_{oy}.

3. As a result of these offsets nonlinearities arise in various signals used in vector control (e.g., nonlinear ρ or nonsinusoidal currents).

4. Rapid parameter convergence of I_{ox} and I_{oy} is dependent on proper selection of the field functions and gain terms in the parameter update laws. The rate of convergence is also dependent on the field frequency.

5. Parameter convergence of all modeled torque ripple parameters is guaranteed provided that the level of excitation is significant and that the transfer function of the torque feedback loop does not contribute 90° phase shift.

6. Feedforward cancellation of the higher torque components is effective in locked rotor experiments using the torque sensor in the compensator.

7. Fundamental ripple compensation is possible using the torque sensor in a speed controlled vector controller.

8. Fundamental ripple compensation is possible using the position sensor (which registers the position ripple) in a position controlled vector controller.

Conclusion

The torque ripple reduction scheme proposed in this thesis is based on the assumption that the source of torque ripple can be modeled as a periodic torque disturbance and the frequency of this torque disturbance is same as the field frequency. This assumption is inspired by results from analysis and laboratory experiments. A model governing the effects of circuit offset in the current sensing data acquisition path has been derived. The coefficients of this model and the harmonic torque ripple model are estimated by using an identification scheme. The fundamental ripple component is reduced by introducing the estimated current bias offsets into the current sensing path. The inverse of the harmonic torque ripple is approximated using the estimated parameters of the harmonic model and then introduced to the system to cancel the actual ripple. The aforementioned experimental results clearly indicate as in Figure 5.5 the effectiveness of the proposed scheme.

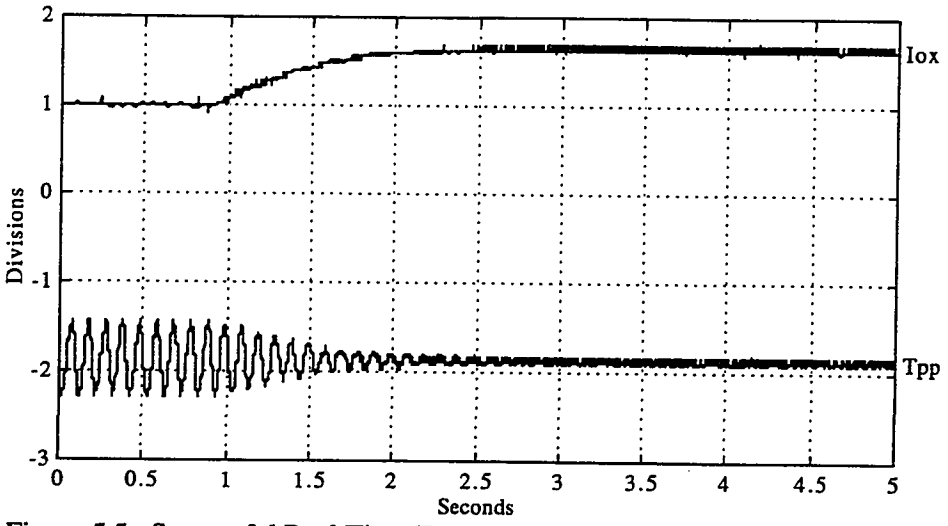

Figure 5.5. Successful Real Time Torque Ripple Minimization as Proposed by the Compensator.

Experimental Data Observed

Experimental Figures

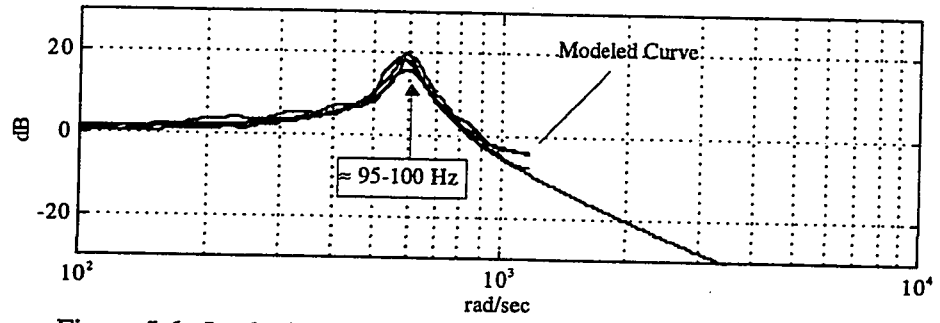

Figure 5.6. Locked Rotor System Frequency Response (Magnitude).[1]

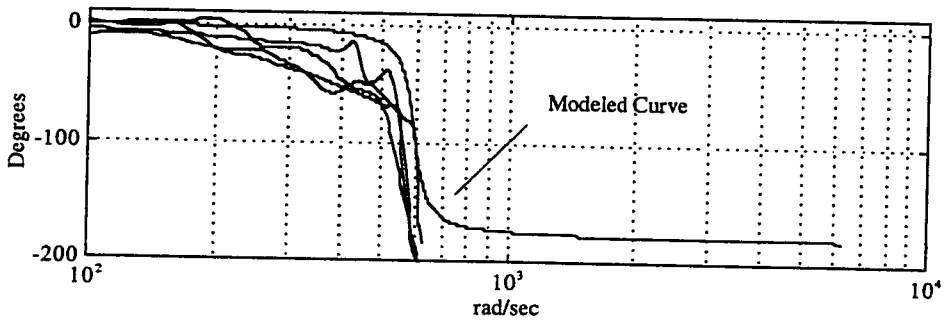

Figure 5.7. Locked Rotor System Frequency Response (Phase).

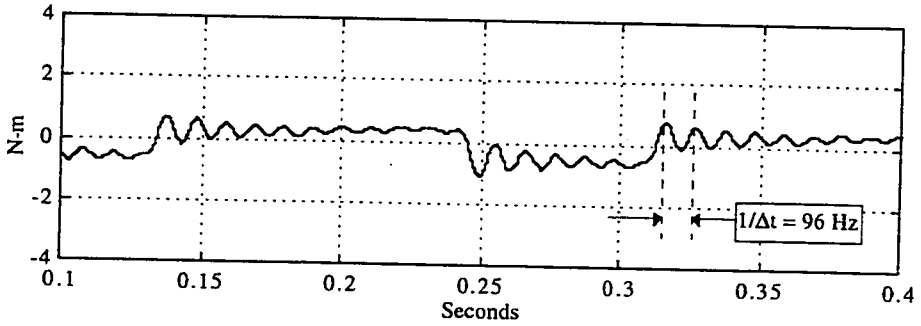

Figure 5.8. Locked Rotor System Step Response.

[1] System Swept from 2.3 - 186 Hz.

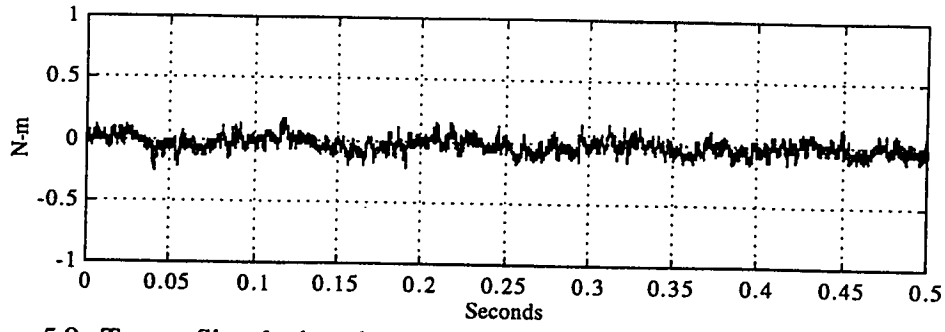

Figure 5.9. Torque Signal when the Vector Controller is Enabled and the Torque Sensor Uncoupled from the Locked Rotor of the Motor.

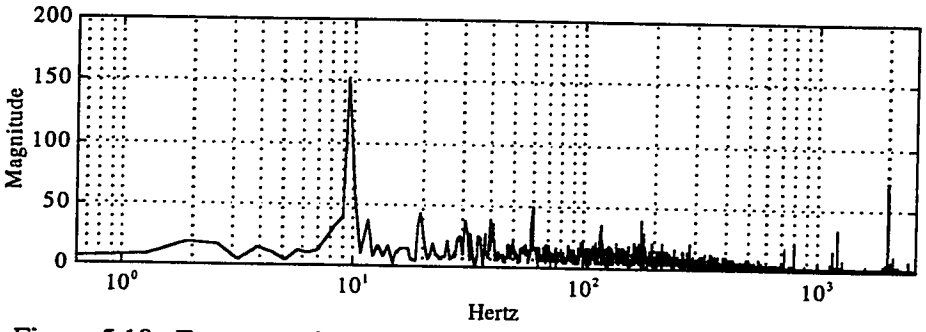

Figure 5.10. Frequency Spectrum of the Torque Signal shown in Figure 5.9.

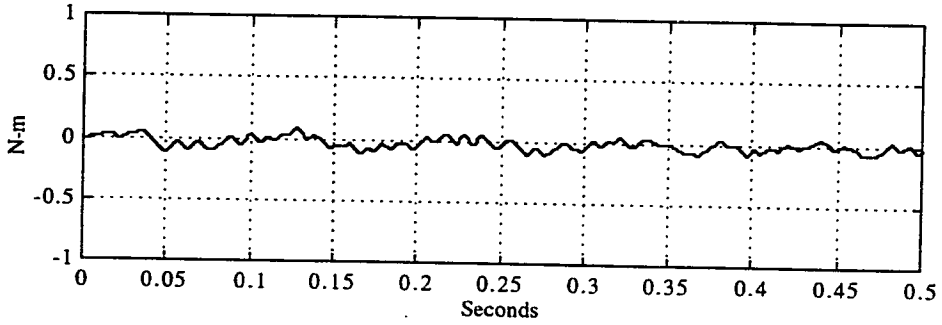

Figure 5.11. Filtered Version of Figure 5.9 using a 100 Hz Eight Order Butterworth Digital Filter implemented in MATLAB.

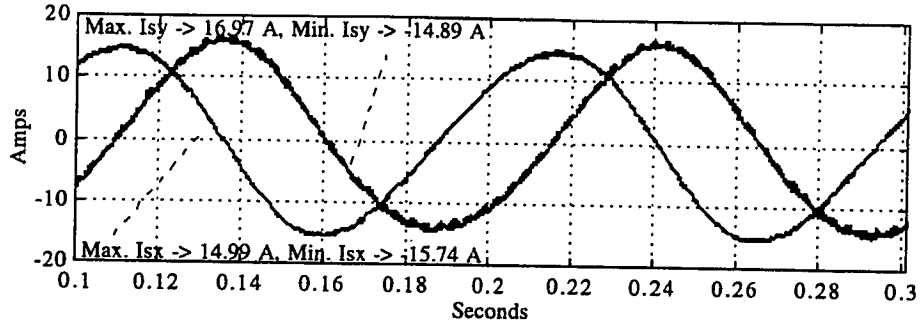

Figure 5.12. Two-Axis Measured Stator Currents i_{sx} and i_{sy} with Bias Current Offsets.

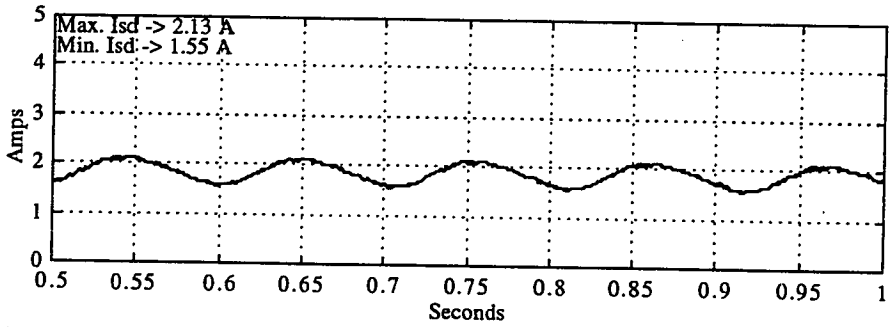

Figure 5.13. Time Varying Direct Current Component I_{sd} in Rotor Flux Frame as a Result of Bias Current Offsets.

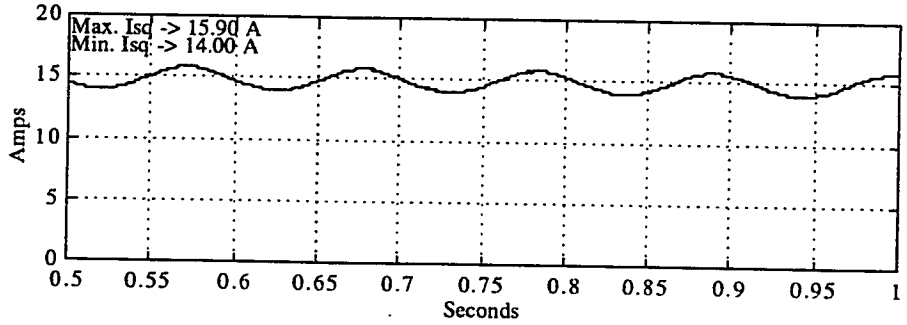

Figure 5.14. Time Varying Quadrature Current Component I_{sq} in Rotor Flux Frame as a Result of Bias Current Offsets.

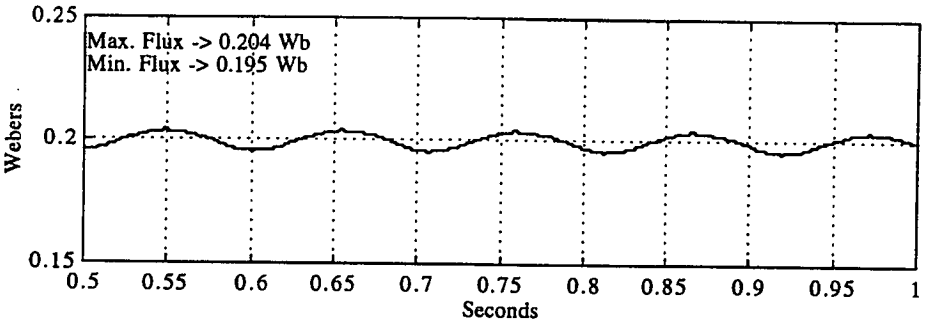

Figure 5.15. Time Varying Rotor Flux $|\Psi_r|$ Observed as a Result of Bias Current Offsets.

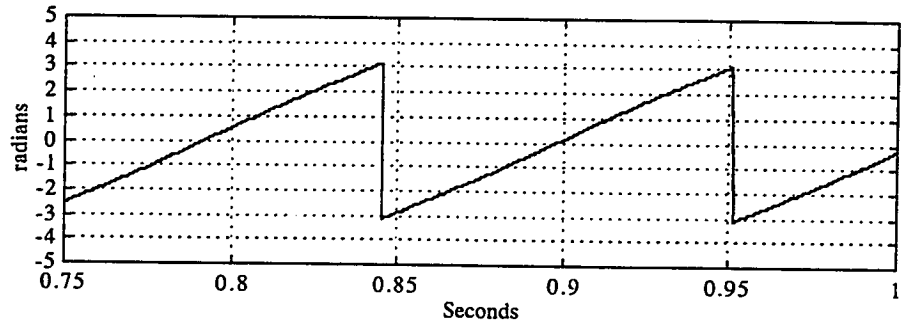

Figure 5.16. Nonlinear Slip Angle α as a Result of Bias Current Offsets.

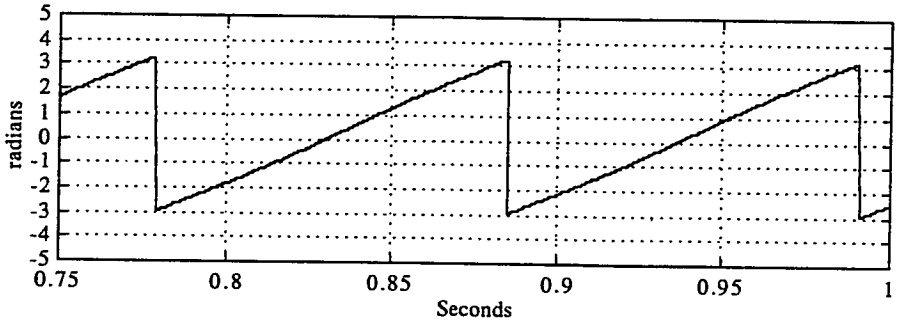

Figure 5.17. Nonlinear Rotor Flux Angle ρ as a Result of Bias Current Offsets.

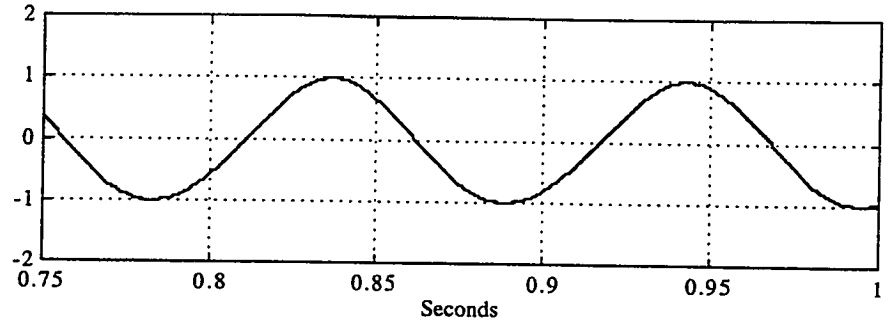

Figure 5.18. Nonsinusoidal Version of cos(ρ) as a Result of Bias Current Offsets.

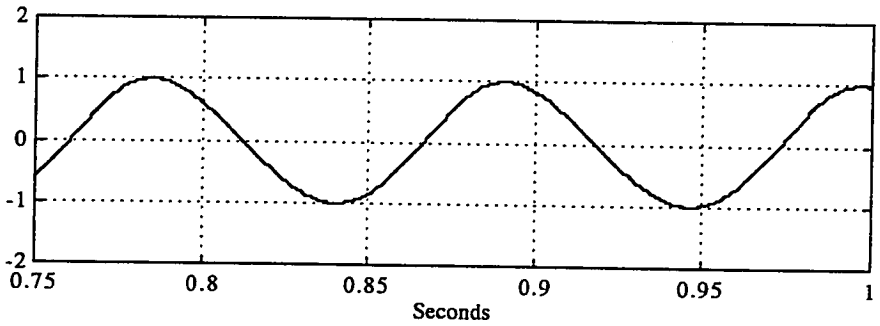

Figure 5.19. Nonsinusoidal Version of sin(ρ) as a Result of Bias Current Offsets.

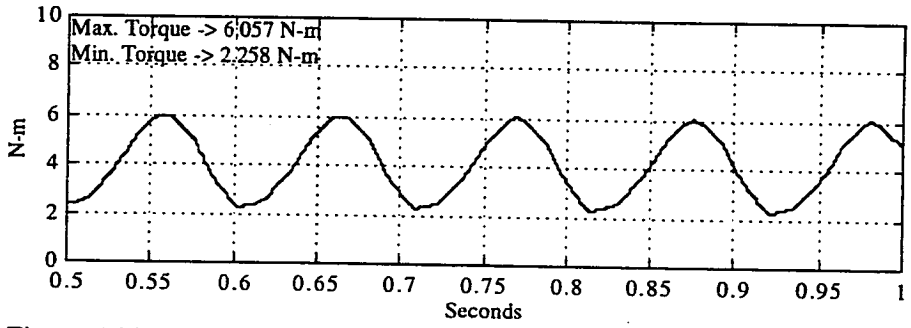

Figure 5.20. Torque Ripple of the Induction Machine Under Vector Control.[2]

[2] Data filtered in MATLAB using a 100 Hz 8th order Butterworth lowpass filter.

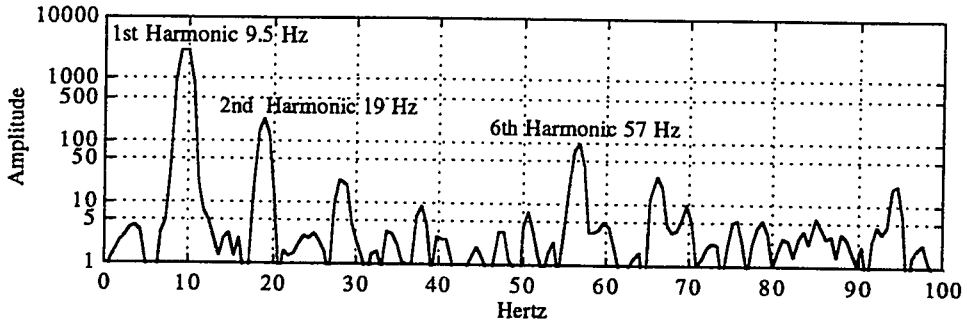

Figure 5.21. FFT Frequency Spectrum of the Measured Torque Ripple of Figure 5.20.[3]

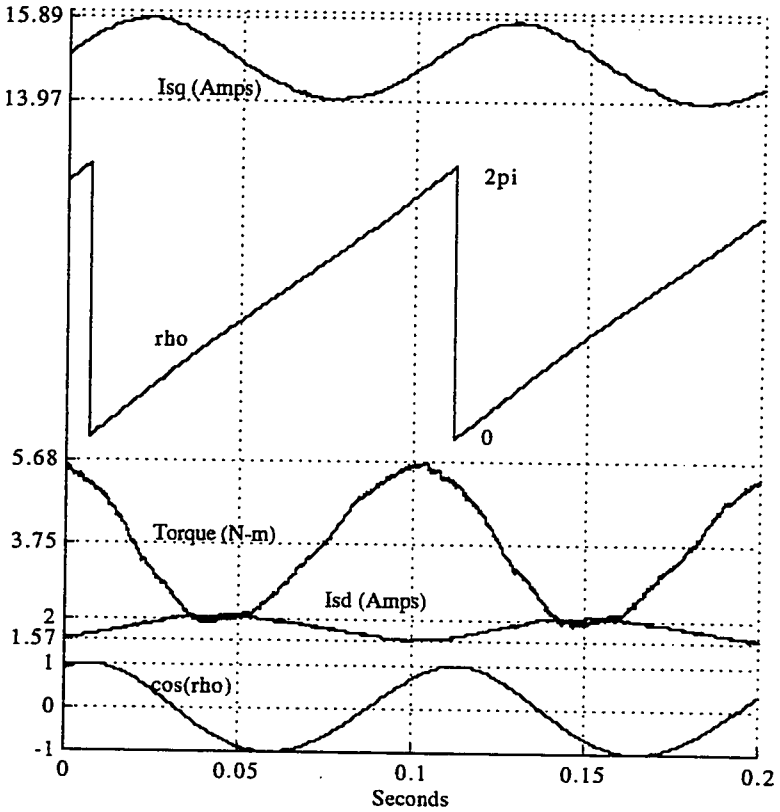

Figure 5.22. Selected Control Parameters of an Untuned Vector Controller.[4]

[3] Kaiser window used for spectral resolution. Note that the frequency spectrum plots presented in this thesis all utilize a 8192 point FFT.

[4] All signals sampled simultaneously under locked rotor conditions.

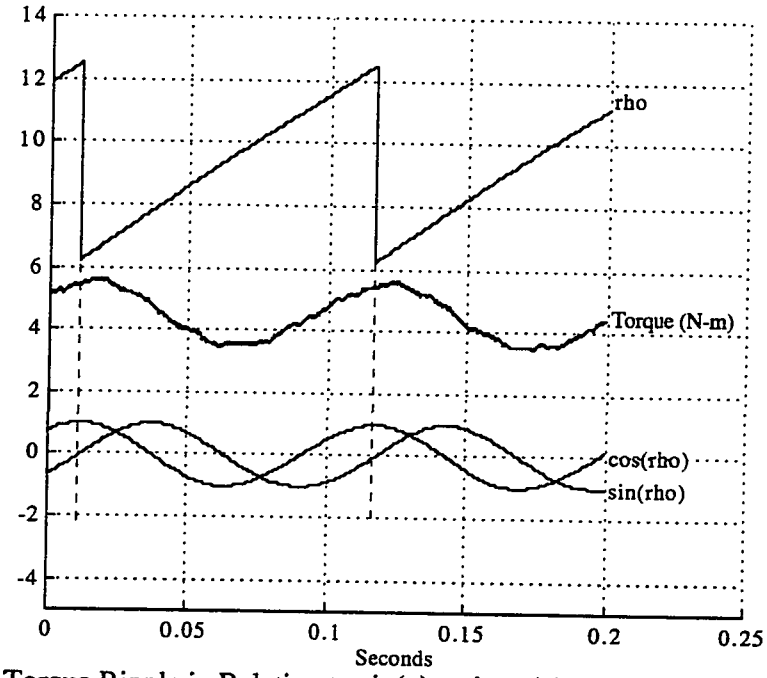

Figure 5.23. Torque Ripple in Relation to sin(ρ) and cos(ρ) with $I_{ox} = 0$ A, $I_{oy} = 0.645$ A.

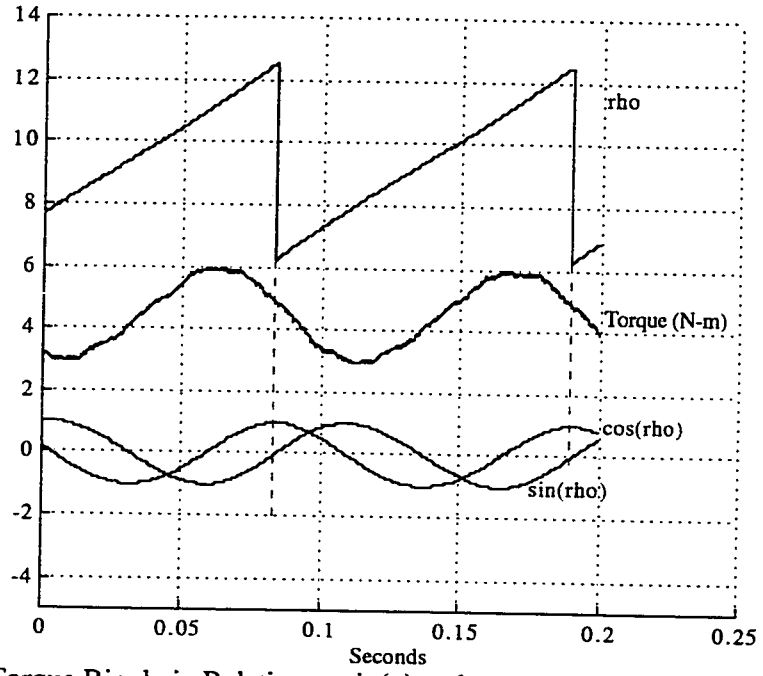

Figure 5.24. Torque Ripple in Relation to sin(ρ) and cos(ρ) with $I_{ox} = -0.416$ A, $I_{oy} = 0$ A.

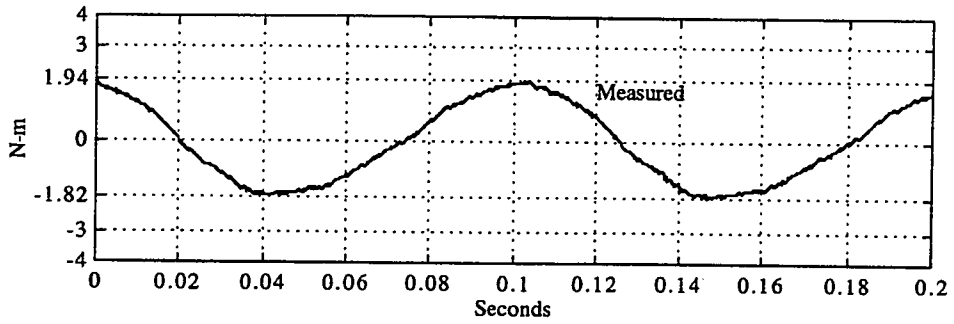

Figure 5.25. Measured Torque Ripple of Figure 5.22.[5]

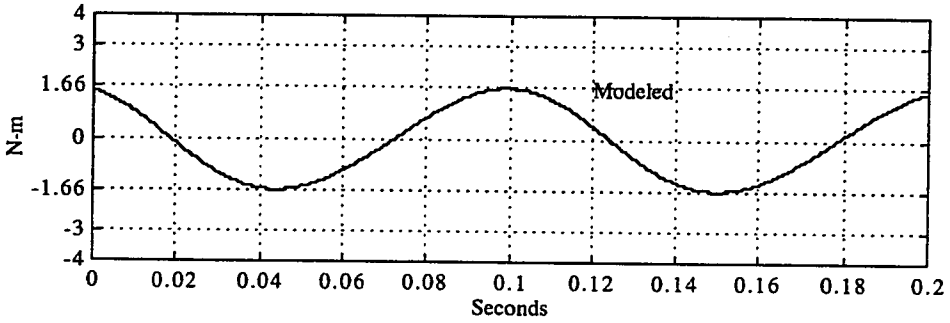

Figure 5.26. Modeled Version of Figure 5.25 using Equation (4-18).

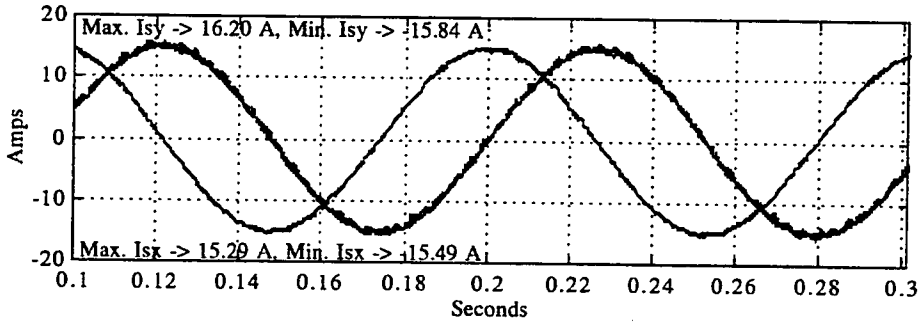

Figure 5.27. Two-Axis Measured Stator Currents i_{sx} and i_{sy} with Bias Current Nullification.

[5] Filtered data with steady state torque removed.

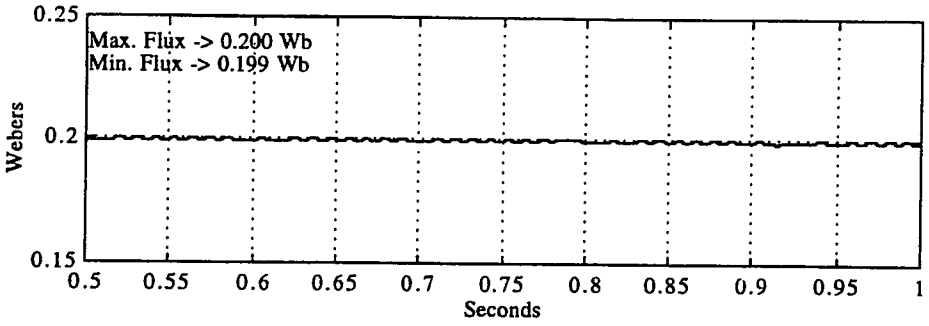

Figure 5.28. Rotor Flux $|\Psi_r|$ Observed as a Result of Bias Current Nullification.

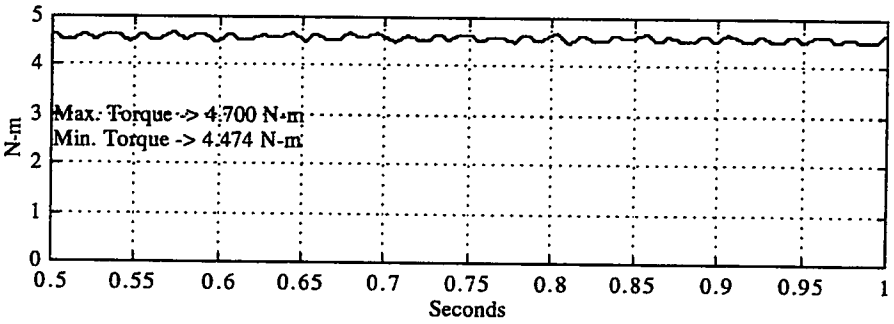

Figure 5.29. Torque Measurement Where Fundamental Torque Ripple Component is Removed as a Result of Bias Current Nullification.[6]

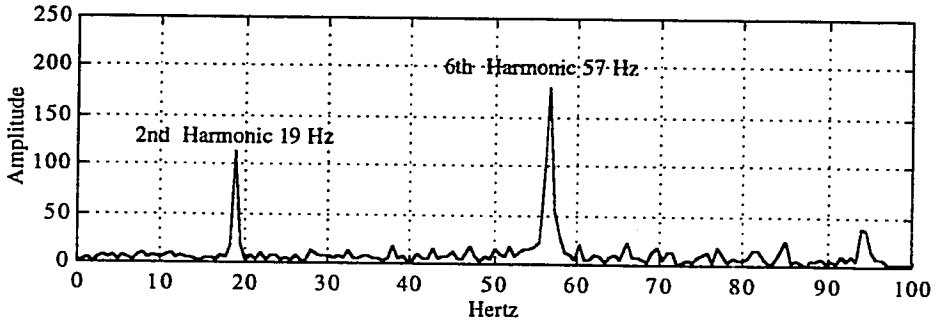

Figure 5.30. Frequency Spectrum of Figure 5.29 Demonstrating the Remaining Harmonic Torque Ripple Components.

[6] 100 Hz lowpass filtered data. Note signal generated under locked rotor conditions.

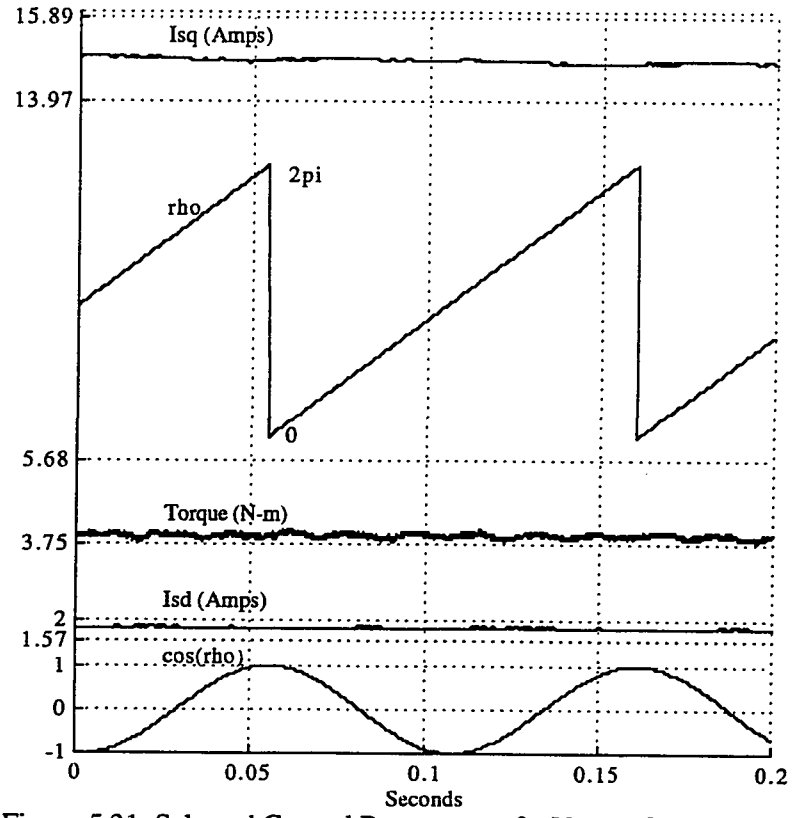

Figure 5.31. Selected Control Parameters of a Vector Controller as a Result of Bias Current Nullification.

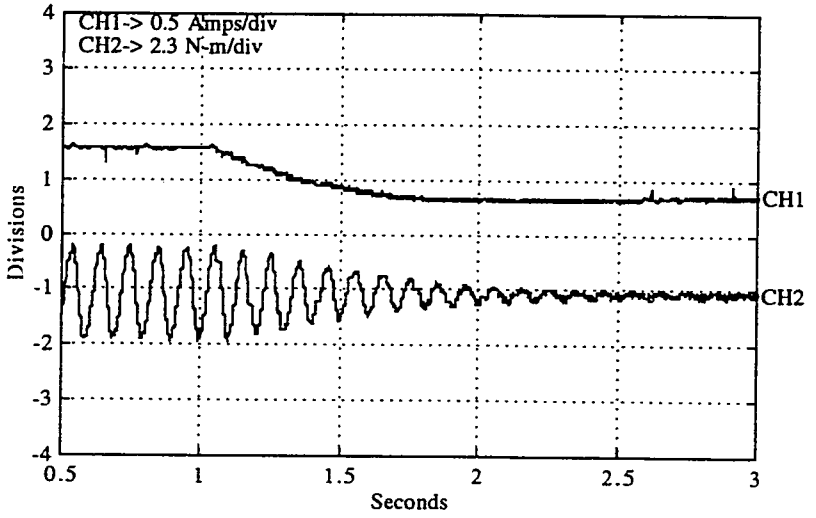

Figure 5.32. Real Time Torque Ripple Reduction as Parameter I_{ox} Converges.[7]

[7] Sampled on Tektronix 2212 oscilloscope.

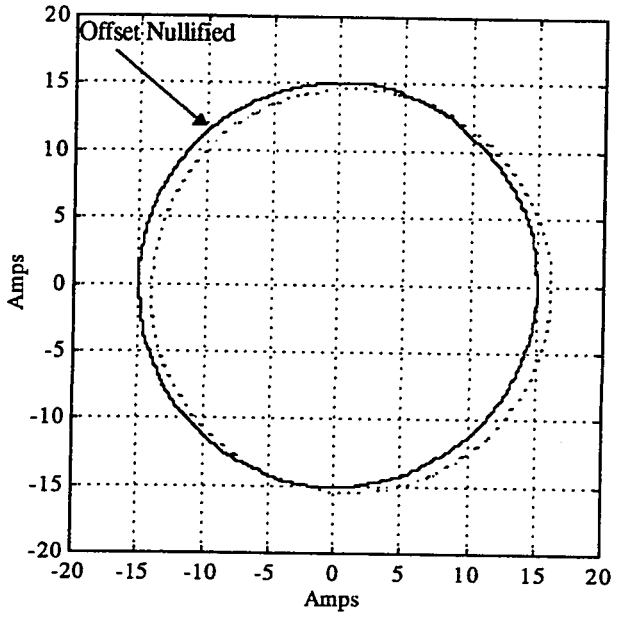

Figure 5.33. Lissajous Pattern of i_{sy} vs. i_{sx}.[8]

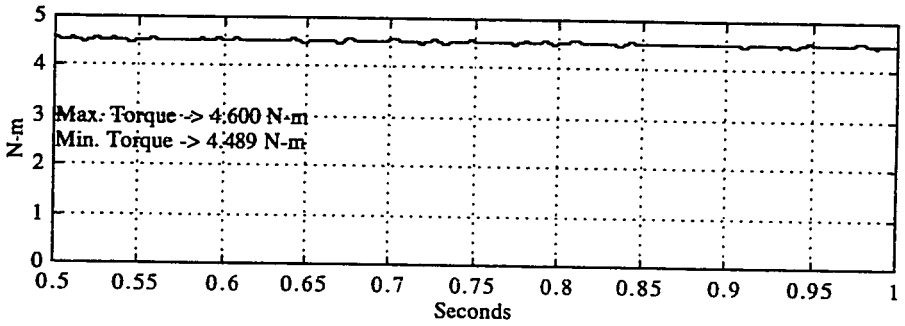

Figure 5.34. Torque Measurement after all Ripple Components are Removed.[9]

[8] Two patterns demonstrating the resulting shift of the circle before and after compensation. Dotted line represents case prior to compensation. Solid line represents case after compensation.
[9] 100 Hz filtered data. Signal generated under locked rotor conditions.

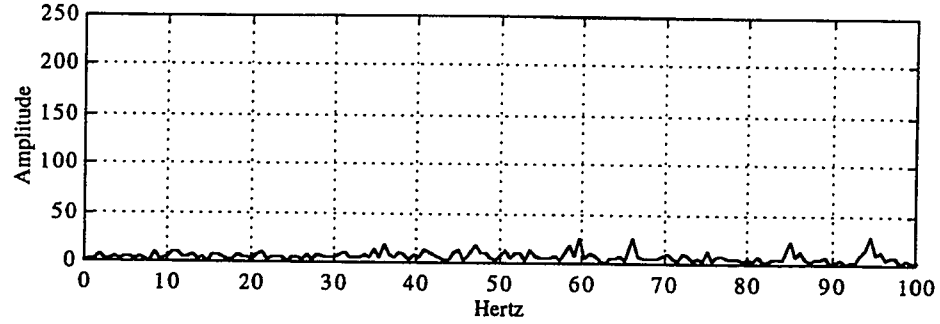

Figure 5.35. Resulting Frequency Spectrum after Complete Ripple Compensation.

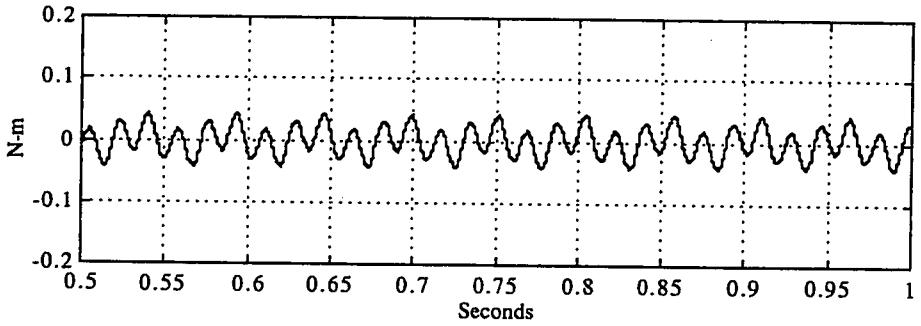

Figure 5.36. Sample Feedforward Cancellation Term T_f..

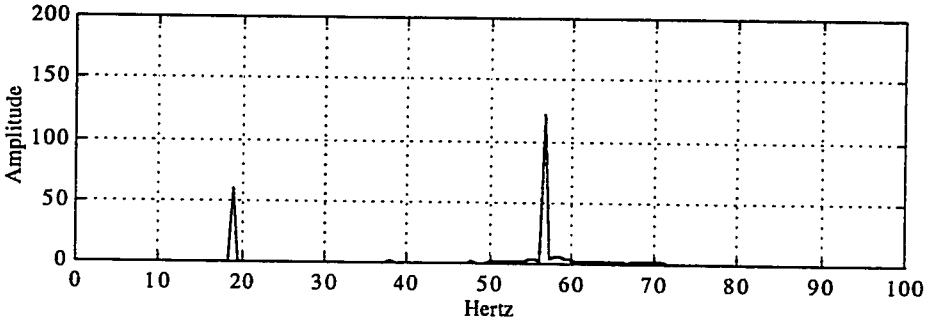

Figure 5.37. Frequency Spectrum of Figure 5.36.

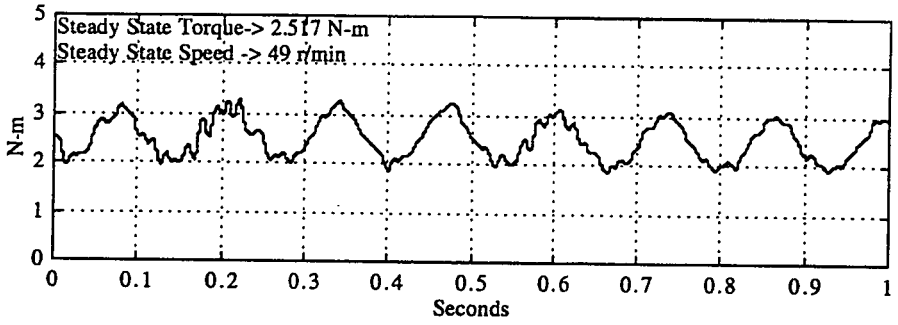

Figure 5.38. Dynamic Torque Ripple Under Open Loop Vector Control at a Steady State Speed of 49 r/min.[10]

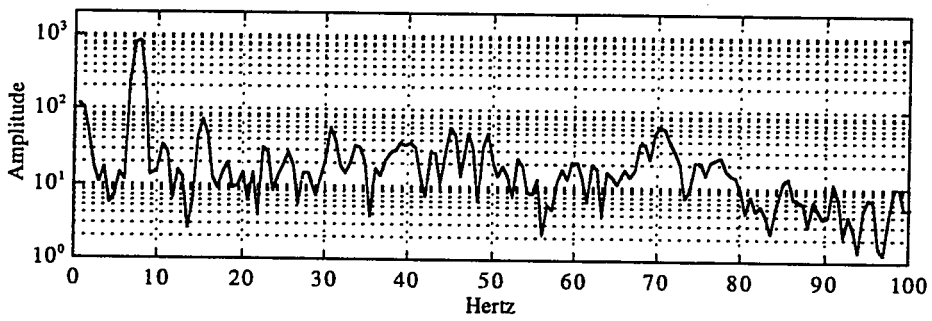

Figure 5.39. Frequency Spectrum of the Figure 5.38.[11]

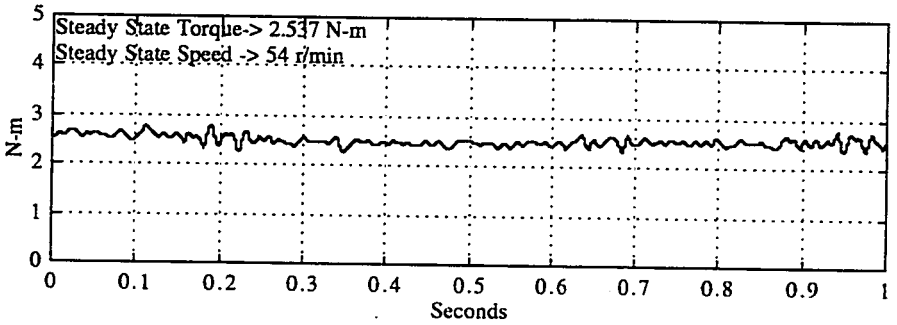

Figure 5.40. Torque Measurement of a Tuned Open Loop Vector Controller.[12]

[10] Low speed experiment. Signal low pass filtered at 100 Hz.
[11] Kaiser window used.
[12] Low speed experiment. Signal low pass filtered at 100 Hz.

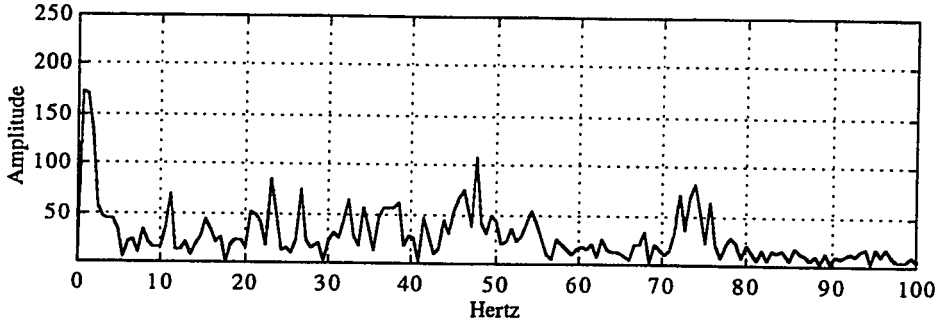

Figure 5.41. Frequency Spectrum of Figure C.35.

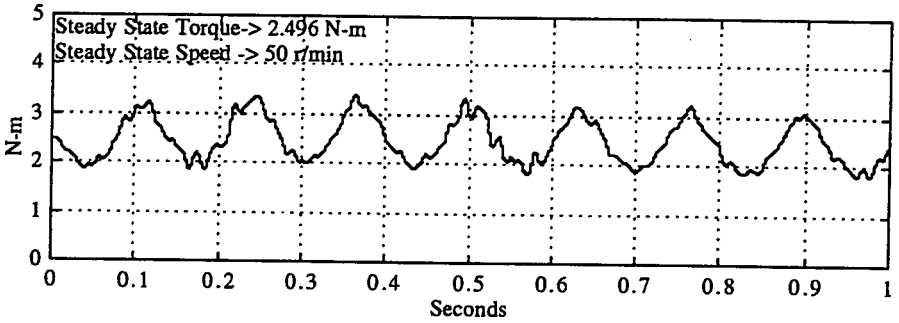

Figure 5.42. Measured Torque Ripple of an Untuned Vector Controller Driven by an Outer Loop Speed Controller.[13]

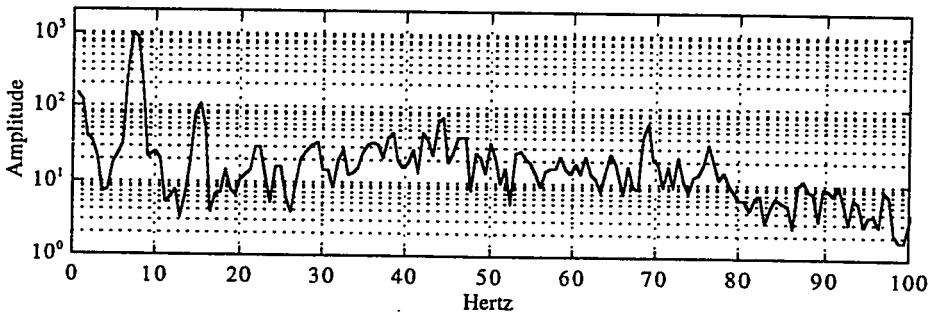

Figure 5.43. Frequency Spectrum of Figure C.37.[14]

[13] Low speed experiment. Signal low pass filtered at 100 Hz.
[14] Kaiser window used.

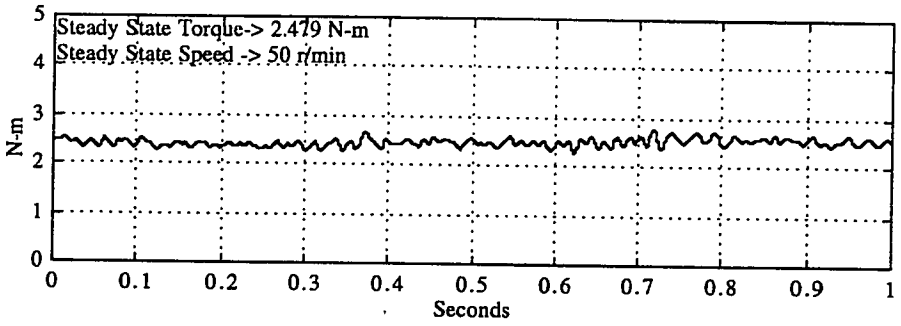

Figure 5.44. Torque Measurement of a Tuned Vector Controller Driven by an Outer Loop Speed Controller.[15]

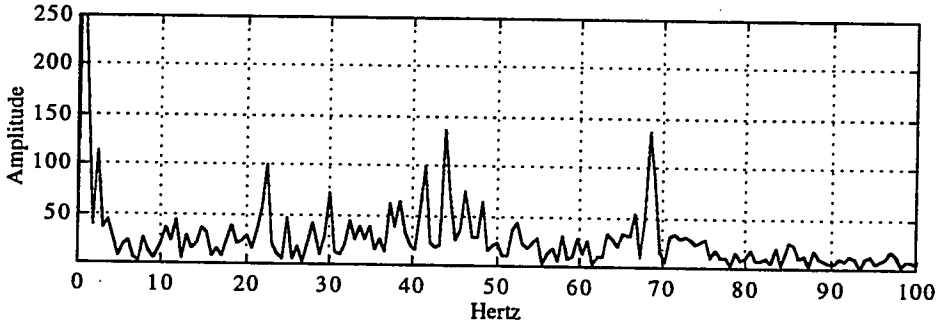

Figure 5.45. Frequency Spectrum of Figure 5.44.

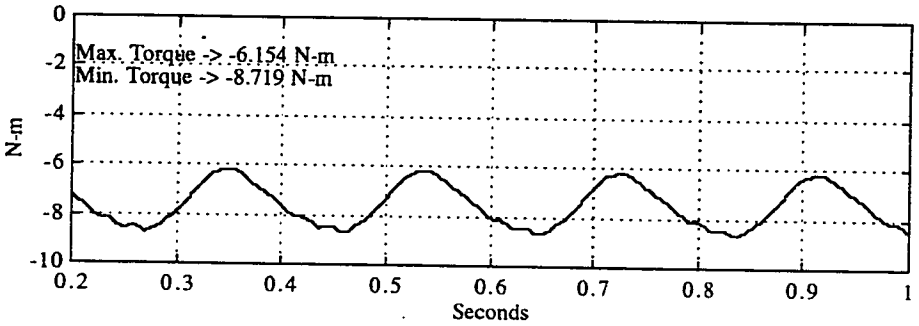

Figure 5.46. Torque Measurement of an Untuned Vector Controller Driven by an Outer Loop Position Controller.[16]

[15] Low speed experiment. Signal low pass filtered at 100 Hz.

[16] Zero speed experiment. Signal generated by lifting and suspending 15.9 lbs via a cable/pulley mechanism. Signal lowpass filtered at 100 Hz.

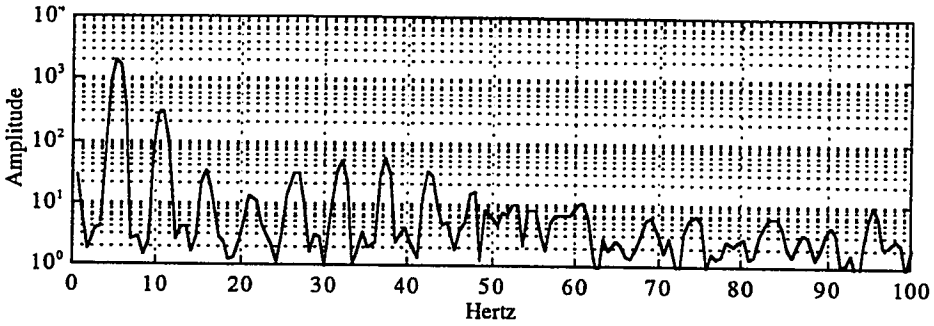

Figure 5.47. Frequency Spectrum of Figure 5.46

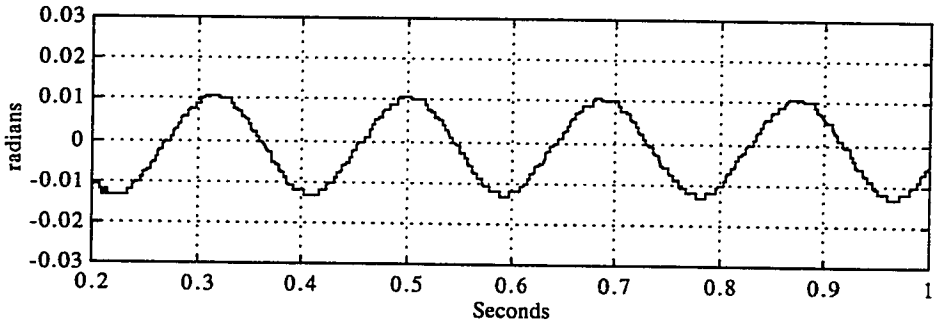

Figure 5.48. Position Measurement of an Untuned Vector Controller Driven by an Outer Loop Position Controller.[17]

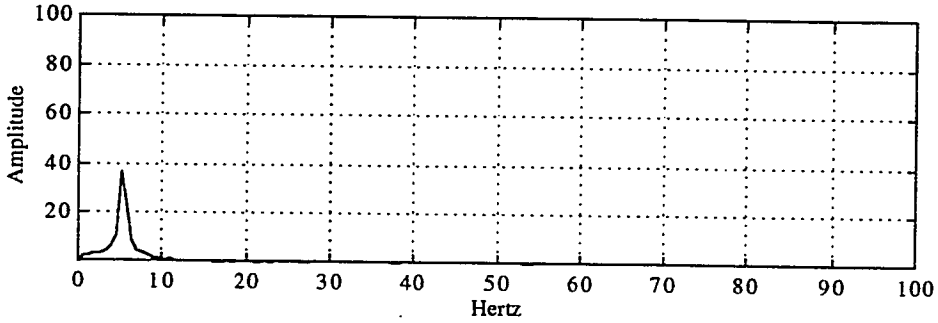

Figure 5.49. Frequency Spectrum of Figure 5.48.

[17] Same experimental conditions as used in the generation of Figure 5.46.

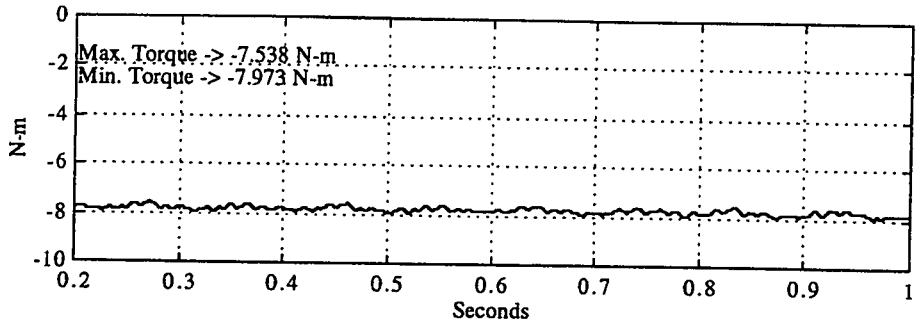

Figure 5.50. Torque Measurement of a Tuned Vector Controller Driven by an Outer Loop Position Controller and Compensated using the Position Ripple.[18]

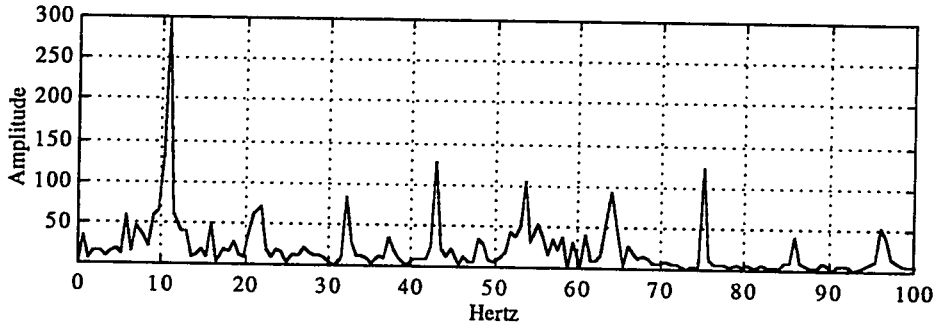

Figure 5.51. Frequency Spectrum of Figure 5.50.

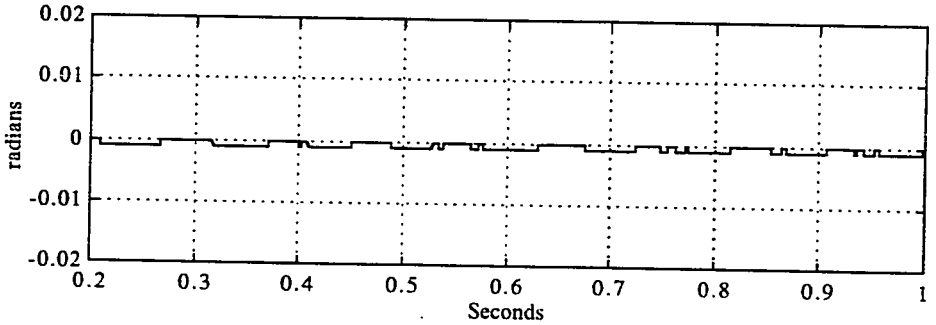

Figure 5.52. Position Measurement of a Tuned Vector Controller Driven by an Outer Loop Position Controller.[19]

[18] Zero speed experiment. Signal generated by lifting and suspending 15.9 lbs via a cable/pulley mechanism. Signal lowpass filtered at 100 Hz.

[19] Same experimental conditions as used in the generation of Figure 5.50.

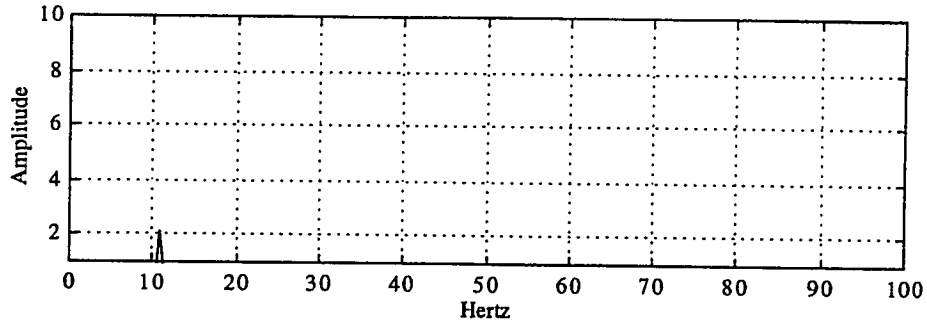

Figure 5.53. Frequency Spectrum of Figure 5.52.

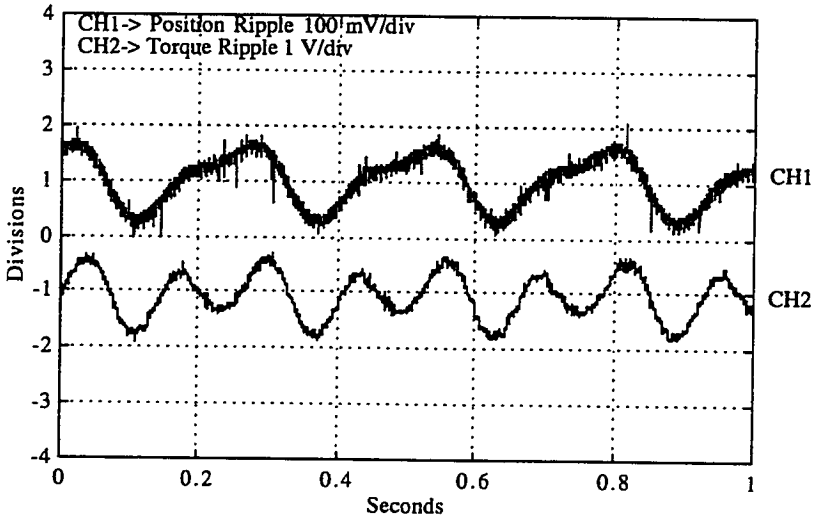

Figure 5.54. Position and Torque ripple Measurements Prior to Compensation .[20]

[20] Zero speed experiment. Signal generated by lifting and suspending 14.1 lbs via a cable/pulley mechanism. Sampled on Tektronix 2212 oscilloscope.

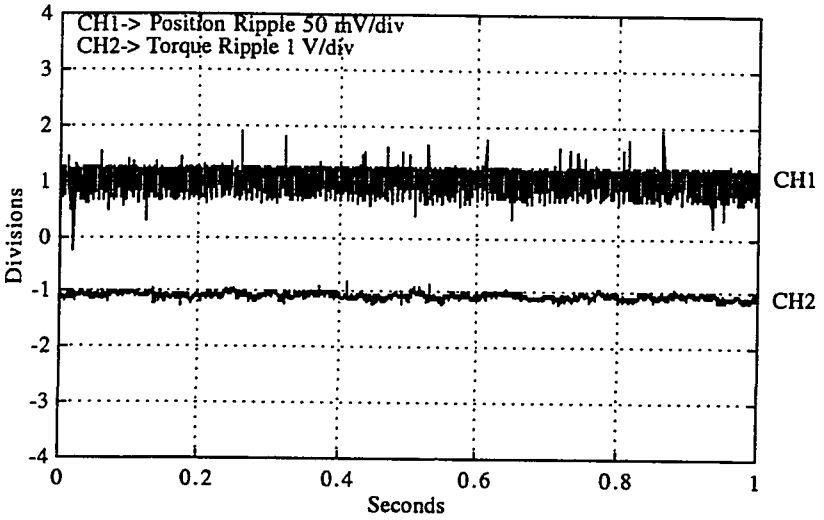

Figure 5.55. Position and Torque ripple Measurements After Compensation.[21]

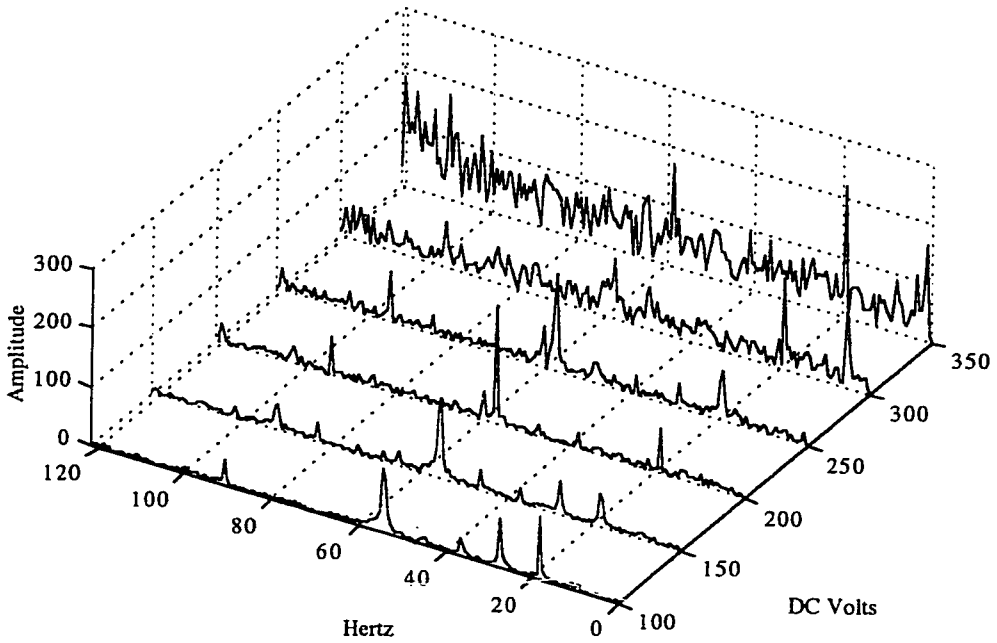

Figure 5.56. Harmonic Torque Ripple Spectrum vs. Relative DC Bus Voltages.

[21] Same conditions as in the generation of Figure 5.54. Sampled on Tektronix 2212 oscilloscope.

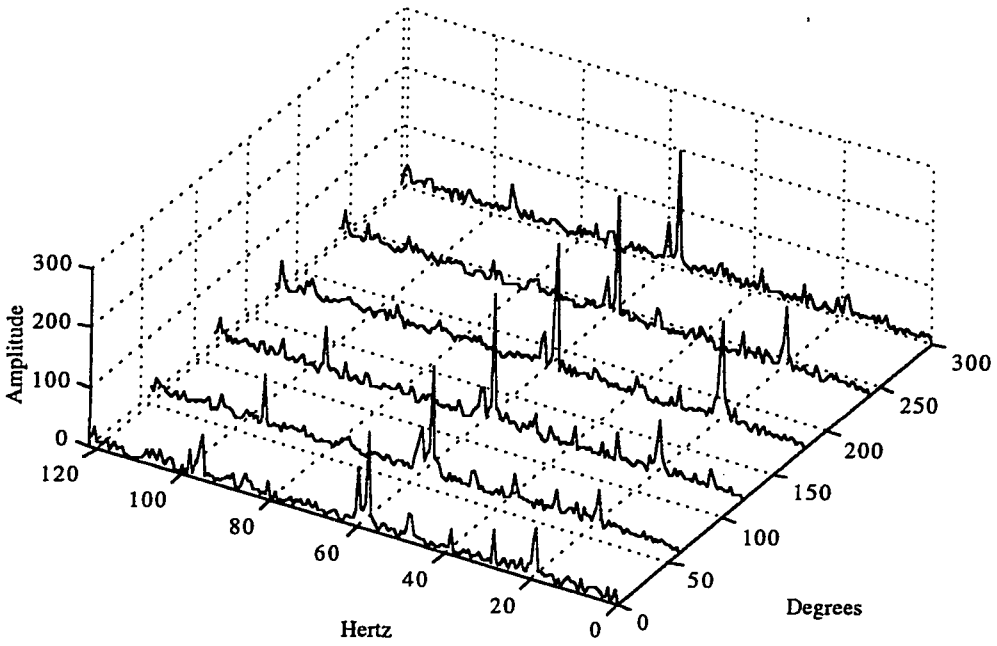

Figure 5.57. Harmonic Torque Ripple Spectrum vs. Rotor Angular Position.

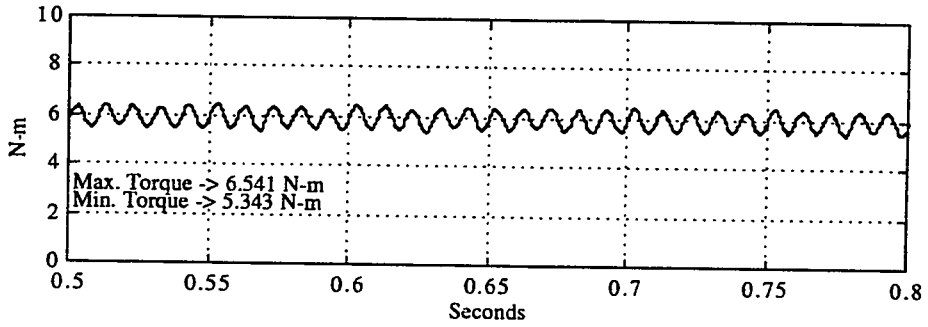

Figure 5.58. Torque Measurement Demonstrating the Excitation of the 6th Harmonic Due to the Resonant Mode Present in the Torque Feedback Loop.[22]

[22] Locked rotor filtered measurement.

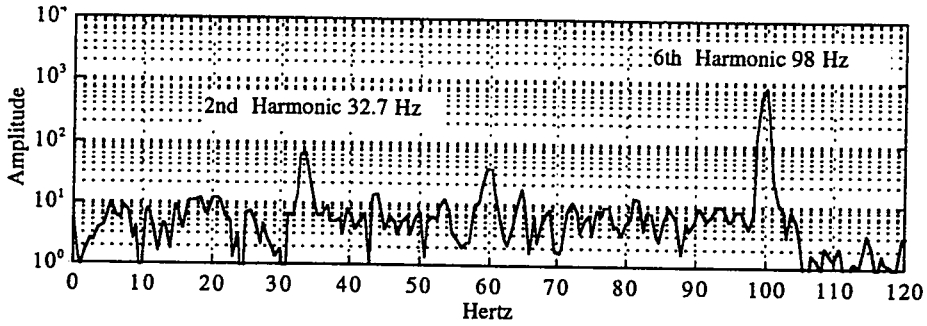

Figure 5.59. Frequency Spectrum of Figure 5.59.

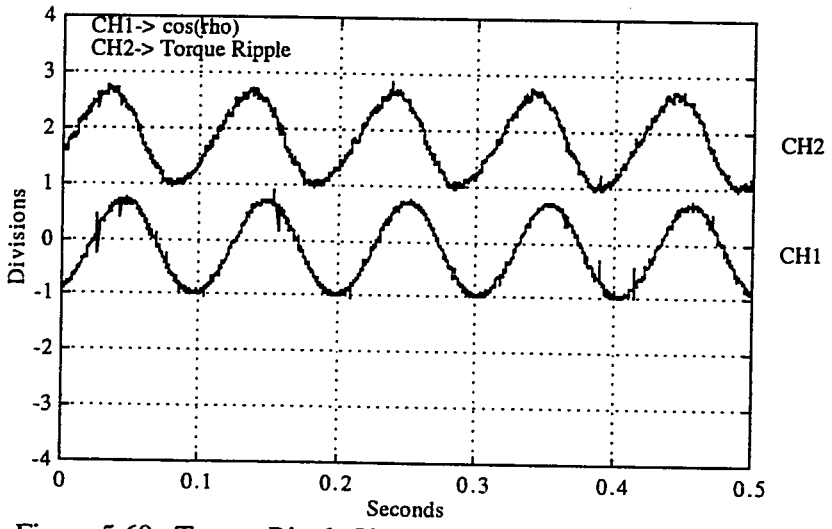

Figure 5.60. Torque Ripple Under Locked Rotor Conditions.[23]

[23] Clockwise rotor motion or forward locked direction. Sampled on Tektronix 2212 oscilloscope.

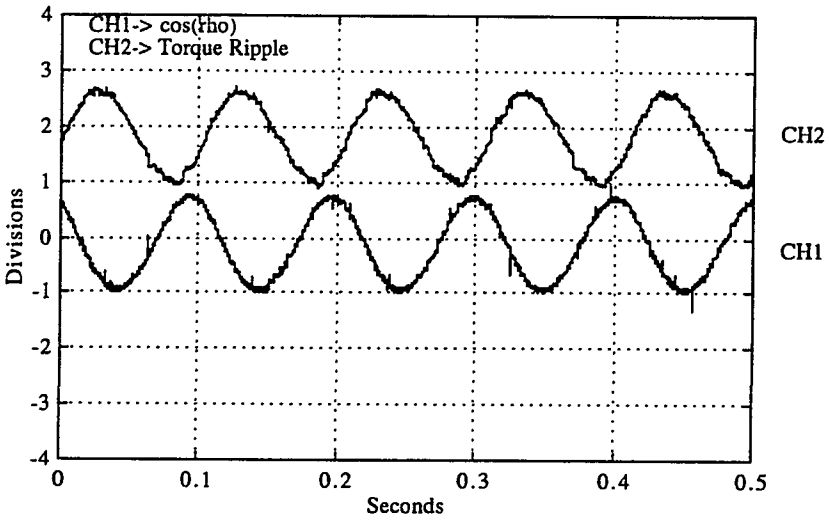

Figure 5.61. Torque Ripple Under the Same Commanded Signals as in Figure 5.60 with Two Power Conductors Swapped.[24]

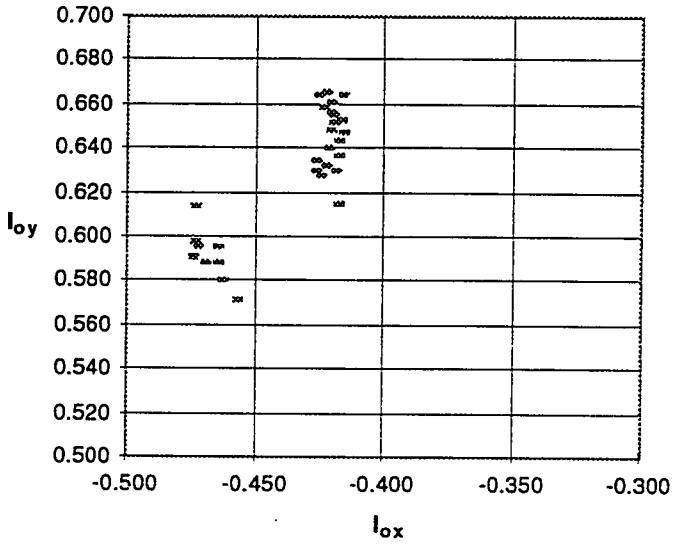

Figure 5.62. Regions of Convergence for the Fundamental Torque Ripple Parameter Estimates.

[24] Counterclockwise rotor motion or reverse locked direction. Sampled on Tektronix 2212 oscilloscope.

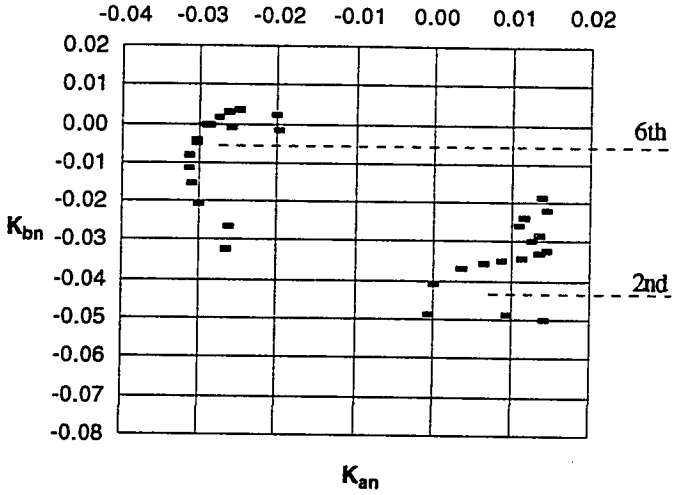

Figure 5.63. Regions of Convergence for the Harmonic Torque Ripple Parameter Estimates.

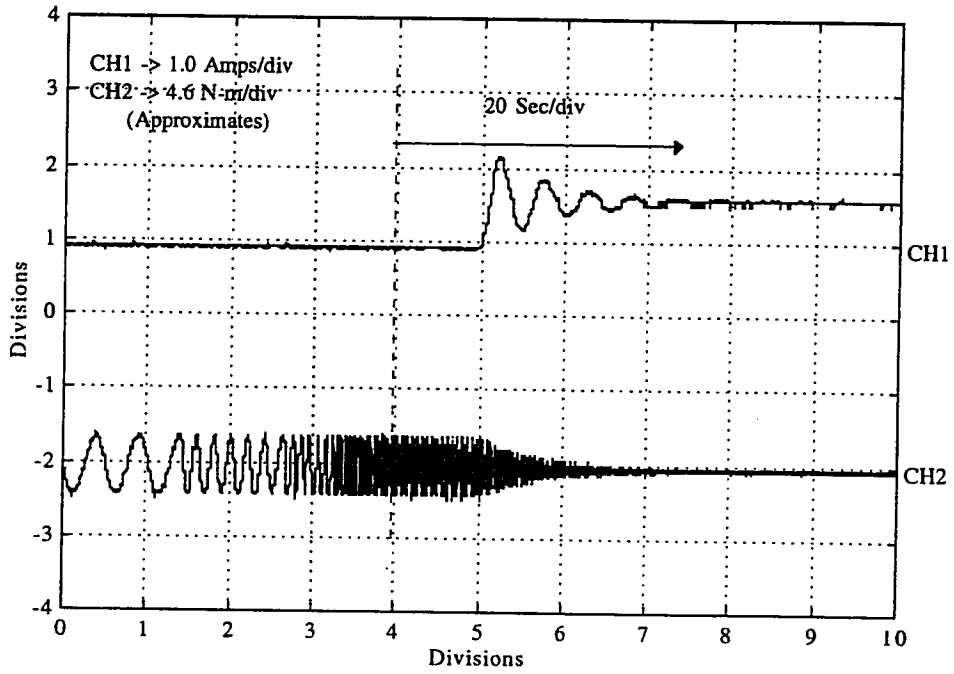

Figure 5.64. Real Time Ripple Reduction as Parameter I_{oy} Converges.[25]

[25] Note update laws(4-20) and (4-21) in this case use -sin(ρ) and cos(ρ) respectively. Sampled on Tektronix 2212 oscilloscope.

Experimental Tables

Table 5.1

Data Defining the Amplification of the 6th Torque Harmonic due to Plant Dynamics.

Flux Reference (Wb)	Torque Reference (N-m)	Fundamental Freq.† (Hz)	6th Harmonic Freq.† (Hz)	FFT Amplitude†
0.25	4	6.07	36.42	99
0.20	4	9.53	57.18	200
0.19	4	10.48	62.88	258
0.18	4	11.60	69.60	292
0.17	4	12.80	76.80	369
0.16	4	14.42	86.52	517
0.15	4	16.20	97.20	818
0.14	4	18.48	110.88	1618
0.13	4	20.75	124.50	391
0.12	4	23.67	142.02	200

†Data collected with rotor locked.

Table 5.2

Data Set A Characterizing the Fundamental Torque Ripple Component Under a Combination of Flux and Torque References.

Flux Reference (Wb)	Torque Reference† (N-m)	Measured Torque‡ (N-m)	Phase Shift§ (Degrees)	Ripple Freq. (Hz)
0.2	2	2.05	32.6	4.78
"	4	3.88	56.1	9.69
"	6	5.94	56.9	14.23
"	8	6.86	46.0	18.53
0.3	4	2.59	38.7	4.25
"	6	3.63	49.4	6.37
"	8	4.55	50.9	8.48
"	10	5.15	45.9	10.64
"	12	6.03	40.9	12.47
0.4	6	2.52	34.1	3.54
"	8	3.21	41.7	4.82
"	10	3.74	42.5	6.03
"	12	4.25	51.6	7.14
"	14	5.18	36.1	8.38
0.5	8	2.56	36.2	3.08
"	10	2.98	40.9	3.85
"	12	3.37	44.8	4.61
"	14	3.78	44.8	5.41
"	16	4.14	46.5	6.07
"	18	4.34	48.5	6.91
0.6	4	1.16	-8.9	1.06
"	6	1.32	0.0	1.58
"	8	1.62	10.2	2.12
"	10	1.78	17.1	2.67
"	12	2.06	21.8	3.22
"	14	2.20	26.8	3.77
"	16	2.38	27.7	4.26
"	18	2.47	28.5	4.78
"	20	2.61	29.3	5.35

†Clockwise or forward direction torque reference.

‡Peak to peak time varying locked rotor torque with steady state torque removed.

§Phase shift in respect to cos(ρ) where the torque ripple is leading.

Table 5.3

Data Set B Characterizing the Fundamental Torque Ripple Component Under a Combination of Flux and Torque References.

Flux Reference (Wb)	Torque Reference† (N-m)	Measured Torque‡ (N-m)	Phase Shift§ (Degrees)	Ripple Freq. (Hz)
0.2	-2	2.01	105.0	4.86
"	-4	3.81	112.7	9.43
"	-6	5.43	113.3	13.82
"	-8	6.96	116.9	17.84
0.3	-4	2.59	98.4	4.24
"	-6	3.49	95.9	6.29
"	-8	4.71	115.6	8.25
"	-10	5.01	115.4	10.43
"	-12	5.77	108.8	12.45
0.4	-6	2.50	100.7	3.60
"	-8	3.14	104.0	4.76
"	-10	3.58	106.0	5.97
"	-12	4.06	113.8	7.09
"	-14	4.55	107.9	8.32
0.5	-8	2.19	97.9	3.05
"	-10	2.58	107.5	3.75
"	-12	2.98	107.0	4.61
"	-14	3.14	104.5	5.28
"	-16	3.58	111.8	6.18
"	-18	3.58	107.7	6.86
0.6	-4	1.11	64.4	1.05
"	-6	1.32	62.7	1.58
"	-8	1.36	68.8	2.10
"	-10	1.71	86.5	2.64
"	-12	1.71	87.7	3.22
"	-14	1.83	94.0	3.72
"	-16	2.31	97.6	4.23
"	-18	2.66	104.9	4.80
"	-20	3.44	103.5	5.23

†Counterclockwise or reverse direction torque reference.

‡Peak to peak time varying locked rotor torque with steady state torque removed.

§Phase shift in respect to cos(ρ) where the torque ripple is leading.

Table 5.4

Modeled Data Characterizing the Fundamental Torque Ripple Component Under a Combination of Flux and Torque References.

Flux Reference (Wb)	Torque Reference (N-m)	Modeled Torque† (N-m)	Modeled Phase Shift† (Degrees)
0.2	2	1.71	42.6
"	4	3.35	49.2
"	6	5.01	51.5
"	8	6.67	52.7
0.3	4	2.30	40.9
"	6	3.38	45.9
"	8	4.48	48.4
"	10	5.58	49.9
"	12	6.68	50.9
0.4	6	2.62	38.3
"	8	3.43	42.6
"	10	4.24	45.2
"	12	5.06	47.0
"	14	5.88	48.3
0.5	8	2.84	35.5
"	10	3.47	39.4
"	12	4.12	42.0
"	14	4.76	44.0
"	16	5.42	45.4
"	18	6.08	46.6
0.6	4	1.64	8.8
"	6	2.05	20.3
"	8	2.53	27.7
"	10	3.03	32.7
"	12	3.54	36.3
"	14	4.07	38.9
"	16	4.60	40.9
"	18	5.14	42.6
"	20	5.68	43.9

†Data generated by using equation (4-18).

Table 5.5

Identified Current Bias Offsets under a combination of Flux and Torque References.

Flux Reference (Wb)	Torque Reference (N-m)	Iox† (A)	Ioy† (A)	Magnitude
0.2	2	-0.418	0.653	0.775
"	4	-0.427	0.664	0.789
"	6	-0.424	0.666	0.790
"	8	-0.417	0.664	0.784
0.3	4	-0.423	0.640	0.767
"	6	-0.422	0.656	0.780
"	8	-0.425	0.659	0.784
"	10	-0.417	0.647	0.770
"	12	-0.421	0.655	0.779
0.4	6	-0.422	0.648	0.773
"	8	-0.422	0.656	0.780
"	10	-0.421	0.652	0.776
"	12	-0.422	0.661	0.784
"	14	-0.418	0.653	0.775
"	16	-0.419	0.644	0.768
"	18	-0.419	0.637	0.762
0.5	8	-0.420	0.630	0.757
"	10	-0.428	0.630	0.762
"	12	-0.426	0.628	0.759
"	14	-0.428	0.634	0.765
"	16	-0.424	0.632	0.761
"	18	-0.419	0.615	0.744
0.6	4	-0.475	0.614	0.776
"	6	-0.475	0.598	0.764
"	8	-0.474	0.595	0.761
"	10	-0.464	0.580	0.743
"	12	-0.466	0.589	0.751
"	14	-0.466	0.595	0.756
"	16	-0.476	0.591	0.759
"	18	-0.471	0.589	0.754
"	20	-0.458	0.571	0.732

†Data collected with rotor locked.

Table 5.6

Identified Harmonic Model Parameters.

Flux Reference (Wb)	Model Parameters (N-m)†				Fundamental Freq. (Hz)
	k_{2a}	k_{2b}	k_{6a}	k_{6b}	
0.40	-0.028	0.013	-0.001	-0.027	2.393
0.35	-0.022	0.014	-0.001	-0.020	3.154
0.30	-0.019	0.013	0.002	-0.021	4.272
0.25	-0.024	0.011	0.004	-0.026	5.901
0.24	-0.026	0.011	0.003	-0.027	6.524
0.23	-0.030	0.012	0.002	-0.028	7.230
0.22	-0.032	0.014	0.000	-0.029	7.918
0.21	-0.033	0.013	-0.001	-0.030	8.639
0.20	-0.034	0.011	-0.004	-0.031	9.420
0.19	-0.035	0.008	-0.005	-0.031	9.852
0.18	-0.036	0.006	-0.008	-0.032	10.810
0.17	-0.037	0.003	-0.011	-0.032	12.000
0.16	-0.041	0.000	-0.015	-0.032	13.370
0.15	-0.048	-0.001	-0.021	-0.031	16.810
0.14	-0.048	0.009	-0.026	-0.027	19.380
0.11	-0.050	0.014	-0.032	-0.027	22.650
0.12	-0.047	0.012	-0.027	-0.020	26.690

†Data collected under constant torque reference of 4 N-m.

APPENDIX A

Torque Sensor Amplifier and Filtering Circuit

In order to perform torque ripple reduction utilizing the torque sensor as specified in Chapter 4, it is imperative to extract the large dc component present in the torque measurement. In general, this extraction can be performed through the implementation of either a hardware or software based highpass filter. The simplest form of a hardware filter which could be used is a very large coupling capacitor [29]. On the other hand, it is impractical and very difficult to find bipolar capacitors larger than 5 μF. Furthermore, at sufficiently low frequencies, the time varying torque signal of interest may be attenuated significantly [29]. Although, it is completely possible to use this approach or to construct a typical highpass filter (e.g. Butterworth, Chebychev), a more sophisticated circuit as shown in Figure A.1 on page 123 is utilized for greater flexibility in the analysis of the torque measurement.

This circuit depicted in Figure A.1 is equivalent to a low-bandwidth highpass filter. The circuit is designed such that the user may analyze various permutations of the torque measurement. The circuit consists of two main sections since the torque sensor outputs two forms of the torque measurement: 1. High frequency. 2. Low frequency. The first output contains both the ac and dc transient signals limited by a bandwidth of 300 Hertz. The second output is a one Hertz lowpass version of the first output. Due to the fact that the given torque transducer used in this project was designed for heavy torque applications, the outputs of both these signals for torque measurements between 0 and 10 N-m were in the millivolt range. Moreover, these signals were not immune to levels of noise generated by the PWM inverter and the three phase autotransformer used in varying the dc bus voltage of the inverter. Therefore, in order to maximize the ADC sampling resolution of these two torque signals and to improve the signal to noise ratio, two instrumentation amplifiers (i.e., AD524) were selected [32]. The gains for both instrumentation amplifiers

are identically preset by the user to maximize sampling resolution. The other amplifiers (i.e., AD713) are good quality general purpose operational amplifiers [32].

The extraction of a dc free transient signal from the torque measurement begins by utilizing the outputs of the amplified signals from the torque sensor. The idea is to pass both these signals through a differential amplifier such that the resulting output is simply a noninverted dc free high frequency signal. To ensure that the time varying characteristics of the lower frequencies of interest (i.e., 0.5 to 30 Hz) are attenuated significantly, the amplified low frequency output is passed through four lowpass filters which are separated using voltage followers (buffers). This will guarantee that the transient response of the combined filter will be critically damped. The cutoff frequencies of the individual filters were set so reasonable, practical resistor and capacitor values could be selected and such that there was significant attenuation between 0.5 and 30 Hz (i.e., 80 dB roll-off at approximately 0.5 Hertz).

High Pass Digital Filter Realization

In the implementation of the position/torque ripple compensator a digital highpass filter was designed to extract the time varying position ripple component. Since the position measurement is internally computed (from information provided by a shaft encoder) in the source code, a software based filter was utilized. There are two classes of software digital filters that could have been used. The first is the finite impulse response (FIR) digital filter and the second is the infinite impulse response (IIR) digital filter [26]. There are multiple design tradeoffs between the two classes of filters [26]. Given the fact that there is a wealth of knowledge on the design and realizations of IIR continuous time filters, the traditional approach involves designing a discrete time filter by transforming the continuous time prototype filter (e.g. Butterworth or Chebychev) [26]. Since the position/torque ripple compensator requires a simple filter, an IIR filter was selected.

In order to design an IIR digital filter based on an analog prototype, a set of specifications were predescribed to the conform to the specifications of the given vector controller. The position/torque ripple compensator as described in Chapter 4 requires the use of a highpass filter that yields a maximally flat frequency response with little or no phase shift at the frequencies of interest. To satisfy this condition a second order Butterworth highpass filter with a cutoff frequency set at 0.1 Hertz was designed. This filter resulted in zero attenuation of frequencies of interest above one Hertz with a maximally flat frequency response. The frequencies approaching dc were attenuated at 40 dB per decade. Furthermore, the phase shift of the frequencies above one Hertz approached zero. The coefficients of the required difference equation were found using the command "butter" in MATLAB [34]. A block diagram representation of the difference equation is shown in Figure A.2 on page 124. The difference equation, which is the inverse Z-transform of equation (A-1), is programmed in "C" as shown in the code of Figure A.3. The filter is implemented as a periodic function call from the main program. Note that since the sampling interval of the Vector Controller implemented was 5200 Hertz (i.e., sampling frequency used in the position control experiments only), a delay loop (i.e. software counter) was added in implementing the filter. This enabled the use of reasonable, practical coefficients. At a sampling frequency of 5200 Hertz very high resolution is required to design a 0.1 Hertz filter.

$$H(z) = \frac{b_0 + b_1 z^{-1} + b_2 z^{-2}}{1 + a_1 z^{-1} + a_2 z^{-2}}. \qquad \text{(A-1)}$$

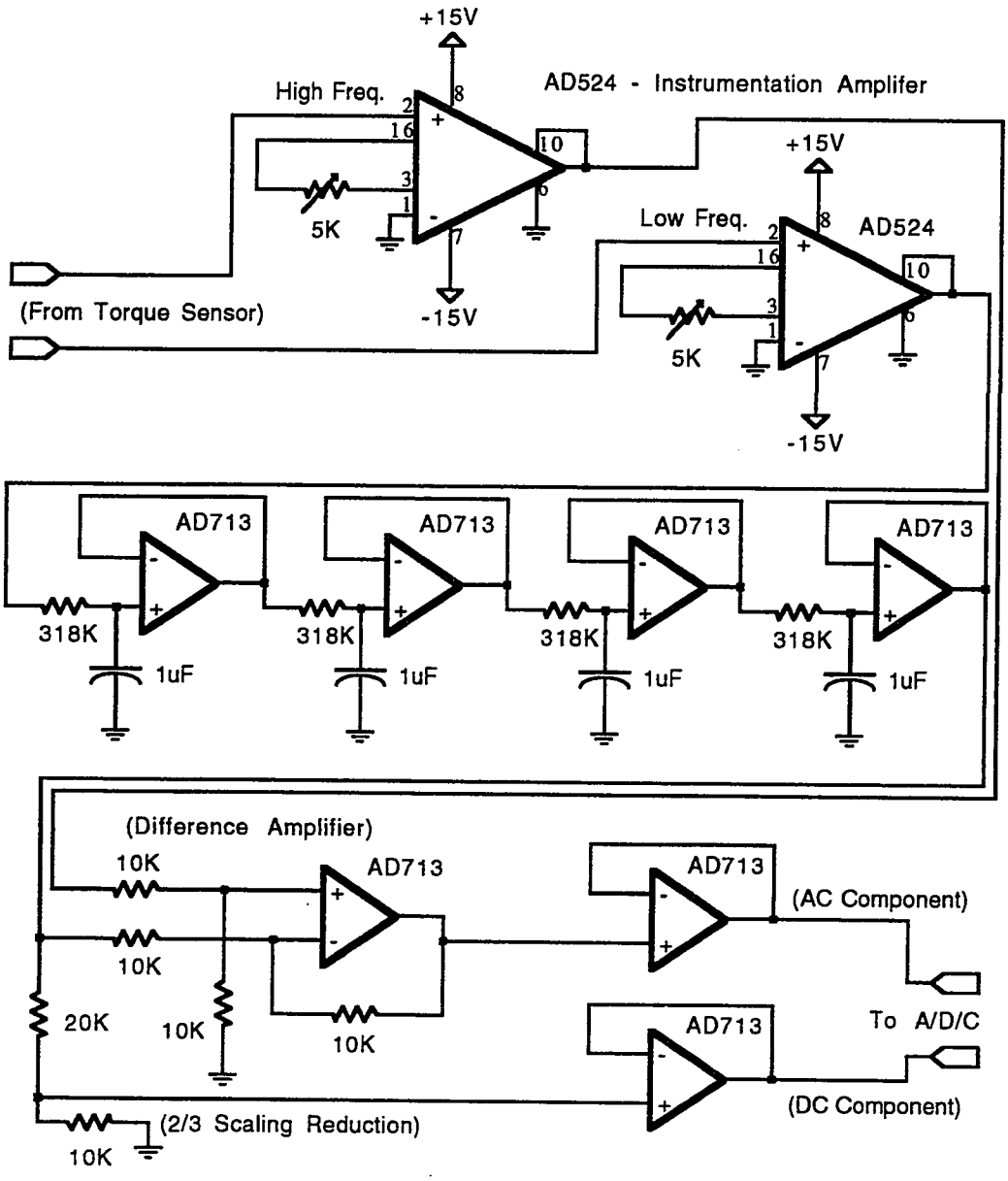

Figure A.1. Amplification and Filtering Circuit for Torque Sensor Data Acquisition and Analysis.

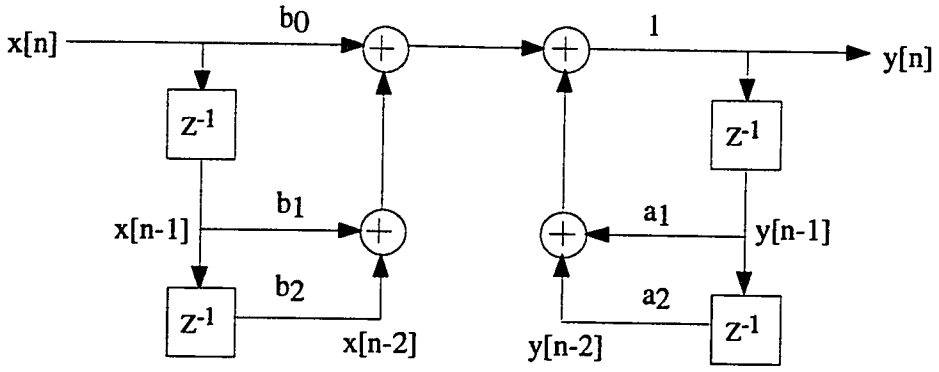

Figure A.2. Signal Flow Graph of a Digital High Pass Filter.

```
Highpass_Filter()                                   /* 2nd Order Butterworth Highpass Filter */
{
        double a1, a2, a3, b0, b1, b2;
        float gain_term;

        a1 =   -1.998307473569944;                  /* Highpass Filter Coefficients */
        a2 =   +9.983089046822168e-1;
        b0 =   +9.991540945630404e-1;
        b1 =    -1.998308189126080;
        b2 =   +9.991540945630402e-1;
        gain_term = 10;

        filter_counter++;                           /* The following are all global variables */
        if (filter_counter >= 10)
        {
            gx_present = gain_term * gPosition;     /* Input position measurement */
            gy_present = b0*gx_present + b1*gx1_past + b2*gx2_past - a1*gy1_past - a2*gy2_past;
            gx2_past = gx1_past;                    /* Initialized to zero */
            gx1_past = gx_present;
            gy2_past = gy1_past;
            gy1_past = gy_present;

            filter_counter = 0;
        }
        gHPFposition = gy_present;                  /* Filtered Position Measurement */
}
```

Figure A.3. C Programming Code for the Implementation of a Digital Highpass Filter.

APPENDIX B

Equipment Specification Tables

Table B.1

Three-Phase Induction Motor Technical Nameplate and Experimental Specifications.

Description	Specification	Units
Manufacturer	Baldor	-
Frame	145T	-
Specification No.	05C01W03	-
Catalog No.	M3587T	-
Phase	3	-
Max. Speed	1725	rev/m
Horsepower	2	hp
Poles	4	-
Class	F	-
Line Voltage	208,230,460	V
Line Current	6.5,6.2,3.1	A
Efficiency	82.5	%
Power Factor	77	%
Stator Resistance†	1.20	Ohms
Rotor Reistance†	0.82	Ohms
Inductance†	0.108	H

†Data experimentally determined by using the identification routine as outlined in Chapter 3.

Table B.2

Torque Transducer Technical Specifications.

Description	Specification	Units
Manufacturer	Himmelstein	-
Model No.	4902V-N	-
DC Output Voltage (+/-)	5	V
Max. Speed	5000	rev/m
Max. Torque	133	N-m
Scale Factor (CW)‡	23.1076	N-m/V
Scale Factor (CCW)‡	22.8008	N-m/V
Bandwidth (High Freq. Output)	300	Hz
Bandwidth (Low Freq. Output)	1	Hz
Supply Current	40	mA

‡Scale factors calibrated experimentally under constant torque conditions.

Table B.3

Flexible Miniature Disc Coupling Technical Specifications.

Description	Specification	Units
Manufacturer	Thomas	-
Coupling Type	DBZ	-
Coupling Size	75	-
Max. Speed	7800	rev/m
Max. Torque	39.9	N-m
Max. Peak Torque	65.5	N-m
Max. Bore (Standard Hub)	0.875	in

REFERENCES

[1] A. Annaswamy, K. Narendra, *Stable Adaptive Systems*. New Jersey: Prentice Hall International, 1989.

[2] Z.G. Bai, K. Ide, T. Tsuji, Z.J. Yang "Vector approximation method with parameter adaptation and torque control of csi-fed induction motor," *IEEE Trans. Industry Applications*, vol. 31, no. 4, July/Aug. 1995, pp. 830-840.

[3] D. Bak, "AC 'Drives' Ahead," *Engineering News*, pp. 23-24, May 6, 1996.

[4] F. J. Bartos, "Flux Vector AC Drives are Poised for Wider Growth," *Control Engineering*, pp. 75-81, Feb. 1995.

[5] R. Barro, P. Hsu, "Torque ripple compensation of vector controlled induction machines," in *IEEE Proc. Power Elect. Specialist Conf.*, 1997, pp. 1281-1287.

[6] R. Barro, P. Hsu, "Torque ripple compensation of induction motors under field oriented control," in *IEEE Proc. Applied Power Elect. Conf.*, 1997, pp. 527-533.

[7] B. K. Bose, *Power Electronics and AC Drives*. New Jersey: Prentice Hall, 1986.

[8] S. J. Chapman, *Electric Machinery Fundamentals*, 2nd ed. New York: McGraw Hill, 1991.

[9] L. O'Connor, "Electric vehicles move closer to the market," *Mechanical Engineering*, March 1995, pp. 82-87.

[10] R. C. Dorf, *Modern Control Systems*, 6th ed. Massachusetts: Addison Wesley Publishing Company, 1992.

[11] G. F. Franklin, J. David Powell, and Abbas Emami-Naeini, *Feedback Control of Dynamic Systems*, 3rd ed. Massachusetts: Addison-Wesley Publishing, 1992.

[12] C. V. Jones, *The Unified Theory of Electrical Machines*. New York: Plenum Press, 1967.

[13] B. Guru and H. Hiziroglu, *Electric Machinery and Transformers*. New York: Harcourt Brace Jovanovich Publishers, 1988.

[14] K. M. Hebber, S. D. T. Robertson, "Torque pulsations in induction motors with inverter drives," *IEEE Trans. Industry Applications*, vol. 1A-7, March/April, 1971 pp. 318-323.

[15] J. Holtz and L. Springob, "Identification and compensation of torque ripple in high-precision permanent magnet motor drives," *IEEE Trans. on Industrial Electronics*, vol. 43, no. 2, April 1996, pp. 309-320.

[16] P. Hsu, "*A short course on vector control (1996-1997).*" Unpublished notes.

[17] M. Inoue, S. Morimoto, Y. Takeda, K. Taniguchi, "PWM strategy for reducing torque ripple in inverter-fed induction motor," *IEEE Trans. Industry Applications*, vol. 30, no. 1, Jan./Feb. 1994, pp. 71-77.

[18] J. A. Karnas, D. Platnik, and P. F. Ryff, *Electric Machines and Transformers*. New Jersey: Prentice Hall, 1987.

[19] T. Koga, A. Matsumoto, I. Miyashita, Y. Okada, "Torque ripple reduction methods for vector controlled induction motor with current preview control," in *IEEE Proc. Ann. Conf. Industrial Electronics Society*, 1989, pp. 192-197.

[20] P. C. Krause, *Analysis of Electric Machinery*. New York: McGraw Hill, 1986.

[21] P. C. Krause and O. Wasynczuk, *Electromechanical Motion Devices*. New York: McGraw Hill, 1989.

[22] W. Leonhard, *Control of Electric Drives*. Berlin: Springler-Verlag, 1985.

[23] V. E. Mablekos, *Electric Machine Theory for Power Engineers*. New York: Harper & Row Publishers, 1980.

[24] N. Mohan, W. Robbins, T. Undeland, *Power Electronics - Converters, Applications, and Design*. New York: John Wiley & Sons, 1995.

[25] D. North, "Control system Key to B-2 Flight Qualities," *Aviation Week & Space Technology*, pp. 46-51, April 17, 1995.

[26] A. V. Oppenheim and R. W. Schafer, *Discrete-Time Signal Processing*. New Jersey: Prentice Hall, 1989.

[27] C. L. Phillips and H. T. Nagle, *Digital Control System Analysis and Design*, 3rd ed. New Jersey: Prentice Hall, 1995.

[28] M. J. Riezenman, "EV Watch," *IEEE Spectrum*, pp. 74-75, Sept. 1995.

[29] A. Sedra and K. Smith, *Microelectronic Circuits*, 3rd ed. New York: Saunders College Publishing, 1991.

[30] V. Del Toro, *Electric Machines and Power Systems*. New Jersey: Prentice Hall, 1985.

[31] P. Vas, *Vector Control of AC Machines*. Oxford: Oxford University Press, 1990.

[32] *Analog Devices Design-In Reference Manual*, 1994.

[33] "Statistical Yearbook of the Electronic Industries," *1996 Electronic Market Data Book*, pp. 100-101.

[34] The Math Works Inc., *The Student Edition of MATLAB*. New Jersey: Prentice-Hall, 1995.